Instigating and Investigating Cellular Chemistry via Fluorescence Microscopy

Wenzhou (Kevin) Zhang

Department of Chemistry

McGill University

Montreal, Canada

February 2024

A thesis submitted to McGill University in partial fulfillment of the requirements of the degree of

Doctor of Philosophy

(Photo taken by Kevin Zhang, 2016)

The first commandment for every good explorer is that an expedition has two points; the point of departure and the point of arrival. If your intention is to make the second theoretical point coincide with the actual point of arrival, don't think about the means – because the journey is a virtual space that finishes when it finishes, and there are as many means as there are different ways of "finishing." That is to say, the means are endless.

-Ernesto 'Che' Guevara, The Motorcycle Diaries (1993)

Abstract

This thesis describes our efforts in using live cell imaging with fluorogenic, chemo-selective molecules to probe the milieu of oxidative stress-related cell death. Reactive oxygen species (ROS) have long been a subject of great importance in the field of biology and medicine. While ROS has been implicated in numerous disease states and pathologies, they can also be harnessed as therapeutics such as in photodynamic therapy (PDT). Lipid autooxidation – the autocatalytic cycle of lipids being degraded into lipid hydroperoxides through a free radical pathway – in particular has raised great interest, as it is the central chemical reaction involved in a recently discovered form of cell death called ferroptosis – for which the fundamental molecular mechanisms of its execution are still poorly understood. Fluorescence microscopy, including super-resolution techniques, present a unique opportunity into gaining access to such systems as minute changes can be detected, with good spatial and temporal resolution, all while minimally perturbing cellular function. To this end, this work focused on three major goals: 1) to gain a mechanistic understanding of ferroptotic cell death by monitoring ferroptosis progression in live cells using fluorescence microscopy-based strategies and H_4B-PMHC – a fluorogenic radical trapping antioxidant probe –; 2) To exploit the ROS imbalance in ferroptosis toward generating new strategies that bring together ferroptosis inducers and photodynamic therapy. Enhanced imaging sensitivity will also be explored. Both aims are facilitated by working with the dormant photosensitizer H_3BrB-PMHC – a dual-action fluorogenic antioxidant probe and dormant photosensitizer; and 3) To conduct super resolution imaging in healthy cells and in ferroptosis, using the reversible Michael acceptor fluorogenic probe cyanoAcroB (a lipid derived electrophile (LDE) mimic).

The body of experimental work is reflected in three experimental chapters. A first chapter outlines our work on ferroptosis with a palette of fluorogenic antioxidant-mimicking probes, positioning our method as a useful toolbox for the study of ferroptosis. We identify an ordered sequence of events

to the execution of ferroptosis. Alongside this, we present a proof-of-principle usage of H_4B-PMHC as an internal standard for the assessment of ferroptosis inhibitors. We also identify the endoplasmic reticulum as the critical organelle in the protection against ferroptosis onset. A second chapter presents the usage of our dormant photosensitizer probe H_3BrB-PMHC. Conceived to undergo activation upon reaction with ROS, an autocatalytic process next takes over as singlet oxygen is generated from newly activated compound in turn activating nearby dormant probes. The new probe was utilized to identify with enhanced sensitivity regions of cells undergoing increased ROS imbalance. Lipid droplets were thus identified as such sites. We posit a hypothesis for this phenomenon as lipid droplets as a primary site of polyunsaturated fatty acid storage and a protection mechanism against further oxidative stress. A third chapter seeks to elucidate how LDEs react within cells and exploit this reactivity toward enhanced resolution of reaction sites. LDEs such as α,β-unsaturated aldehydes are formed upon lipid hydroperoxides rearrangement and their chemistry, and their biological and health implications are intimately related to ferroptosis pathology. Here, we show that a fluorogenic reversible Michael acceptor (an LDE mimic) may be used to interrogate the chemistry of lipid-derived electrophiles, while unraveling the dynamics of organelles (e.g. mitochondria) where this chemistry takes place.

This work provides new insights and broadens the scope of applications where fluorescence microscopy may be utilized toward interrogating biological problems. From the mechanistic understanding of a new modality of cell death, to identifying subcellular locations of ROS, to optimizing conditions for super-resolution live cell microscopy and its usage in LDE chemistry exploration, the techniques developed in this work may serve as a springboard for further development in the field.

Résumé

Cette thèse décrit nos efforts pour utiliser l'imagerie en direct des cellules avec des molécules fluorogènes et chimio-sélectives afin d'explorer le milieu de la mort cellulaire liée au stress oxydatif. Les espèces réactives de l'oxygène (ROS) ont longtemps été un sujet d'une grande importance dans le domaine de la biologie et de la médecine. Bien que les ROS aient été impliqués dans de nombreuses maladies et pathologies, ils peuvent également être exploités comme thérapeutiques, comme la thérapie photodynamique (PDT). La peroxydation des lipides - le cycle autocatalytique de dégradation des lipides en hydroperoxydes lipidiques - est particulièrement fascinante, car elle est à la base d'une forme récemment découverte de mort cellulaire appelée ferroptose, dont les mécanismes fondamentaux d'exécution sont encore mal compris. La microscopie de fluorescence, y compris les techniques de super-résolution, offre une opportunité unique d'accéder à de tels systèmes car de minuscules changements peuvent être détectés, avec une bonne résolution spatiale et temporelle, tout en perturbant au minimum la fonction cellulaire. Dans cette optique, ce travail s'est concentré sur trois objectifs majeurs : 1) utiliser des stratégies basées sur la microscopie de fluorescence et le H4B-PMHC - une sonde fluorogène mimant les antioxydants - pour comprendre les mécanismes de la mort cellulaire par ferroptose ; 2) évaluer le photosensibilisateur dormant H3BrB-PMHC - un photosensibilisateur à double action et une sonde fluorogène ; et 3) utiliser la sonde fluorogène à accepteur de Michael réversible cyanoAcroB pour l'imagerie en direct de cellules en super-résolution de l'ajout de thiols se produisant in vitro.

Le premier chapitre décrit notre travail sur la ferroptose avec une palette de sondes fluorogènes mimant les antioxydants, positionnant notre méthode comme une boîte à outils utile pour l'étude de la ferroptose. Grâce à l'utilisation de la microscopie multicanal, nous identifions une séquence ordonnée d'événements dans l'exécution de la ferroptose. Parallèlement, nous présentons une utilisation de

principe de H4B-PMHC comme norme interne pour l'évaluation des inhibiteurs de la ferroptose. De plus, en utilisant des sondes PMHC ciblant les organites, nous identifions également le réticulum endoplasmique comme l'organe critique dans la protection contre l'apparition de la ferroptose. Le deuxième chapitre présente l'utilisation de notre sonde photosensibilisatrice dormante H3Br-PMHC. Notre sonde à base de PMHC activable par les ROS a été réglée pour équilibrer la génération d'oxygène singulet et la fluorescence, fournissant un générateur et un indicateur d'oxygène singulet. L'avantage de l'autocatalyse - l'activation de la sonde engendrant d'autres activations de la sonde - a été utilisé pour identifier des régions sensibles aux ROS des cellules, des emplacements subcellulaires où l'activation de la sonde se produit plus rapidement, notamment les gouttelettes lipidiques. Nous émettons l'hypothèse d'un phénomène selon lequel les gouttelettes lipidiques sont un site principal de stockage des acides gras polyinsaturés et un mécanisme de protection contre un stress oxydatif supplémentaire. Le troisième chapitre met l'accent sur l'amélioration de l'imagerie en super-résolution des cellules vivantes grâce à une conception rationnelle des sondes. Les hydroperoxydes lipidiques subissent une réarrangement en produits électrophiles réactifs tels que les aldéhydes α,β-insaturés dérivés des lipides (électrophiles dérivés des lipides), dont les chimies sont étudiées et caractérisées pour leurs implications biologiques et sanitaires. Ici, nous montrons qu'un accepteur de Michael fluorogène réversible pourrait être utilisé pour interroger la chimie des électrophiles dérivés des lipides, où la réversibilité réglée minimise l'accumulation de produits fluorescents et prolonge la fenêtre d'imagerie permettant une imagerie en super-résolution à l'échelle de l'heure.

Dans l'ensemble, ce travail apporte de nouvelles perspectives et élargit le champ d'application de ce que la microscopie de fluorescence peut être utilisée pour interroger des problèmes biologiques. De la compréhension mécanistique d'une nouvelle modalité de mort cellulaire, à l'identification des localisations subcellulaires des sensibilités aux ROS dans la thérapie photodynamique, à l'optimisation

des conditions pour la microscopie de cellules vivantes en super-résolution, les techniques développées dans ce travail pourraient servir de tremplin pour d'autres développements dans le domaine.

Acknowledgments

First of all, I would like to thank my supervisor and co-pilot, **Dr. Gonzalo Cosa**. The enthusiasm and thoroughness of our very first interaction (a 10PM email on New Year's Eve, 2015!) when I as a 21-year-old undergrad inquired about the group fully won me over, and that enthusiasm never wavered from the start of this journey to the end. The road has been bumpy at times, and the weather has not always been perfect (such as our group picnic of 2017), but we navigated everything that came our way. For your infinite patience and guidance, I will forever be indebted.

For my committee members, **Dr. Chris Thibodeaux** and **Dr. Paul Wiseman**, thank you for the advice and feedback over the years. For my thesis examiners, **Dr. Amy Blum**, **Dr. Pedro Friedmann-Angeli**, and **Dr. Dima Perepichka**, thank you for the critical read of my thesis and the thought-provoking questions. For the support staff of the Department: **Chantal Marotte, Jean-Marc Gauthier, Rick Rossi, Robert Workman, Dr. Robin Stein, Dr. Alex Wabha, Dr. Hatem Titi, and many others**, thank you for ensuring the smooth operation of our buildings over the years. For the team at **Nikon Canada: Vincent, Hicham, Marc, Nic, Wissam, and Remi**, thank you for always being responsive and cooperative, even when the microscope is not. For the funding agencies, NSERC and FRQNT in particular, thank you for the financial support of me personally, but also our lab as a whole.

For my wonderful group members past and present, thank you all collectively for your company (and putting up with me for so long). I could not have imagined a better cohort to spend these years with. **Dr. Lana Greene**: H_4B-PMHC goddess and HeLa extraordinaire. Thank you for your mentorship, friendship, and continued support from across the screen. **Dr. Ricky Lincoln**: team cell imaging dungeon master. Thank you for showing me the ropes when I first started in the lab, for the many fruitful collaborations, and for bailing me out of trouble too many times to count. **Dr. Christina Calver**: the predecessor of the Cosa group's tradition of prairie degeneracy. Thank you for the good vibes, for

introducing the lab to Pil, and Moose Bar. **Dr. Viki Glembockyte**: eagle eyes! Thank you for always being so helpful, your generosity with your time, and the best beer after an 11hr hike (Whiteface stout). **Dr. Yasser Gidi** (or Christian?): the corridor reggaetonero. Thank you for your companionship through all the late nights in the corridor, the gym, the squash court, and whenever I decided to tear up your kitchen with Pablo. **Dr. Casey Platnich**: the group's best PowerPoint maker and second-best Calgarian. Thank you for playing a key role in all of our group's best memories, from welcoming me into the group in my first week with a birthday cake, and the best parties (with champagne pong) on St Urbain. **Dr. Julia McCain**: heavy atom effect and knitting extraordinaire. Thank you for the many years side by side (literally), and ensuring that I could get through a chemistry degree without ever running an NMR. **Dr. Aya Sakaya**: P&P second-floor office survivor, President's Choice cookie enjoyer, lipid bilayer & instrumentation goddess. I have too many things to say, some of which are not suitable for print form, so I will just simply say "thank you for being a part of this journey." **Dr. Anthony Van Kessel**: cell culture #2, ElectrophileQ #1. Thank you for all the many discussions in the corridor, scientific or otherwise. The ferroptosis wing of our research would not have been possible without you. **Jorge Ramos**: thank you for being the instrumentation and software whiz. **Flor Fungo:** the successor to the endless battles against our Nikon microscopes, thank you for the best empanadas árabes and all the often unrecognized contributions in keeping our lab running. **Andy Yin:** thank you for all the humour you provided to our gatherings, especially at camping. **Alex Feghali:** thank you for all the levity you brought to my DMs. **Paty Islas:** thank you for the late-night snacks in the corridor. **Laiyi Xu:** thank you for the wonderful collaboration, your invaluable contribution to the ferroptosis storyline can not be understated. **Denys Holovan:** thank you for picking up the torch of #teamcellimaging and your endless curiosity. **Heidi Dewling:** thank you for being our gen Z reference. **Juan Sanchez**: best of luck with taking on the torch of cell imaging. **Dr. Morgan Foret:** honourary Cosa group member, thank you for being a great friend throughout the years.

For all the wonderful postdocs and visitors in the lab throughout the years, while our interactions may have been short, I truly cherished them nevertheless. **Dr. Mayra Martinez (and Dr. Pablo Maqueo)**: thank you for all the wonderful food adventures spanning St. Dominique (carnitas & dumplings), Guanajuato (pulque w/ red wine), and Deep River. **Dr. Sol Martinez and Dr. Andres Durantini:** thank you for periodically coming back to Montreal and brightening up the lab (with Bianca as well), and the sometimes questionable beverage choices (tequi-mate). **Dr. Kasia Jodko-Piorecka:** thank you for all the deep chats in the kitchen, and your invaluable contribution in bringing cyanoAcroB to life! **Dr. Terri Lowell:** thank you for bringing up the average pun level of the lab (and all the science help, of course). **Dr. Alejandro Blasco:** thank you for being a great team member. **Dr. Luisa Pereira:** thank you for the best dance moves and your contagious positivity. **Dr. Rodrigo Ponzio:** thank you for the best paper airplanes at 3 Brasseurs. **Dr. Roger Bresoli-Obach**: gràcies for the wonderful collaboration and those long weekends in the microscope room. **Dr. Kris Jannsen:** thank you for the degeneracies around town and the Rogers Cup memories. **Dr. Jose Luis Fonseca:** thank you for beings #fitspo.

To the various friends in the chemistry department (in no particular order), thank you for the memories, the borrowed reagents, the helpful discussions, the shared drinks, the gossip, and much much more. **Dr. Sebastian Skaanvik** (for all the cell culture help and Crab Night!), **Dr. Danny Chhin** (for keeping me humble in badminton), **Dr. Jeremy Dawkins** (for the camping and wizard staffs), **Prof. Sam Gateman** (inspiration, in and out of the lab), **Isabelle Beaulieu** (for the Herculean effort in keeping the cell culture room running), **Dr. Dan O'Reilly** (too many things to mention, you degenerate), **Dr. Miguel Garavís** (for being the best Fieldhouse hitting partner and the second biggest Rafa fan in P&P). **Dr. Danielle Vlaho & Mitch Huot** (for being the best party hosts and Halloween couple costumes), **Dr. Kevin Uggowitzer** (for organizing the best meetings in OM10), **Hasan Isaak** (encouragement and Toronto propaganda), **Dr. Mostafa Rammal** (racquet sports buddy), **Dr. Tobias Priemel** (beer staff, fleischsalade,

and ChemBio expertise), **Prof. Justin Di Trani & Prof. Rob Harkness** (for being the most memorable duo of the 3rd floor office and an absolute force of nature in both productivity and in swag), **Chris Hennecker** (for the "best" rendition of Stacy's Mom), **Felipe Venegas** (for the most random posting history), **Prof. Dustin Duncan** (being so diligent that I wear my labcoat when I borrow reagents), **Dan Therien** (for letting me borrow reagents without a labcoat on when Dustin's not looking), **Dr. Morten Loehr** (for the cell culture companionship and Killepitsch), **Kaifeng Zhao** (for the cell culture room comradery)**, Dr. Kamila Mustafina** (for the microscopy commiserations) **, Dr. Alex Gellé** (for Pint of Science, staging the most efficient* move out of St Denis, for co-parenting)**, Dr. Alain Li** (for the ever tempting offer of a place to crash in Shanghai)**, Dr.Sosthène Ung** (for the many years of baijiu adventures), **Dr. Jun Zhu** (for always thinking of me)**, Dr. Yun Wang** (for the interesting corridor kitchen chats)**, Dr. Siting Ni** (for your eternal kindness and optimism)**, Dr. Alex Wahba & the Chemistry Outreach crew**, and probably some that I have missed!

To the **McGill Tennis Club**, especially the executives (**Brandon, Benny, Manon, Chris, Alex**), thanks for all the hits! Your presence on the other side of the net (ready to crush my backhand returns landing nice and high just past the service line) were a welcome respite for the long days at the lab. I'm glad we got to keep the club going for so long, and here's to the next generation.

To the **Beloyannis** and **Bethune** clubs of the PCQ, thank you SD, EE, BS, MJ, FF, KZ, KT, IS, and many more that I may have missed for the comradery. To the comrades re-invigorating **SftP Canada**, thank you for bringing struggle to the science, and science to the struggle. To **Alexandra Elbakyan**, our modern-day Prometheus, thank you for taking on the noble quest of fighting for free access to knowledge as a human right. To the **comrades in Chiapas**, thank you for the important ideological education: it's necessary to create a new world, a world where many worlds fit, a world where all worlds fit. To **comrades everywhere**: "the point however, is to change it."

To the **Thai Express in the McGill metro**: thank you for keeping me (along with half the Chinese internationals on campus) fed with the best (secret menu) Chinese food in Montreal.

To **anyone I may have missed** out on, my apologies and I hope to express my gratitude in person some time down the line.

And finally, **to my parents**. While sometimes there may be a continent of distance and a sea of understanding between us, no words or deeds can truly convey my eternal gratitude for everything.

****

As cell culture, particularly the HeLa cell line, played a large part in this thesis, a special acknowledgement must be made. The HeLa cell line was derived from the tissues of Henrietta Lacks, without her knowledge or consent. In the seven decades since, countless financial gains in the form of therapeutics and patents have been profited off the HeLa cell line, without adequate recognition and certainly without adequate compensation for Ms. Lacks or her family. We thank her immeasurable contributions not only to the last decade of cell imaging work in the Cosa group, but also to human health and disease worldwide.

Author Contributions

All publications were co-authored with research supervisor **Dr. Gonzalo Cosa** (Department of Chemistry, McGill University), who jointly contributed to project design and manuscript preparation.

Chapter 2

Wenzhou (Kevin) Zhang contributed to project design, performed the cell culture and fluorescence microscopy experiments, data analysis, and contributed to manuscript preparation. **Laiyi Xu** contributed to probe synthesis and spectroscopic characterisations, assisted with cell culture and fluorescence microscopy experiments, data analysis, and contributed to manuscript preparations. **Julia McCain** contributed to probe synthesis. **Terri Lovell** contributed to manuscript preparations and helpful discussions.

Chapter 3

Wenzhou (Kevin) Zhang contributed to project design, performed the cell culture and fluorescence microscopy experiments, data analysis, and contributed to manuscript preparation. **Roger Bresoli-Obach** assisted with cell culture and fluorescence microscopy experiments. **Julia McCain** contributed to probe synthesis.

Chapter 4

Reproduced from "Chemically Tuned, Reversible Fluorogenic Electrophile for Live Cell Nanoscopy", Lincoln, R.*; **Zhang, W.***, Lovell, T.C., Jodko-Piorecka, K., Devlaminck, P.A., Sakaya, A., Van Kessel, A.T.M., and Cosa, G., ACS Sensors (2022), 7, 1, 166-174. Copyright 2022 American Chemical Society

Wenzhou (Kevin) Zhang contributed to project design, performed the cell culture, spectroscopy, and microscopy experiments, data analysis, and contributed to manuscript preparation. **Richard Lincoln** contributed to project design, synthesized the compounds, performed the microscopy and spectroscopy experiments, data analysis, and manuscript preparation, for which portions of his work are included in

his PhD thesis. **Terri Lovell** conducted the DFT calculations. **Katarzyna Jodko-Piorecka** performed the data analysis and manuscript preparation. **Pierre Devlaminck** conducted probe synthesis. **Aya Sakaya** assisted in spectroscopic measurements**. Antonius Van Kassel** conducted probe synthesis and purification.

Publications

Article 1 was published as part of this thesis. Articles 2-4 were published during the thesis period but are not included in this thesis.

1. Zhang, W.*; Lincoln, R.*; Lovell, T. C.; Jodko-Piorecka, K.; Devlaminck, P.A.; Sakaya, A.; Van Kessel, A.T.M.; Cosa, G. Chemically Tuned, Reversible Fluorogenic Electrophile for Live Cell Nanoscopy. *ACS Sensors*, 7, **2022**, 1, 166-174.
2. Lincoln, R.; Van Kessel, A.T.M.; Zhang, W.; Cosa, G. A Dormant BODIPY-Acrolein Singlet Oxygen Photosensitizer Intracellularly Activated upon Adduct Formation with Cysteine Residues. *Photochem. Photobiol. Sci.*, 18, **2019**, 2003-2011.
3. Foret, M.K.; Do Carmo, S.; Lincoln, R.; Greene L.E.; Zhang, W.; Cuello, A.C.; Cosa, G. Effects of Antioxidant Supplements on Lipid Peroxidation Levels in Primary Cortical Neuron Cultures. *Free Radic. Biol. Med.*, 130, **2019**, 130, 471-477.
4. Lincoln, R.; Greene, L.E.; Zhang, W.; Louisia, S.; Cosa, G. Mitochondria Alkylation and Cellular Trafficking Mapped with a Lipophilic BODIPY-acrolein Fluorogenic Probe. *J. Am. Chem. Soc.* 139, **2017**, 139, 16273-16281.

Table of Contents

List of Figures

List of Schemes

List of Tables

List of Abbreviations and acronyms

α-TOH α-Tocopherol

ε Extinction Coefficient

λ Wavelength

ϕ_{fl}, Fluorescence Quantum Yield

ABPP Activity-based Protein Profiling

ACSL4 acyl-CoA synthetase long-chain family member 4

ATP adenosine triphosphate

BODIPY Boron-dipyrromethene (4,4-difluoro-4-bora-3a,4a-diaza-sindacene)

BSA Bovine Serum Albumin

BSO Buthionine Sulfoximine

CTCF Corrected Total Cell Fluorescence

DFT Density Functional Theory

DGAT diacylglycerol acyltransferase

DIC Differential Interference Contrast

DMEM Dulbecco's Modified Eagle Medium

DMSO Dimethylsulfoxide

DNA Deoxyribonucleic acid

DoPS Dormant Photosensitizer

EC50 Effective concentration 50%

EMCCD Electron Multiplying Charge Coupled Device

FBS Fetal Bovine Serum

FENIX Fluorescence-Enabled inhibited autoXidation

FLIM Fluorescence Lifetime Imaging Microscopy

FOV Field of view

FSP1 Ferroptosis suppressor protein 1

GPX4 Glutathione Peroxidase 4

GSH Glutathione

HILO Highly Inclined and Laminated Optical sheet microscopy

ISC Intersystem Crossing

LCIS Live Cell Imaging Solution

LDE Lipid Derived Electrophile

LED Light emitting diode

LOO• Lipid Peroxyl Radical

LOX Lipoxygenase

MTT 3-(4,5-dimethylthaizol-2-yl)-2,5-diphenyltetrazolium bromide

NA Numerical Aperture

NASCA Nanometer Accuracy by Stochastic Chemical Reactions

nm Nanometres

NMR Nuclear Magnetic Resonance

PALM Photo-activated Localization Microscopy

PAINT Points Accumulation for Imaging in Nanoscale Topography

PBS Phosphate Buffer Saline

PDT Photodynamic Therapy

PeT Photoinduced Electron Transfer

PI Propidium iodide

PMHC 2,2,5,7,8-Pentamethyl-6-hydroxychromanol

RCD Regulated cell death

ROS Reactive Oxygen Species

RSL3 Ras-selective lethal small molecule 3

RTA Radical Trapping Antioxidant

SDS PAGE Sodium Dodecyl Sulfate Polyacrylamide Gel Electrophoresis

SIM Structured Illumination Microscopy

SMLM Single Molecule Localization Microscopy

SOFI Super-resolution Optical Fluctuation Imaging

SRRF Super-Resolved Radial Fluctuations

STED Stimulated Emission Depletion Microscopy

STORM Stochastic Optical Reconstruction Microscopy

TCSPC Time Correlated Single Photon Counting

TIRF Total Internal Reflection Fluorescence

UV Ultraviolet

WF Widefield

Chapter 1: Introduction

Mankind thus inevitably sets itself only such tasks as it is able to solve, since closer examination will always show that the problem itself arises only when the material conditions for its solution are already present or at least in the course of formation.

-Karl Marx, A Contribution to the Critique of Political Economy (1859)

1.1 Preface

Theory and methodology exist in a dialectical relationship. Challenging problems require the development of adequate tools, which affords further insights into the previously unknown, illuminating further problems, and the cycle is repeated *ad infinitum*.

The problem chosen for this investigation is the very problem of life itself. As aerobic beings, utilizing oxygen for metabolism comes at the cost of oxidative stress, which we have evolved to balance in a delicate homeostasis. The recently discovered form of cell death resulting from excess oxidative stress in lipid membranes has garnered significant interest, yet fundamental questions remain unresolved as to its origin and final execution.

The methods of choice for this research are primarily fluorescence-based, a boon to the study of biological systems ever since its inception. Being able to light up specifically labeled molecules against a dark background with little perturbation allows for the extraction of a rich trove of information, such as distribution, structural features, quantity, and rates.

This introduction aims to provide the reader with an overview of oxidative stress biology and the tools used to study it. A particular focus will be placed on our subject of interest – lipid peroxidation and ferroptosis. Fluorescence methodologies utilized in the subsequent chapters of original research will be adequately described and contextualized.

1.2 Lipid Peroxidation: From the Very Beginning (of the Universe)

1.2.1 Oxygen: Chronicle of a Death Foretold

Oxygen is an essential factor for sustaining the majority of living things on earth; however, it was not always this way. The earliest lifeforms – microorganisms inhabiting deep sea vents – appeared roughly 3.4 billion years ago[1]; it would take another billion years for oxygen in the form most familiar to us – as O_2, an atmospheric gas – to appear in any significant quantity. This was an event termed the Great Oxygenation Event (GOE),[2, 3] triggered approximately 2.6 billion years ago by the emergence of cyanobacteria that evolved to harness the light of the sun to generate energy via photosynthesis and produce oxygen from the splitting of water.[3] Initial atmospheric O_2 levels were suppressed as free iron and other mineral deposits absorbed atmospheric O_2 to form oxides,[4] and they only began to accumulate after the saturation of these mineral deposits, rising from negligible to as high as 21% O_2.[2] To the primarily anaerobic organisms on earth, this was a death sentence, as they were defenseless against the toxic effects of oxygen. Ionizing UV radiation from the sun generates ozone, which in an aqueous milieu leads to promiscuously reactive oxygen species[3] (ROS, **Section 1.2.2**) forming that can modify and damage many key biomolecules.

Heightened atmospheric O_2 levels presented new opportunities for organisms evolved to take advantage of it. More efficient aerobic respiration for energy generation allowed for the development of multicellularity and complex tissue development, with vasculature to transport oxygen. Tolerance to oxygen and ROS requires the adaptation of antioxidant defenses (enzymatic and small molecule), the malfunction of which results in disease states.[3, 5] Biological membranes, essential for maintaining concentration gradients and cell integrity, are a major site of concern for oxidative stress. The unsaturated lipid components of biological membranes, contributing to membrane fluidity, are vulnerable to oxidation (discussed in **Section 1.2.4**), the excesses of which can result even in cell death

(**Section 1.3**). It is within these contradictory conditions of oxygen being a gift and a curse that oxidative stress biology and the subject of this thesis begins.

1.2.2 Reactive Oxygen Species in Biology

Reactive oxygen species (ROS) is a collective term given to a multitude of radical and non-radical molecules deriving from oxygen.[3, 5] Examples include hydroxyl ($OH^{\bullet}$), peroxyl ($LOO^{\bullet}$), hydroperoxyl ($HOO^{\bullet}$), and superoxide ($O_2^{-\bullet}$) radical species, and hydrogen peroxide (H_2O_2), lipid hydroperoxide (LOOH), and singlet oxygen ($^1O_2$) non-radical species. Highly – and thus non-specifically – reactive, they are capable of modifying all classes of biomolecules, including nucleic acids,[6] lipids,[7] and proteins.[8] Despite being implicated as a component of almost every disease state, including aging,[9] cancer,[10] neurodegeneration,[11] inflammation,[12] and more, ROS also serve as mediators of cellular homeostasis.[13] ROS are utilized as signalling molecules as well as in cellular defense mechanisms.[3] A delicate homeostasis of ROS is required for basal metabolism, while perturbation towards the side of oxidation results in oxidative stress.

Aside from external stressors like UV or photosensitizers (**Section 1.4.8**), ROS are primarily generated endogenously as a consequence of enzymatic electron transfer processes[14] and low basal level ROS are always present in the cellular milieu (**Fig. 1.1**). For example, leakages within the mitochondria electron transport chain (ETC), or in NADPH oxidases in the plasma membrane, produces $O_2^{-\bullet}$. H_2O_2 is also a product of peroxisomal enzymatic activity in fatty acid degradation, which in the presence of intracellular iron can undergo a Fenton chemistry/Haber-Weiss cycle to produce $OH^{\bullet}$. Antioxidant enzymes are expressed to keep the levels of ROS species in check, such as superoxide dismutase (SOD) converting $O_2^{-\bullet}$ into the less reactive H_2O_2, which is then reduced to water by catalase.

The interest of this thesis lies primarily in lipid-associated ROS, namely the process of lipid peroxidation (**Section 1.2.3**). As many sources of ROS are membrane-bound or adjacent – such as

aerobic respiration – it stands to reason that lipids, the majority component of biological membranes, will withstand a heavy burden of oxidative stress.

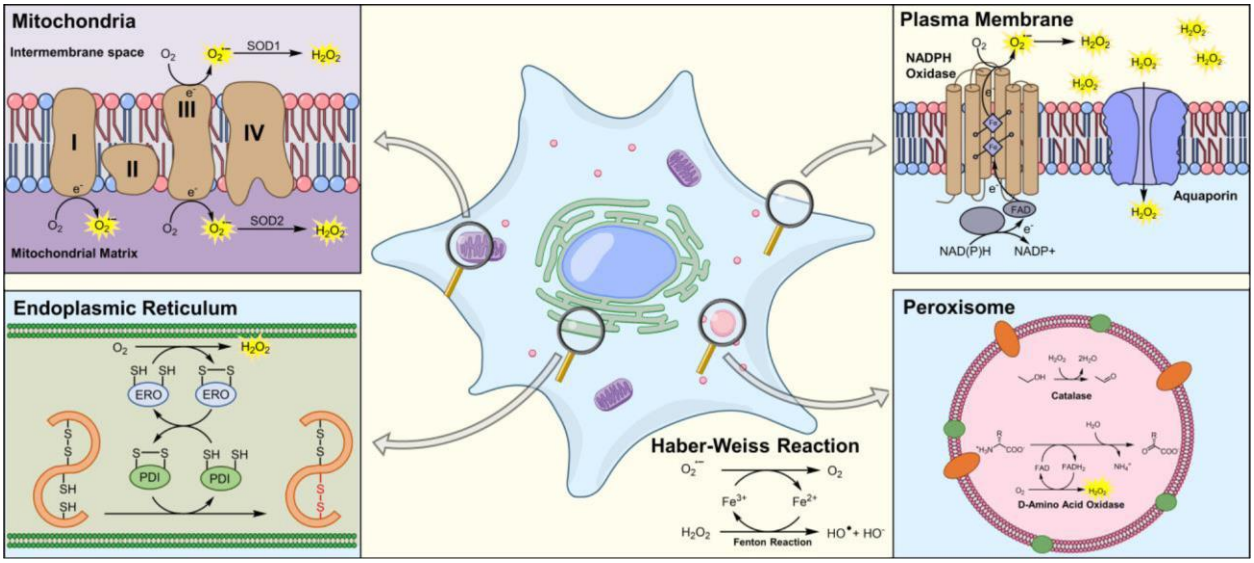

Figure 1.1: Overview of major sites of lipid-associated ROS in various cellular organelles. Reproduced with permission from reference.[14]

1.2.3. Lipid Autoxidation/Peroxidation

Lipid autoxidation is the autocatalytic free radical attack of polyunsaturated fatty acids in lipid membranes in the presence of oxygen, rendering lipid hydroperoxides. The process of lipid peroxidation follows those of other free radical processes in its breakdown into three stages: 1) initiation, 2) propagation, and 3) termination (**Fig. 1.2**). Polyunsaturated fatty acid (PUFA) lipid tails in biological membranes are susceptible to free radical attacks from a variety of initiating radical species in the biological milieu (highlighted in **Section 1.1.2**). This is due to the easily abstractable hydrogen in the bis-allylic position, where following PUFA reaction with free radical initiators carbon centered lipid radical species ($L^{\bullet}$) are formed. Propagation next occurs when the newly formed carbon-centred radical reacts at close to diffusion-controlled rates with molecular oxygen to form a lipid peroxyl radical ($LOO^{\bullet}$),[15] which can then abstract another hydrogen from a neighbouring PUFA, generating another unit of $L^{\bullet}$ and a lipid hydroperoxide (LOOH).[16] Lipoxygenases (LOX) can also directly catalyze the formation of LOOH

from PUFAs.[17] Termination of the radical chain reaction occurs either when two LOO•s combine, or, more likely, by an encounter with radical trapping antioxidants (RTA), such as α-tocopherol (α-TOH, vitamin E).

The accumulation of LOOH is toxic to cells. LOOH may produce further radical products through Fenton chemistry with intracellular iron, which can go on to initiate more lipid peroxidation catalytically. In addition, LOOH can undergo rearrangements into lipid-derived electrophiles[16] (LDE, **Chapter 4**), which can go on to modify proteins upon alkylation of their reactive cysteine residues. In cells, the selenocysteine dependent enzyme glutathione peroxidase 4 (GPX4) couples the oxidation of glutathione (GSH) with the reduction of LOOH to rather inert lipid alcohols (LOH). The impairment of the GPX4 function in LOOH detoxification leads to ferroptosis,[18] further elaborated on in **Section 1.3**.

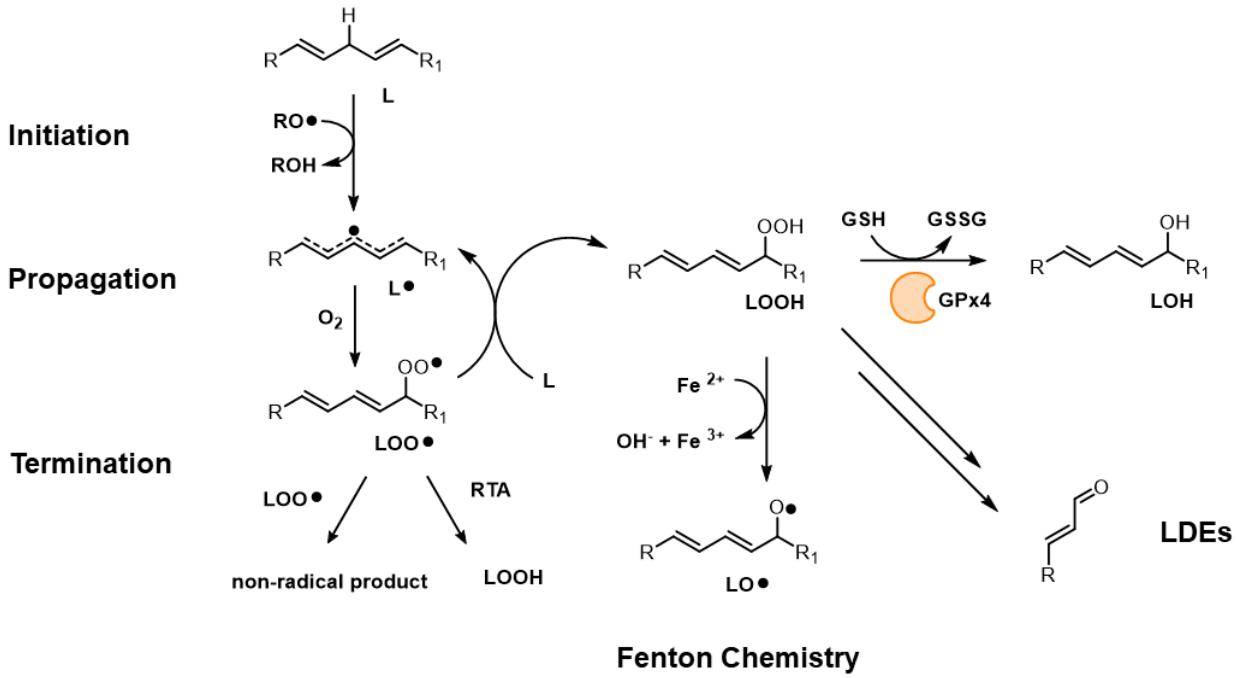

Figure 1.2: Overview of lipid peroxidation in the cellular milieu, including the fate of lipid hydroperoxides (LOOH).[16]

1.3 Ferroptosis – Regulated Cell Death by Lipid Peroxidation

Ferroptosis is the form of cell death stemming from uncontrollable lipid peroxidation. While oxidative stress-related cell death is not new (**Section 1.3.1**), the clear articulation and identification of a mechanism centring (at first, see **Section 1.3.4**) around the action of the lipid hydroperoxide detoxifying enzyme GPX4 unlocked a linkage between metabolism, cellular iron pool, oxidative stress biology, and disease states.[19] As with other regulated cell death mechanisms, control over ferroptosis induction or prevention has tremendous therapeutic potential,[20] which has driven the explosive growth of the field since its commencement a mere 20 years ago.

This section will provide a brief overview into the history of the study of ferroptosis, its key underpinnings, and the unanswered questions in the field which served as the inspiration behind our pursuits in this thesis.

1.3.1 History of Regulated Cell Death (RCD) & Discovery of Ferroptosis

In the early days of biology, cell death was given little thought and dismissed as an inevitable phenomenon of life. The discovery of apoptosis[21] (stemming from the Greek word for "falling off," akin to leaves from a tree) upended such orthodoxy. Apoptosis is a tightly regulated process, with precise external and internal triggers to activate a cascading series of caspases, which go on to cleave cellular proteins in a neat degradation of every cell component. Triggers and inhibitors of apoptosis also exist, showing the process to be governable and exploitable, making apoptosis the first classified regulated form of cell death. This stood in sharp contrast to accidental cell death – instantaneous and catastrophic damage to cellular integrity. Regulated cell death plays an integral part of multicellular organismal development[22] (e.g., dissolving the webbing between fingers during gestation) and the loss of control over cell death leads to the proliferation of cancer.[23] The explosion in the discovery of novel forms of regulated cell death (e.g., pyroptosis,[24] NETosis,[25] cuproptosis,[26] disulfidptosis,[27] etc.) necessitated a

consortium of cell death researchers to provide an updated classification, in which an emphasis is placed on the specific mechanism of execution rather than morphology **(Fig. 1.3)**.[28]

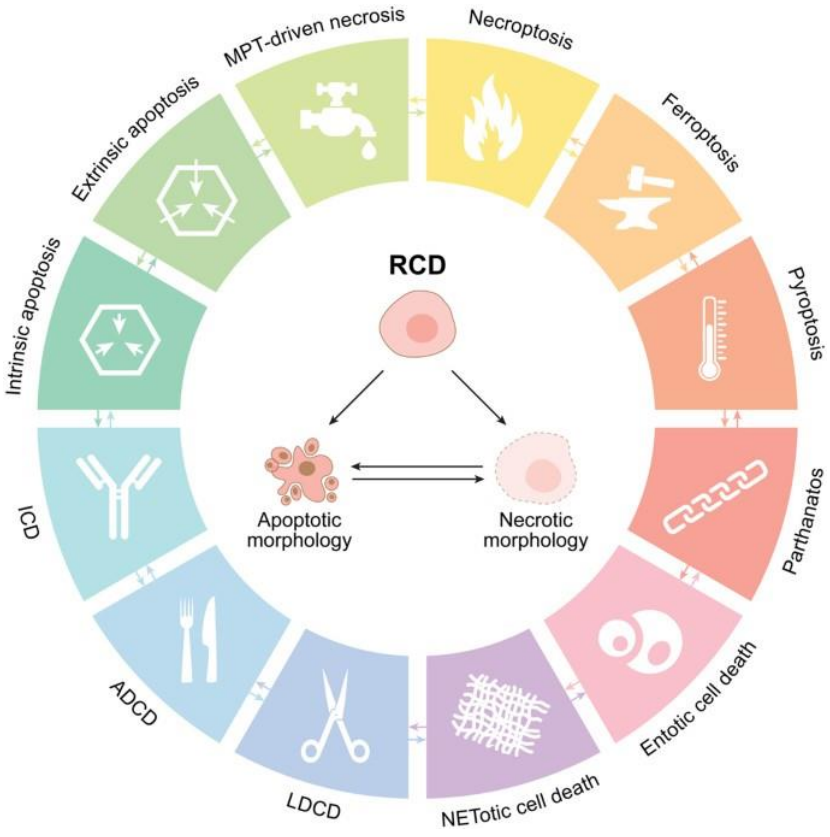

Figure 1.3: Overview of major regulated cell death (RCD) subroutines, highlighting variety and also interconnectivity. Reproduced with permission from reference 28.

In a sense, ferroptosis is the reconciliation of many decades of cell biology, dating back to the earliest days of cell culture. The earliest observations of ferroptosis date back to the 1950s and 1960s in Eagle's pioneering work in the nutritional requirements of cultured cells.[29] Eagle's work showed that the removal of cysteine – which we now recognize as a limiting precursor to the GPX4 axis of ferroptosis (see **Section 1.3.3**) – causes cell death, and that the biosynthesis of cysteine in turn leads to cell resilience. In the decades following, by which time cell death was discovered as a regulated process with the advent of apoptosis, ferroptosis-like cell death was observed once more with the discovery of an

oxidative stress-induced cell death in neuronal cells, then termed oxytosis.[30] Tan, Schubert and Maher observed that excess extracellular glutamate leads to cell death associated with a depletion of GSH and a resultant increase in ROS. We now consolidate this observation, understanding it as an inhibition of GSH synthesis via the inhibition of cystine import proteins (system x_c). The Conrad group in the early 2000s, working in transgenic rat models, firmly established the foundations of ferroptosis as a field, demonstrating lethality with heightened ROS in various organs from the knockdown of GPX4.[31]

Ferroptosis was in parallel discovered in small molecule screening efforts for anti-cancer compounds by the Stockwell group. The compounds erastin,[32] and later RSL3,[33] were discovered to induce cell death in a manner incongruent with any of the mechanisms known thus far (apoptosis, autophagy, necrosis, etc.) by exerting a large amount of lipid peroxidation. The term "ferroptosis" was given due to the finding that erastin/RSL3 induced cell death could be prevented by the chelation of iron. The molecular underpinnings were elucidated later, showing RSL3 to be an inhibitor of the enzyme GPX4 and erastin to be an inhibitor of cystine import – an upstream component of GPX4 function.[18] Thus, the earliest definition of ferroptosis was stated as cell death by lipid peroxidation governed by the function of the enzyme GPX4, and that can be inhibited by iron chelators and lipophilic antioxidants.[18, 28, 34]

1.3.2 Mechanism (of Sorts) of Ferroptosis

With the explosion of available data as the field gained momentum, mechanistic insight into ferroptosis seemed to point to a lack of a common shared mechanism, in sharp contrast to other forms of RCD like apoptosis, with clearly defined regulators and effectors. A meta-analysis of the ferroptosis literature indicated that ferroptosis was highly context dependent,[35] with some metabolites/proteins influencing ferroptosis sensitivity very differently depending on cell type and the method of ferroptosis

induction. The consensus as it stands is that any pathway or metabolite which can directly or indirectly, up or down-regulate the cellular defense against lipid peroxidation is an effector of ferroptosis.

In a recent review, Pratt and Dixon propose a flexible model of ferroptosis (**Fig. 1.4**), understanding it as a series of overlapping and non-mutually exclusive effectors over a common core mechanism.[36] Within this framework, the core mechanism and inner defenses most relevant will be elaborated upon.

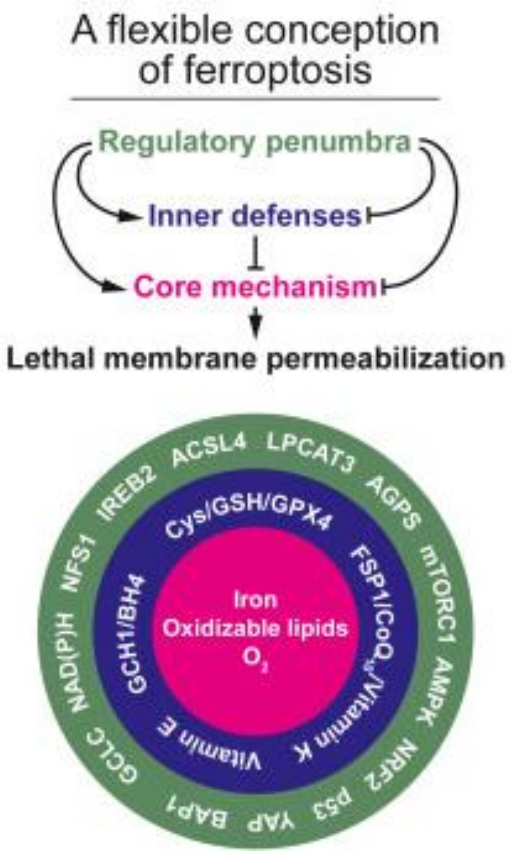

Figure 1.4: A flexible model of ferroptosis proposed by Pratt and Dixon. Reproduced with permission from reference 36.

<u>Core mechanism – requirements for the initiation of ferroptosis:</u>

First and foremost, molecular oxygen is necessary for ferroptosis, as it is the source of the R"O"S which initiates lipid peroxidation (the sources of ROS in cells is elaborated upon in **Section 1.2.2**).

Lipoxygenase enzymes also utilize molecular oxygen directly, such as ALOX-15,[37] which catalyze the regioselective addition of oxygen to PUFAs to form certain lipid hydroperoxide species and are implicated in certain instances of ferroptosis induction. PUFAs, the main oxidizable lipid, serve as the fuel for lipid peroxidation. Ferroptosis can be attenuated or accelerated by changing PUFA availability. Examples of the former includes supplementing cells with monounsaturated fatty acids (MUFAs),[38] or disrupting enzymes, such as acyl-CoA synthetase long-chain family member 4 (ACSL4), that enrich membranes with PUFAs.[39] An example of the latter is the upregulation of PUFA synthesis increasing ferroptosis susceptibility.[37] With the buildup of lipid hydroperoxides (**Fig. 1.2**), the presence of iron can lead to Fenton reaction, leading to further radical species and further lipid peroxidation, linking iron availability and metabolism to ferroptosis. In addition, many enzymes which generate $O_2^{-\bullet}$ and H_2O_2 utilize iron as cofactors. As such, iron availability and metabolism is intimately linked to the induction of ferroptosis. The chelation of iron or the down-regulation of genes in iron metabolism is capable of preventing ferroptosis.[18] Taken together: molecular oxygen, PUFAs/oxidizable lipids, and iron create the conditions from which uncontrollable lipid peroxidation can take place.

<u>Inner defenses – canonical and non-canonical protectors against lipid peroxidation:</u>

The central regulators of ferroptosis are the cellular guardians of lipid peroxidation homeostasis. The selenoprotein GPX4 is the earliest identified and most well-recognized line of defense against the accumulation of lipid hydroperoxides,[18] with inhibition of its expression and function an initiator of ferroptosis. This can be achieved directly by small molecule inhibitors such as RSL3[33] or ML210.[40] As GPX4 is GSH-dependent, disruptions to intracellular GSH levels will also eventually lead to ferroptosis after sufficient depletion, such as that achieved through the action of erastin (a cystine importer) and buthionine sulfoximine[41] (a GSH synthesis inhibitor).

More recently, other endogenous mechanisms have been identified to regulate ferroptosis independent of GPX4, challenging the previously held orthodoxy of GPX4 as the central axis.[18] Ferroptosis suppressor protein 1 (FSP1, renamed from AIFM2/apoptosis-inducing factor 2 due to the recent elucidation of its mechanism) is an oxidoreductase that reduces coenzyme Q_{10} (CoQ_{10}), which can trap lipid peroxyl radicals and further regenerate α-tocopheroxyl radicals, thus ensuring a sustained pool of RTA.[42, 43] The first small molecule inhibitor of FSP-1 function was discovered shortly after.[44] Vitamin K,[45] recharged by the activity of FSP1, also possesses RTA capacity. Taken together: the cellular defenses against lipid peroxidation, whether it be GPX4 or RTA cycles, stop LOOH accumulation and prevent runaway lipid peroxidation.

1.3.4 Key Questions Remaining in the Field

While the state of the field has focused on the identification of new modulators of ferroptosis, with an eye on the role that ferroptosis plays in disease states and avenues for therapeutics, fundamental questions remain. In 2018, Brent Stockwell, one of the pioneers of the field, summarized the key unanswered questions of the field as follows:[46]

1) What are the drivers of lipid peroxidation?
2) Where does lipid peroxidation take place?
3) How exactly do cells die in ferroptosis?

Amidst the exponential growth in ferroptosis literature over the years since 2018, evidence has accumulated to a point where these questions can start to be answered. For instance, the drivers of lipid peroxidation are generally agreed to be the various $O_2^{-\bullet}$ and H_2O_2 species from cellular metabolism (**Section 1.2.2**). However it seems no individual enzyme is necessary for ferroptosis initiation, hence the flexible constellation model of ferroptosis regulation.[35] As well, a matter of where and how much ROS is required to kickstart ferroptosis is still not understood. In the case of where lipid peroxidation takes

place, the endoplasmic reticulum (ER) has been implicated as an essential site of lipid peroxidation, with the exact reason still unresolved. The contributions of various organelles in ferroptosis have been investigated by many groups, especially metabolically obvious ones like the mitochondria[47] – site of oxidative respiration – and lysosomes[48] - keeper of degradative enzymes, with no clear universal relevance and observing context-dependence. Recent works by Stockwell, Woerpel, and Min using the targeted delivery of an endoperoxide (ferroptosis inducer) to various organelles show that the ER is the primary site of lipid peroxidation. While lipid peroxidation can be induced in other organelles to initiate ferroptosis, it is propagated through the ER, where after some delay it finally reaches the plasma membrane.[49] How said lipid peroxidation propagates from the ER to the plasma membrane is thus far an unsettled question.[49] As to the final executioner of cell death, the field has arrived at the consensus of catastrophic membrane permeabilization being the hallmark.[50] It has been shown that ferroptosis leads to the formation of membrane pores, which allow for water entry and causes cell swelling and rounding.[50] However, the causes of pore formation and loss of membrane integrity still require elucidation, although it is speculated to be lipid-derived electrophiles[51], especially aldehyde species.[52]

It is increasingly apparent that the complexity and ambiguity of the ferroptosis puzzle can only be cut through with tools this thesis aims to sharpen.

1.4 Tools and Probes for Studying Lipid Peroxidation and Ferroptosis

The methods for studying lipid peroxidation and its byproducts in ferroptosis are typically endpoint measurements, observing what remains after an induction period of hours to days. Key methodologies employed by the field are outlined here, spanning from colorimetric and fluorescence high throughput assays to lipidomics and imaging

1.4.1 High Throughput Assays of Cell Viability

The efficacy of ferroptosis inhibitors and inducers are commonly screened via cell viability assays. Their commercial availability and multiplex capability present an easy entryway into a quick diagnosis of cell health. Most are colorimetric and rely on quantitation of cellular metabolism as a proxy for cell health. Examples of such assays include the MTT assay,[53] which measures the reduction of the yellow tetrazole compound (3-(4,5-dimethylthaizol-2-yl)-2,5-diphenyltetrazolium bromide, or MTT) to a purple substrate (formazan), mainly via the action of NADPH reductases in the cell cytoplasm. The loss of cell viability results in the loss of reductive power, facilitating this quantification. The resazurin assay, also commercially known under the name AlamarBlue,[54] is another assay based on the reductive potential inside live cells, converting the blue non-fluorescent dye resazurin to the – reduced form – red highly fluorescent resorufin and thus offering two modes of detection, fluorescence and colorimetric. Both assays require an incubation time for sufficient quantities of dye to be reduced until instrument detection limits are reached. CellTiter-Glo® is a cell lysis-based assay[55] which quantifies ATP - present in living cells as the fuel for metabolic activities – via chemiluminescence of the enzyme luciferase and its substrate luciferin, resulting in almost instantaneous quantifications of chemiluminescence at extreme sensitivities. See **Figure 1.5** for a summary of these methods. The same drawback is shared by all these assays in that only static information can be gathered, assessing viability at a discrete timepoint. Dynamic information regarding the speed and proportions of cells undergoing ferroptosis, or other forms of cell death, is missing.

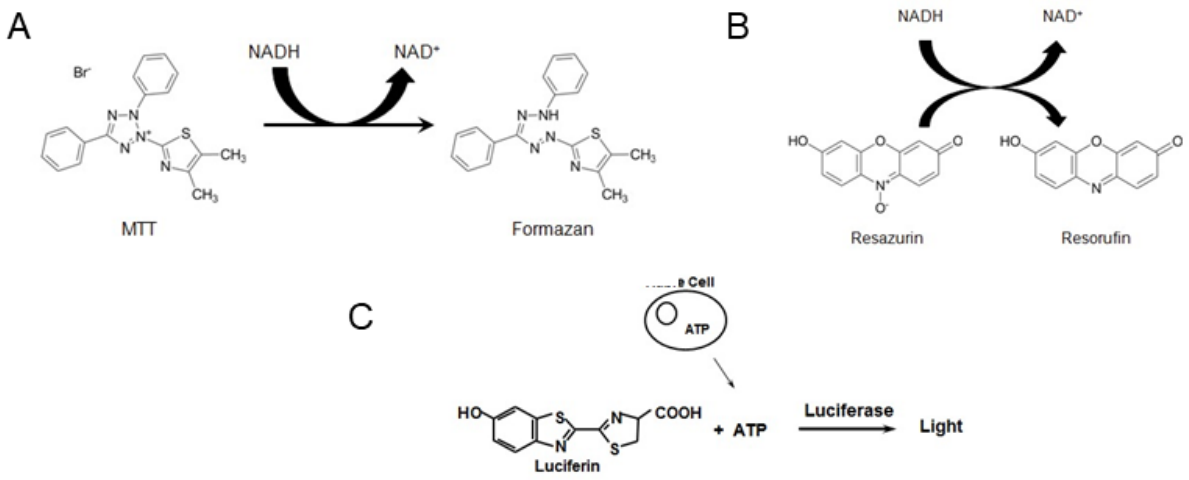

Figure 1.5: Chemical structure and mechanism for commonly used cell death assay markers A) MTT (yellow to purple), B) rezasurin/AlamarBlue (blue/non-fluorescent to pink/fluorescent), and C) Luciferase-based assays like CellTiter-Glo (dark to light). Adapted with permission from reference.[56]

1.4.2 Mechanistic Assays

Mass spectrometry is the premier method for characterizing the lipid oxidation and metabolic products of ferroptosis. It has proved uniquely important in elucidating the relevance of lipid composition and action of enzymes. Specifically, lipidomics have been used in studying the role of PUFA regulatory enzymes and distributions of oxidized lipid species in ferroptosis, such as in Doll and coworkers' seminal work, which identified the role of acyl-CoA synthase 4 (ACSL4) in modulating ferroptosis sensitivity[39] and characterized phosphatidylethanolamines (PE) lipids[37] as being preferentially oxidized. Metabolite quantification, used in the work of the Conrad[42] and Olzmann[43] groups when measuring CoQ_{10} levels, helped to identify the key FSP-1 axis of ferroptosis. Proteomics has also been a key frontier for development, especially in detecting proteins modified by ferroptosis-derived LDEs.[57] Activity-based protein profiling (ABPP), for instance, is a mass spectrometry technique used to identify changes in the availability of nucleophilic sites within the cell milieu. In ABPP, an exogenous electrophile with a pulldown tag is added at saturating concentrations into cell populations, and the negative difference in reactive sites identified between said population and a control population represents the

reactive sites modified by endogenous electrophiles. The Wang group used a meta-aminophenylacetylene (m-APA) probe in ABPP to quantitatively profile LDE modifications in ferroptotic cells and identified over 400 sites of protein modification.[57]

1.4.3 Fluorescence Methods for Measuring Lipid Peroxidation

Fluorescent probes have emerged as a powerful tool for the study of ferroptosis. A number of probes exist to either image the formation of lipid peroxyl radicals or of lipid hydroperoxides. They have been used in high throughput applications outside of simple viability (**Section 1.4.1**) as well as in cell imaging experiments.

Probes for lipid hydroperoxides exist, based commonly on the triphenylphosphine backbone (**Fig. 1.6**). The most commonly used probe is diphenyl-1-pyrenylphosphine (DPPP), which yields a blue (352 nm) fluorescent DPPP oxide product upon reduction of a hydroperoxide into its corresponding hydroxide.[58] Although utilized,[59] the short wavelength makes said probe unsuitable for live cell applications. Spy-LHP was designed to overcome said weakness, detectable at longer wavelengths (535 nm).[60] However its low solubility in cell imaging compatible solvents limited its applications. LiperFluo, a Spy-LHP derivative was later developed and represents the most successful lipid hydroperoxide probe to date.[61] LiperFluo has been utilized by Kagan and coworkers in marking the accumulation of lipid hydroperoxides in lipidomics studies of ferroptosis.[37]

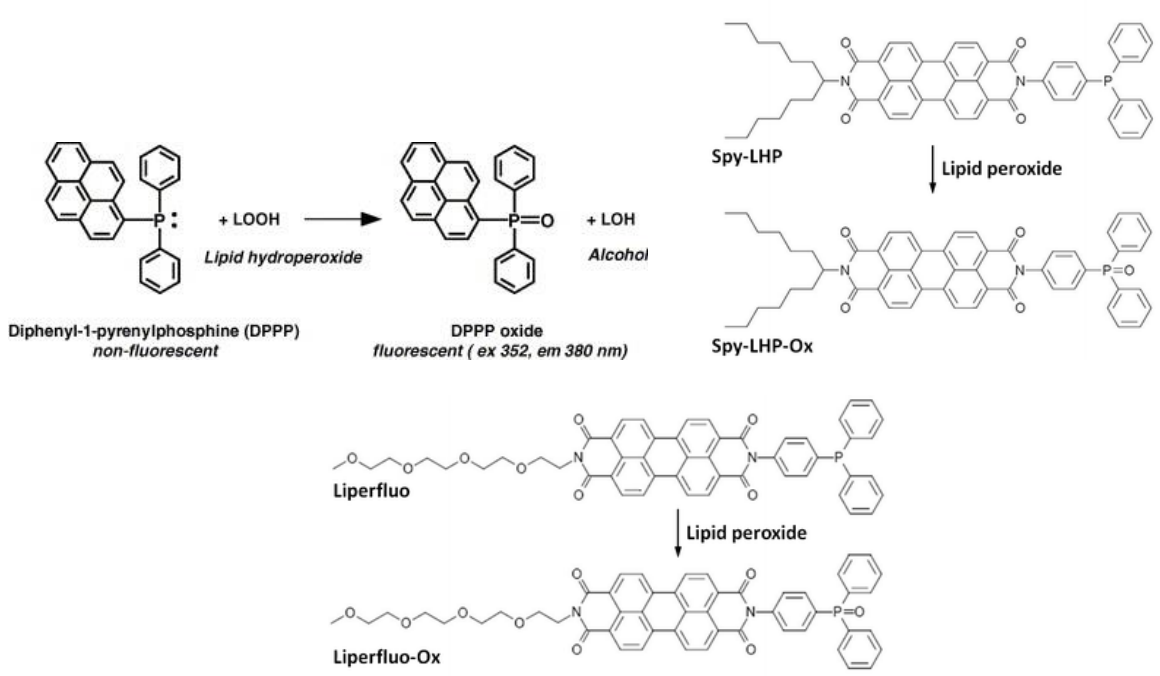

Fig 1.6: probes for lipid hydroperoxides: DPPP, Spy-LHP, and LiperFluo. Reproduced with permission from references 58 and 61.

The commercial probe BODIPY 581/591 C11 (C11 BODIPY).[62] has been the standard to date in the field of ferroptosis. C11 BODIPY is made up of a BODIPY core, a fatty acid tail for anchorage into lipid membranes, and a phenyl group linked to the core via a diene linker. Upon lipid peroxyl radical addition to of the diene linker, the fluorescence of C11 BODIPY shifts from 595nm to 520nm. Here, the degree of oxidation is quantized ratiometrically (oxidized to unoxidized), where this ratiometric assay can be exploited not only in in fluorescence cell sorting applications but also in end-point fluorescence microscopy studies. Oxidation of the diene linker in C11 BODIPY upon reaction with LOO· is analogous to the propagation step of lipid peroxidation in that a new carbon centered radical is initially formed that can trap a molecule of O_2, becoming a peroxyl radical that next may react with additional PUFA. In terms of microscopy, C11 BODIPY is typically used as an endpoint measurement in fixed-cell scenarios post-treatment, instead of in live cell continuous measurements, due to its propensity for internalization, adding ambiguity to spatiotemporal measurements as the distribution of probe is irregular in the cellular

milieu. The usage of C11 BODIPY in more quantitative works has also been cast in doubt, as mass spectrometry studies of fatty acids versus C11 BODIPY oxidation show C11 BODIPY overestimates the extent of lipid peroxidation, due to it being more sensitive to lipid oxidation and exhibiting an antioxidant effect of its own.[63]

Lipid peroxyl radical probes could also be used in high throughput applications for the screening of antioxidant – ferroptosis inhibitor – kinetics. The Cosa group first developed a high throughput well plate fluorescence assay, utilizing a (2nd generation) fluorogenic RTA probes (see below) for measuring the kinetics of peroxyl radical reactions in liposomes.[64] In the presence of competing antioxidants, this assay obtained relative rate constants of H-atom abstraction (k_{inh}) by monitoring the fluorescence of the RTA fluorogenic probe over time, in a rapid and parallel format. FENIX[65] (Fluorescence-ENabled Inhibited autoXidation, **Fig. 1.7** for overview) developed by the Pratt group, makes use of Sty-BODIPY, a fluorogenic BODIPY with an oxidizable alkene moiety, takes inspiration from C11 BODIPY and the high throughput antioxidant competition assay of the Cosa group. The monitoring of antioxidant activity by the co-oxidation of Sty-BODIPY induced by a radical initiator (DTUN) in a model lipid membrane (liposome) environment yielded better adherence to actual degree of ferroptosis protection than a simple measure of antioxidant activity in solution. The FENIX platform has also been recently built upon with endogenous lipid peroxidation initiators[66] to better mimic lipid peroxidation in the cellular milieu for greater physiological relevance.

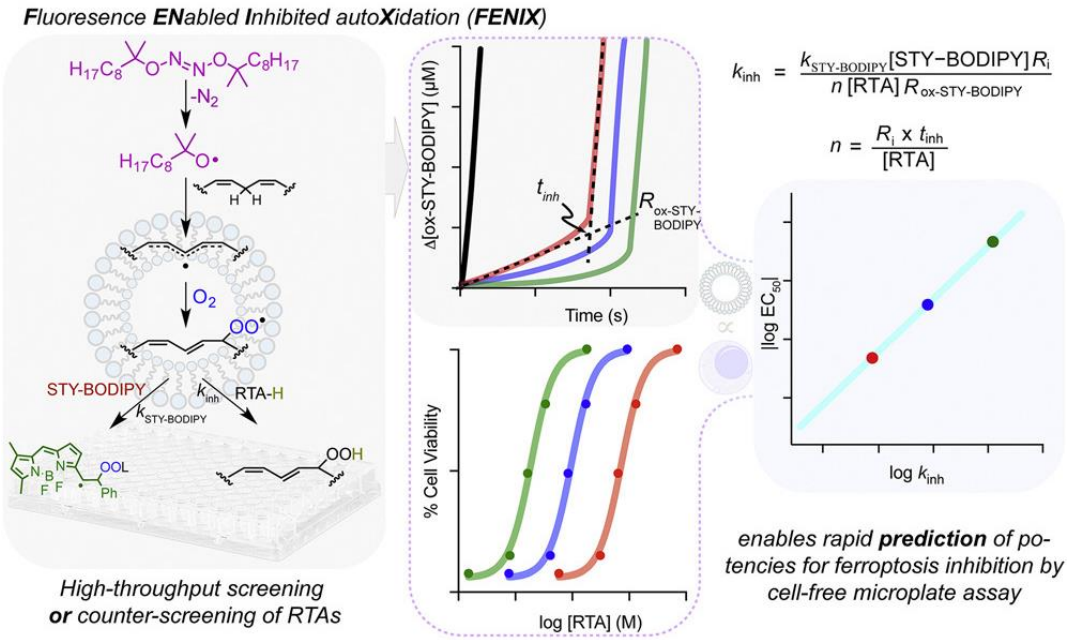

Figure 1.7: Graphical overview of FENIX. Reproduced with permission from reference 65.

The Cosa group has since iteratively developed RTA fluorogenic probes to report spatiotemporally on the generation of lipid peroxyl radicals,[64, 67-70] culminating in H_4B-PMHC,[70] our fourth-generation reporter. Our design principle has remained consistent, connecting the lipid peroxyl radical trapping antioxidant chromanol moiety of α-tocopherol (α-TOH) to a reporter BODIPY fluorophore. In the unoxidized state, the chromanol trap moiety quenches the BODIPY excited state via photoinduced electron transfer (PeT, **Fig. 1.8**). Upon reaction with two equivalents of lipid peroxyl radicals, the chromanol is oxidized, PeT is abolished, and the BODIPY core fluorescence is restored. Iterative improvements of this design by tuning the BODIPY core to be more electron deficient to yield faster rates of PeT,[71] as well as the linker length between the chromanol and BODIPY segments, have improved the dynamic range of the probe from a 22-fold[67] to a 1000-fold[70] enhancement (H_4B-PMHC) in fluorescence upon oxidation.

Our latest probe H_4B-PMHC is amenable to a range of applications due to its extreme sensitivity, including real-time live cell visualization of lipid peroxyl radical generation. Thus, in cell cultures, H_4B-PMHC has been used in the measurement of the basal metabolic rate of lipid peroxyl radical generation

in HeLa cells,[70] in visualizing the extent of lipid peroxidation in lung endothelial cells exposed to cigarette smoke[72] and in measuring antioxidant consumption in neuronal cultures.[73] In bacteria, H_4B-PMHC was employed to resolve the sites of lipid peroxyl radical accumulation.[74] In model membrane systems, H_4B-PMHC has also been used as a fluorescent analogue of α-TOH in spectroelectrochemistry studies,[75] as well as in monitoring singlet oxygen flux in giant unilamellar vesicles.[76] This thesis will describe the use of H_4B-PMHC and related probes in studying ferroptosis progression in live cell imaging.

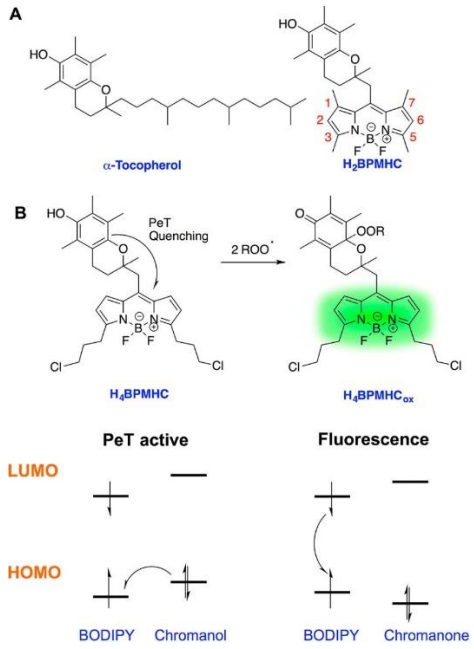

Figure 1.8: (A) Structure of α-TOH and a previously reported, 2nd generation fluorogenic tocopherol analogue. (B) Proposed off/on sensing mechanism of H_4B-PMHC based on PeT. Reproduced with permission from reference 70.

1.5 Live Cell Fluorescence Methodologies

From van Leeuwenhoek's first compound microscopes[77] leading to the first observation of cells[78] to today's super-resolution methods[79-81] blowing well past the diffraction limit to the 1-nanometer scale,[82] the advancements of microscopy cannot be disentangled from the advances in the studies of biological systems. In particular, fluorescence microscopy has become an indispensable component of the modern arsenal to study cell biology, as fluorescent markers can be used to specifically label

substrates of interest with minimal perturbation to cell function. Here an overview of fluorescence microscopy – the key method employed in this thesis is provided. We start the description with fluorophores and recent advances in their usage, to then give details on new imaging techniques enabled by advances in microscopy hardware and software.

1.5.1 Fluorophores

The phenomenon of fluorescence has been observed as early as the fifteenth century.[83] The term fluorescence was first coined by Stokes in 1852[84] as a description of a process of light absorption and emission in his observations of fluorspar (CaF_2) when exposed to light. Since then, a robust understanding of the underlying physics has been developed, serving as the basis of countless platforms.

Photophysical Processes:

Fluorescence and other photophysical processes can best be represented by a Jablonski diagram (**Fig 1.9a**).[85-87] The process begins typically with a molecule (fluorophore) in the singlet electronic ground state (S_0) absorbing a photon of suitable energy (process i, **Fig 1.9a**), promoting an electron into a higher energy orbital (S_n), relaxation then occurs to the lowest electronic excited state (S_1) via a combination of internal conversion and vibrational relaxation (process ii, **Fig. 1.9a**). From S_1, the fluorophore returns to the ground state either by emitting a photon – fluorescence (process iii, **Fig. 1.9a**) – or alternatively, nonradiative processes could also occur to relax the molecule down to the ground state without a photon emission (process iv, **Fig. 1.9a**). Intersystem crossing (ISC) into the spin-forbidden triplet excited state T_1 could also occur (process v, **Fig. 1.9a**), which can subsequently lead to radiative (phosphorescence, process vi, **Fig. 1.9a**) or nonradiative decay back to the ground state (process vii, **Fig. 1.9a**). Further elaboration into triplet state processes and their application will be discussed in **Section 1.5.8** (Photodynamic Therapy).

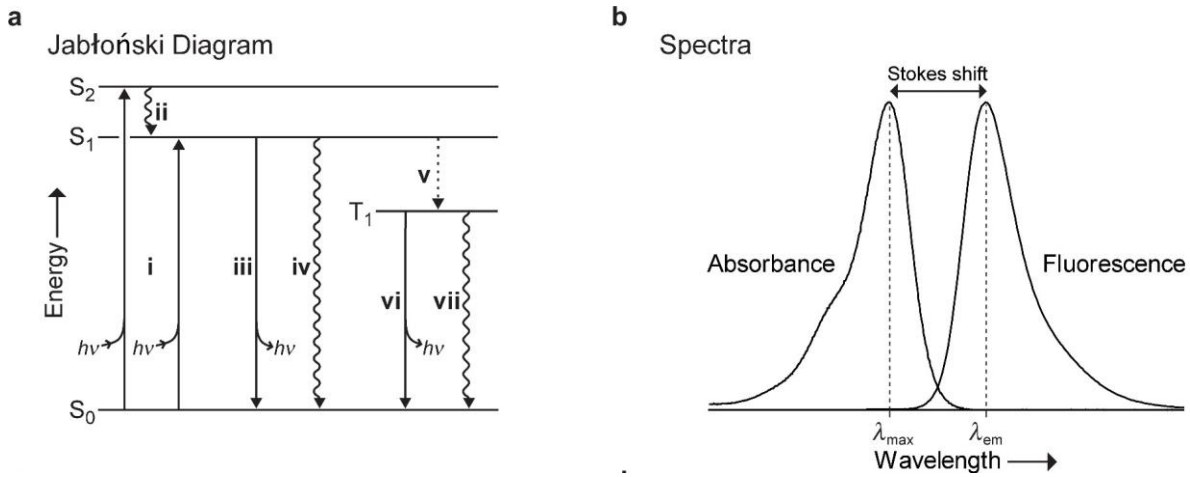

Figure 1.9: A) Jablonski diagram of relevant photophysical processes, highlighting i) absorption of a photon to promote a molecule from the ground to an upper singlet electronic state, ii) vibrational relaxation to S_1, iii) fluorescence, iv) nonradiative decay, v) intersystem crossing to T_1, vi) phosphorescence, and vii) nonradiative decay. B) Absorption and emission spectra of a generic fluorophore. Adapted with permission from reference 85.

Photophysical Properties

The utility of fluorophores comes from the exploitation of their photophysical properties. Fluorophores can be distinguished from each other by their characteristic absorbance and emission, a generic example of which is shown in **Fig 1.9b**. The absorption wavelength maximum (λ_{max}) of a fluorophore corresponds to the most probable absorption wavelength in the absorption band. It is related to the transition energy between S_0 and the excited state Sn, and corresponds to the minimum excitation energy when referring to S_0-S_1 transition(**Fig 1.9a**, i). Upon excitation to S_1, the energy lost in solvent reorganization and other processes redshifts the emission when compared to the absorption, with the difference in λ_{max} and λ_{em} characterized as the Stokes shift, and the intersection of absorption and emission being equal to the value for S_0-S_1 transition energy . To use many dyes in parallel, it is important to consider selecting ones without spectral overlap, so individual dyes can be uniquely excited and visualized. For usages of fluorophores as a measure of concentration, a high signal-to-noise ratio, or brightness, is desirable. The absorptivity of a fluorophore (at λ_{max}) can be expressed by the extinction coefficient (ε), as defined by the Beer-Lambert law. The emission quantum yield (ϕ) is a measure of the

probability of a dye to decay from S_1 (or upper excited state) via fluorescence (**Fig 1.9**, iii). It is the proportion of emitted photons to all photons absorbed, essentially the efficiency of a dye to fluoresce. The ideal fluorophore – one with the maximal output of photons – is one which has high ε and a high ϕ, where the product of the two is termed molecular brightness.[88] For fluorophores with overlapping spectral emissions, the lifetime of the excited state (τ) can be used as an alternative discriminant in fluorescence polarization[89] or lifetime imaging.[90]

Types of fluorophores:

The principal classes of fluorophores typically used in cell imaging applications are fluorescent proteins and organic dyes. While lanthanide[91] and semiconductor nanocrystals (quantum dots)[92] have been deployed, their biocompatibility remains a huge hurdle best overcome by sidestepping it altogether. These latter materials will not be elaborated upon further.

Fluorescent proteins, such as those derived from the original *Aequorea victoria* jellyfish[93], present the advantage of being easy to use and highly biocompatible. Their application was first demonstrated post-cloning[94] and genetically-encoded to a target gene to track its expression in nematodes.[95] Currently a plethora of options exist due to the explosion of protein engineering, creating a palette of different colours and brightness[96] to choose from, accessible to the labeling of specific protein targets via routine molecular biology.

Small molecule organic dyes have the advantage of being synthetically flexible, with many opportunities for functionalization with chemically reactive handles for either cross linkages or fluorogenicity.[88] Many families of dyes across the visible (and near IR) spectra have been developed and are highlighted in **Figure 1.10**, presenting a very enticing array to choose from in multiplexing. In addition to photophysical properties (λ_{max}, λ_{em}, ε, ϕ, τ), here additional criteria such as the pK_a,

chemical/photostability, toxicity, and dye localization can serve as the basis for selection based on application.

The boron-dipyrromethene (BODIPY) backbone for our fluorogenic probes has been developed upon in the Cosa lab over the past decade.[67, 69, 70, 97] Correspondingly, the probes utilized in this thesis are BODIPY-based. BODIPYs in this application have many advantages, including their high quantum yield (ϕ ~1 for typical BODIPY core), high stability across the range of physiologically-relevant conditions, facile synthesis and functionalization, and high lipophicity – for ease of partitioning into lipid membranes. As this work is focused on imaging methodologies, the synthetic schemes and characterizations of various probes is outside of the scope of investigation and will not be discussed.

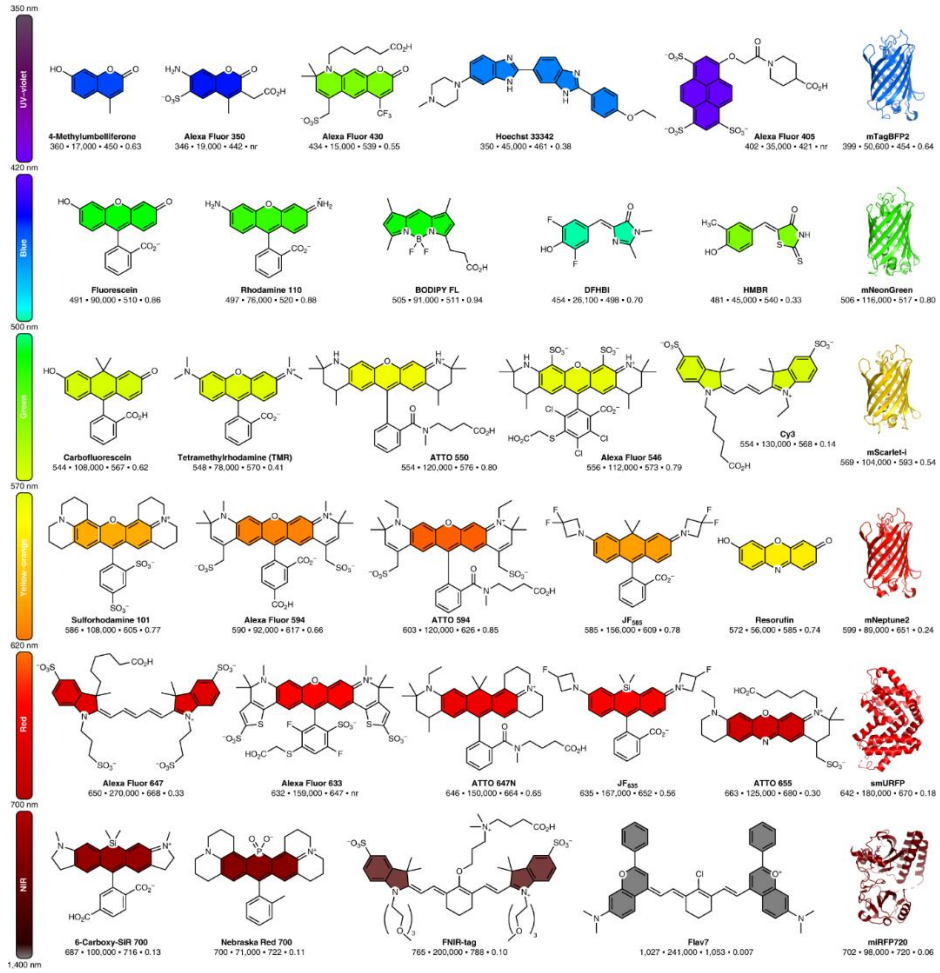

Figure 1.10: Survey of major fluorophore families arranged by wavelength. Reproduced with permission from reference.[88]

1.5.2 Fluorescence Microscopy

Fluorescence microscopy is an extremely versatile platform that can be adapted for qualitative and quantitative, static and dynamic, physical and organic systems. In the Cosa group alone, imaging has been the technique of choice for studying the dynamics of protein binding,[98] the assembly of DNA nanostructures,[99] the photophysical properties of materials,[100] and chemical reactions in membranes.[75] As this work is primarily interested in cellular processes, a focus will be placed on live cell imaging.

Widefield microscopy - meaning the whole sample is illuminated, as opposed to nearfield microscopy[101] – is broadly used for cell imaging. Typically, this method is employed in the epifluorescence modality, meaning the objective lens is used to both excite and collect light from the sample. The sample is illuminated with a light source of adequate power and spectrally filtered for the correct wavelengths. Lasers are nowadays implemented in most systems due to their high output and their capability for precise wavelength tuning. Upon excitation, the emission is then collected back through the objective lens, filtered for the specified wavelengths, and captured by a camera. High sensitivity image sensor setups, such as electron-multiplying charged coupled devices (EMCCDs) and scientific- complementary metal oxide semiconductors (sCMOSs) allow for fast acquisition rates (~ms time resolution), along with incredible sensitivity (>90% quantum efficiency).

1.5.3 Total Internal Reflection Fluorescence (TIRF)

TIRF is a widefield technique in which illumination occurs at an angle greater than the critical angle of refraction between two interfaces of different refractive indices.[102] Typically, these interfaces consist of an aqueous sample (n_1 = 1.33) and a glass coverslip (n_2 = 1.52). When the angle of illumination exceeds the critical angle, total internal reflection occurs, the incident light is reflected into itself, and an evanescent wave is generated at the glass-water interface that decays exponentially with distance into the water. The spatial confinement (d) of the evanescent field is a function of the angle of incidence past

the critical angle (θ) and the wavelength of excitation. It is approximately 150nm for the visible light range.

$$d = \frac{\lambda}{4\,\pi}(n_2{}^2 \sin^2\theta - n_1{}^2)^{1/2}$$

TIRF mitigates problems associated with background, as chromophores/impurities away from the surface are not excited, creating a superior signal-to-background ratio capable of discriminating fluorophores from background at the single molecule level.[103] TIRF is thus the illumination method of choice for single molecule fluorescence microscopy as well as many super-resolution methods (**Section 1.5.6**).[104]

1.5.4 Highly Inclined and Laminated Optical Sheet (HILO)

While TIRF enables the visualization of fluorophores down to the single molecule level, it is a surface phenomenon that is very limiting for biological systems, as cells are microns in thickness. To this end, HILO[105] is more amenable to obtaining useful information. Here, slightly less oblique illumination than that used in TIRF results in an optical sheet of approximately one micron in thickness, passing through the centre of the sample of interest. Signal-to-background is good, as in TIRF, due to the lack of background excitation, albeit slightly less so when, for instance, the bulk of the cytosolic content of an adherent cell is illuminated. See **Figure 1.11** for a comparative illustration of the epifluorescence, TIRF, and HILO illumination angles.

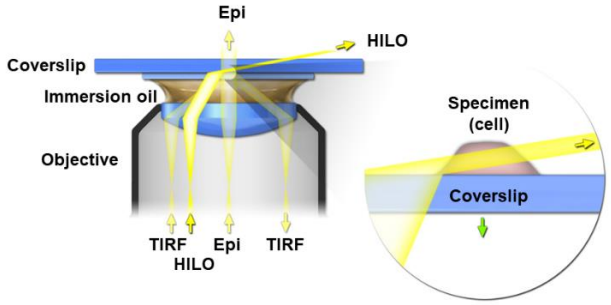

Figure 1.11: Angle of illumination for widefield microscopy: epifluorescence, TIRF, and HILO. Figure adapted from reference 106.[106]

1.5.5 Confocal Microscopy

Confocal microscopy encompasses a broad class of techniques commonly used in cell imaging.[107] In contrast to widefield techniques, confocal techniques produce a series of optical slices by occluding out-of-focus light. This is achieved by focusing the light through a carefully aligned pinhole (in the CONjugate FOCAL plane of the sample), ensuring only fluorescence that originates from the focal plane is captured. Two major implementations of confocal techniques exist: laser scanning confocal microscopy (LSCM) and spinning disk confocal microscopy (SDCM). In LSCM, scanning mirrors are used to raster the laser light source across the sample one pixel at a time. Acquisition times are relatively slow, precluding fast dynamics. Typically, a photomultiplier tube (PMT) is used instead of a camera, as intensity is assigned to one pixel at a time (point detector). SDCM excites and images the sample in parallel from multiple points.[108] By utilizing an array of pinholes on a disk spinning at a high frequency (5000-10000 rpm), out of focus light can be rejected while achieving an even illumination of the entire sample. Acquisition time is thus improved, allowing for the use of array detectors (cameras) instead of point detectors (PMT). See **Figure 1.12** for a graphical overview of both LSCM and SDCM.

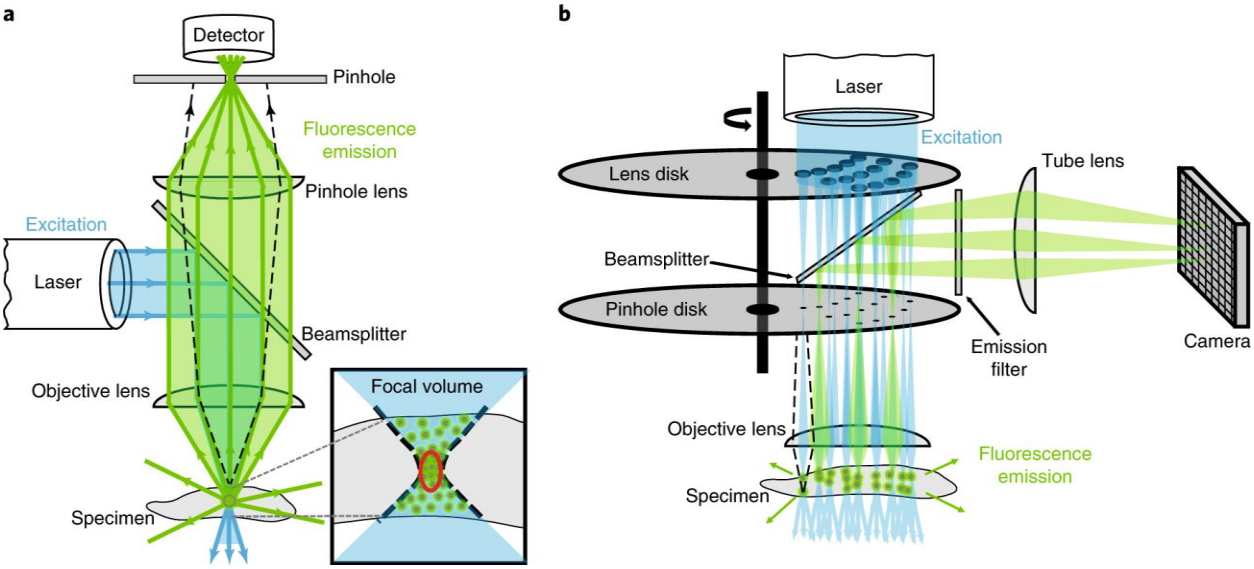

Figure 1.12: Overview of a) LSCM and b) Yokogawa-based SDCM, where the laser is focused with an array of lenses (a lens disk) aligned with the pinhole disk. Reproduced with permission from reference.[109]

1.5.6 Super-Resolution Microscopy

Ernst Abbe derived the theoretical fundamental resolution limit to optical microscopy[110] 150 years ago, stating it as a function of the numerical aperture (NA) of the objective and the wavelength of emitted light. Diffraction limited resolutions of approximately 200 nm and 500 nm are thus calculated laterally and axially respectively, and attained with a high (~1.4) NA objective for a wavelength of 500 nm.

$$d_{XY} = \frac{\lambda}{2\,NA}$$

$$d_Z = \frac{2\lambda}{(NA)^2}$$

The diffraction limited resolution is on the size scale of many organelles and bacteria, meaning more invasive methodologies such as electron microscopy must be used to acquire intracellular details.

Starting in the early 1990s and 2000s, methods for circumventing the diffraction limit of light began to emerge, leading to the Nobel Prize in Chemistry in 2014 awarded for the development of two such methods.[111] Broadly, the two strategies for beating the diffraction limit of light are: 1) point spread function (PSF) engineering and 2) single molecule localization (**Fig. 1.13**).

STED (STimulated Emission Depletion) is a point-scanning confocal technique (**Section 1.5.5**) first theorized[112] and realized[81] by Stefan Hell, by which resolution can be enhanced by depleting fluorophore emission in the outer region of the diffraction limited spot. Stimulated emission can be achieved by using a laser of longer wavelength, forcing the excited fluorophore to relax to a higher vibrational state than the fluorescence transition, causing a red shifted photon separable/ignorable from the normal fluorescence of the fluorophore. Thus, by engineering a donut shaped depletion beam over the excitation beam, the periphery of the excitation PSF can be depleted thus confining the emission to a sub-diffraction limited zone. Resolution enhancement here follows the relationship:

$$d_{XY} = \frac{\lambda}{2\,NA\,\sqrt{1+\sigma}}$$

Where the saturation factor (σ) is a function of the peak intensity of the excitation laser (I_{max}) and the threshold intensity required to achieve saturated emission depletion (I_{sat}):

$$\sigma = I_{max}/I_{sat}$$

Improvements in resolution can be made down to ~50 nm.[113]

SMLM (single molecule localization microscopy) methods separate single, diffraction-limited fluorophores in time, before separating them in space. This has been achieved in various ways using different fluorophores, in techniques such as PALM[80] (Photoactivated Localization Microscopy, using fluorescent proteins proposed by Eric Betzig) and STORM[79] (Stochastic Optical Reconstruction Microscopy, using cyanine dyes, proposed by Xiaowei Zhuang). By capturing thousands of frames of photoswitchable fluorophores under conditions such that only a small subset of diffraction-limited fluorophores is emitting, computational analysis can be done to pinpoint the centres of emitting molecules and reconstruct a map of super-resolved emissions (fitting a point spread function). The improved localization precision ($d_{localization}$) of the fluorophore thus scales with the number of photons collected (N) for each fluorophore imaged:

$$d_{localization} = \frac{d}{\sqrt{N}}$$

Improvement in resolution down to ~50 nm can be routinely achieved, with ~10nm range accessible with further optimization.[113]

MINFLUX,[82] a revolutionary new technique, is capable of achieving sub-nm resolution. Similar to STED, but flipping the paradigm on its head, MINFLUX makes use of a donut-shaped incident beam. A spot of zero intensity exists in the center of the excitation beam, at which point a fluorophore positioned there would exhibit no intensity. MINFLUX moves the excitation donut to encircle

fluorophores until it is positioned at the position of minimum signal directly in the centre of the excitation donut. This technique drastically reduces the number of photons required for image acquisition compared to STED.

The advent of super-resolution methods has led to important discoveries in cell biology. To highlight a few specific examples, the Zhuang group discovered the periodic cytoskeletal structure in neuron axons/dendrites using STORM.[114] The Jakobs group, using live cell STED, resolved mitochondria cristae dynamics for the first time and the distribution of mitochondria nucleoids.[115] MINFLUX,[82] still in its infancy, has already been used to track the movement of individual kinesin motor proteins making discrete ~4nm length steps along microtubules in 3D.[116]

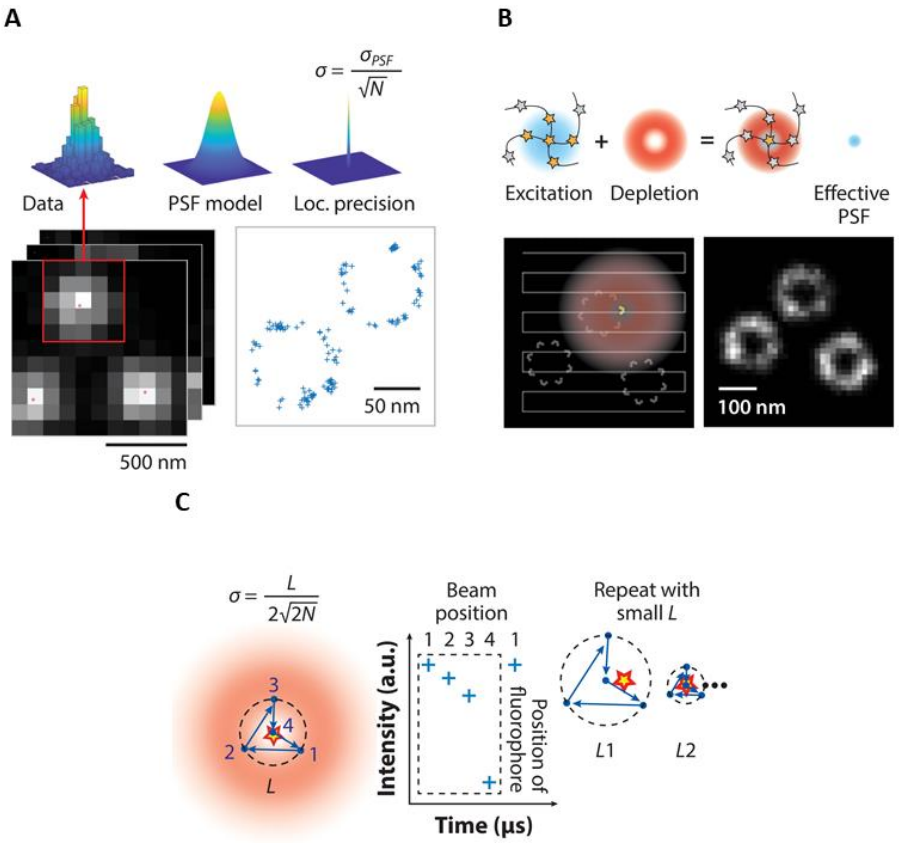

Figure 1.13: Overview of A) SMLM, B) STED, and C) MINFLUX. Reproduced with permission from reference.[117]

1.5.7 Alternative Methods for Super-Resolution

Super-resolution methods such as STED and SMLM do not come without significant trade-offs, which has led to a desire for mitigation. Both techniques require laser power at ranges which can impact cell viability,[118] as the resolution increase in STED is directly proportional to the intensity of the depletion donut and SMLM techniques require high laser power in order to achieve the desired fluorophore photoswitching dynamics. In addition, SMLM, requiring the collection of thousands of frames – over the course of minutes or longer – precludes the possibility of capturing fast dynamic processes.

Structured illumination microscopy (SIM) is a widefield technique that utilizes a periodically patterned illumination field to generate interference with labeled structures in the sample, from which an image of the structure can be calculated at a resolution beyond the diffraction limit.[119] While not requiring high laser power or long acquisition times, SIM is physically limited to a twofold increase in resolution (~150 nm, compared to ~20 nm for SMLM). As such, the above listed techniques all possess caveats for live cell imaging.

Super-resolution Optical Fluctuation Imaging is a computational super-resolution technique exploiting the correlation of light from individual fluorophores.[120] The fundamental idea is that capturing a series of images (~100 to ~1000 frames) over time using a fluorophore with stochastic, time-dependent fluctuations (not moving, only varying in intensity over time/blinking), enhancing the intensity of pixels correlated over time (signal) and diminishing the intensity of pixels uncorrelated in time (noise, out of focus light), will lead to resolution enhancement. The resolution improvement with SOFI scales with the number of orders of correlation (correlating n measurements at a time), by a factor of $\sqrt{n}$.

SRRF (super-resolution radial fluctuations)[121, 122] is a method pioneered by the Henriques lab which circumvents many of the challenges of super-resolution when applied to live cells. As in SMLM, higher resolution data is created from a sequential series of frames. However, unlike SMLM, there is no requirement for sparse distribution of fluorophores – thus, it enables working on densely labeled samples at low laser power. Additionally, there is no requirement for blinking fluorophores (like in SOFI). In brief, the analysis is split in two steps, 1) localization by radiality and 2) de-noising by temporal correlation. In the first step, an intensity gradient vector is assigned to each pixel, pointing to the direction of highest pixel intensity in a ring of neighbouring pixels. A radiality score is then assigned to each pixel, as a measure of how well the gradient vectors in the local environment converge, with high radiality as a proxy for the position of the fluorophore, as microscope point spread functions are radially symmetric (**Fig. 1.14**). The second step of the analysis examines the temporal correlation of the map of radiality, with the reasoning that while signal is highly temporally correlated, noise is random and temporally uncorrelated. The final map of temporal correlation can then be rendered as a SRRF image, with a resolution of ~70 nm.[121] For this thesis, SRRF is employed in **Chapter 2** and **Chapter 4** as the best compromise between biological relevance, temporal sampling, and image resolution.

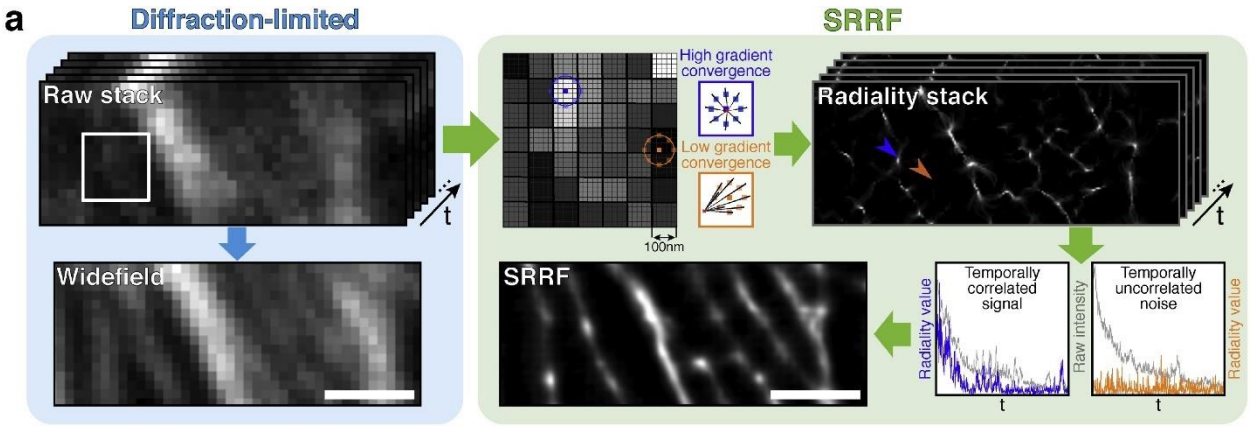

Figure 1.14: Workflow of SRRF analysis. The cyan box highlights the raw data of a stack of diffraction-limited images, and the green box highlights the analysis process of radiality assignment and temporal correlation analysis. Reproduced with permission from reference.[122]

1.5.8 Photodynamic Therapy (PDT)

The therapeutic applications of light date back to antiquity, with many ancient civilizations prescribing various plant extracts and sun exposure for treatment of skin diseases.[123] Modern phototherapy began in the early twentieth century, exemplified by Niels Finsen, whose work on the subject was awarded the Nobel Prize in 1903.[124] The discovery of the tumour-localizing ability of haematoporphyrin along with its phototoxic effect on tumour cells led to the development of PDT.[125]

PDT relies on the action of a photosensitizer, light, and oxygen. Molecular oxygen in its ground state exists as a triplet ($^3O_2$), rendering it electronically inert towards the vast majority of molecules which are singlets.[87] A photosensitizer – a chromophore which upon absorption of a suitable wavelength of light and excitation to the singlet excited state (**Section 1.5.1**, **Fig. 1.9a**), efficiently undergoes ISC to the triplet excited state – is needed to facilitate the reaction of $^3O_2$ with biomolecules to achieve the desired effect of inactivation. Here Dexter energy transfer (nonradiative energy transfer of the excited state, also known as triplet-triplet annihilation) between the excited triplet state of the photosensitizer and the ground state triplet oxygen takes place through a spin allowed process,[127] to yield a ground state photosensitizer and molecular oxygen in the excited singlet state $^1O_2$, commonly known as singlet oxygen. Of note, singlet oxygen can also be sensitized from the singlet excited state of photosensitizers, provided the singlet triplet gap for the photosensitizer is larger in energy than the excitation energy required to form singlet oxygen. Inactivation by singlet oxygen is known as Type II PDT.[127] To attain efficient ISC in the photosensitizer, one may take advantage of the heavy atom effect, a phenomenon where increased intersystem crossing efficiency is attained by the chromophore substitution with high atomic number atoms. Here increased ISC is due to spin-orbit coupling.[126] The photosensitizer in the triplet excited state can also interact with a substrate (biomolecule) via hydrogen atom or electron transfer[87] (Type I PDT), generating radical species which can then further react with $^3O_2$ to form ROS

(**Section 1.2.2**). Type II PDT represents the dominant mechanism in the literature, with most photosensitizers producing $^1O_2$.

While the lifetime of $^1O_2$ is short, when in proximity with membranes, $^1O_2$ can undergo the *ene* reaction with unsaturated lipids to produce lipid hydroperoxides (**Fig 1.15**, also **Section 1.2.4** for the implications of lipid peroxidation).

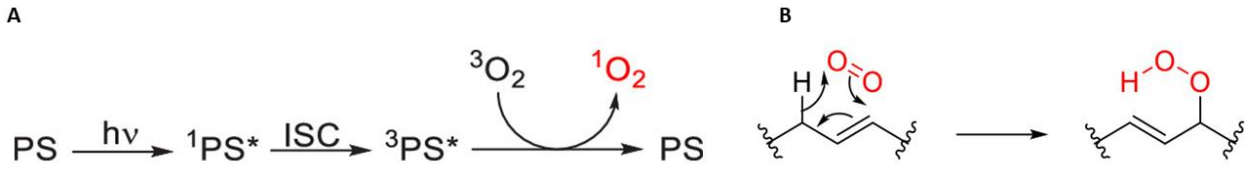

Figure 1.15: A) Mechanism of type II photosensitization to produce $^1O_2$. B) Ene reaction of singlet oxygen with unsaturated lipid to generate a lipid hydroperoxide. Reproduced with permission reference 14.

The general principle of PDT is to deliver a photosensitizer to a targeted cell possessing a disease pathology and to utilize light and oxygen to generate ROS for its elimination. PDT has been broadly deployed over the years in cancer treatments,[128] and in inactivating microorganisms such as bacteria[129] (PDI, photodynamic inactivation). As ROS react non-specifically, spatial control over the activation of photosensitizers to mitigate damage to healthy cells is of utmost importance.

The Cosa group has designed a novel approach to adding an extra layer of control to photosensitization, with the incorporation of a chemical cue for photosensitizer activation (**Fig. 1.16**).[130] Reasoning that activating a photosensitizer specifically in regions under high oxidative stress could contribute to the discrimination of diseased versus healthy tissue, heavy atoms (bromines) were added to our fluorogenic probes for ROS[69] to create a dormant photosensitizer. This design principle was validated in bacterial inactivation, showing selective killing in ROS-stressed *E. coli* over basal.

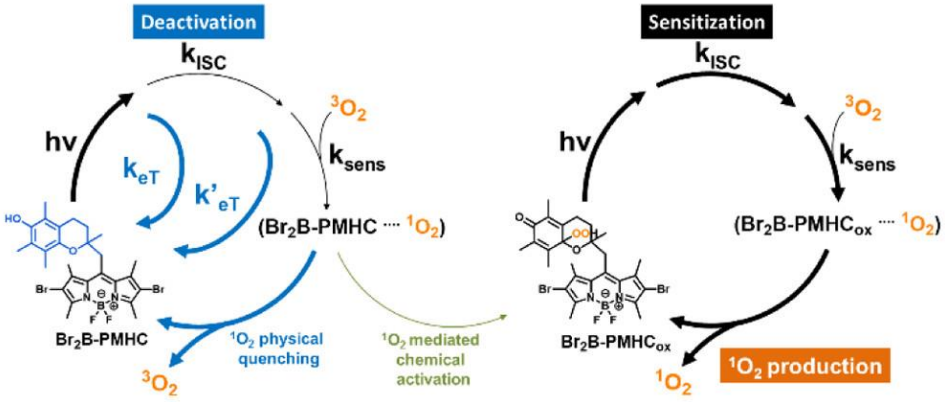

Figure 1.16: Dormant photosensitizer (DoPS) controlled by quenching of the BODIPY photosensitizer segment via PeT by the chromanol segment. Singlet oxygen sensitization is activated in environments of high ROS, providing an extra layer of control over photosensitization. Reproduced with permission from reference 130.

1.6 Goals and Scope of Thesis

Live cell imaging can be used to gain insights into fundamental biological processes, as events can be observed from start to finish with minimal perturbation. Fluorogenic probes that turn on/off with chemical reactivity add another dimension of information on top of the conventional utilization of fluorophores as positional markers, allowing for the quantization of concentration and kinetics.

This thesis sets out to develop a toolkit for the usage of a series of fluorogenic probes responding to lipid peroxidation-related species and to demonstrate potential use-case scenarios for the study of oxidative stress-related cell death in the field at large.

Chapter 2 summarizes our usage of a palette of tocopherol-bearing fluorogenic probes in examining ferroptosis. In what is the first reported real-time observation of ferroptotic cell death from induction to completion, we record with H_4B-PMHC the sequence of events in which cell death progresses, as a physical process stemming from the total consumption of membrane antioxidant. With organelle-targeting PMHC-bearing probes, we demonstrate the trafficking pathway of oxidized lipids from the interior of the cell to the plasma membrane.

Extending our work in detecting lipid peroxidation, we use the probe H_3BrB-PMHC to induce oxidative stress in **Chapter 3**. Here, we introduce the concept of a dormant photosensitizer, an autocatalytic probe which reports ROS while also generating ROS, for the dual purpose of cell imaging and cell killing. We demonstrate spatial specificity in probe activation for photodynamic therapy as well as hot spots of ROS sensitivity within cells, paving the path for theragnostic applications.

Chapter 4 involves examining the chemistry of lipid-derived electrophiles, downstream breakdown products of lipid peroxidation, with the LDE-mimicking probe cyanoAcroB. Tuned to reversibly react with cellular nucleophiles, cyanoAcroB reports on individual reaction events while never accumulating fluorescent products, making it uniquely suitable for the high signal-to-noise requirements of super-resolution microscopy. We show here the capability of cyanoAcroB to produce live cell super-resolution images on the hour timescale in a proof-of-principle application to ferroptosis.

Taken together, this thesis contributed to our understanding of ferroptosis – its process, its intracellular regions of importance, and the fate of its oxidized lipid byproducts. The investigations set out in this work provide an arsenal of methodologies for investigating future problems in the field of oxidative stress biology.

1.7 References

(1) Cavalazzi, B.; Lemelle, L.; Simionovici, A.; Cady, S. L.; Russell, M. J.; Bailo, E.; Canteri, R.; Enrico, E.; Manceau, A.; Maris, A.; et al. Cellular remains in a ~3.42-billion-year-old subseafloor hydrothermal environment. *Sci Adv* **2021**, *7* (29). DOI: 10.1126/sciadv.abf3963 From NLM.
(2) Canfield, D. E.; Ngombi-Pemba, L.; Hammarlund, E. U.; Bengtson, S.; Chaussidon, M.; Gauthier-Lafaye, F.; Meunier, A.; Riboulleau, A.; Rollion-Bard, C.; Rouxel, O. Oxygen dynamics in the aftermath of the Great Oxidation of Earth's atmosphere. *Proceedings of the National Academy of Sciences* **2013**, *110* (42), 16736-16741.
(3) Halliwell, B.; Gutteridge, J. M. C. *Free Radicals in Biology and Medicine*; Oxford University Press, 2015. DOI: 10.1093/acprof:oso/9780198717478.001.0001.
(4) Olejarz, J.; Iwasa, Y.; Knoll, A. H.; Nowak, M. A. The Great Oxygenation Event as a consequence of ecological dynamics modulated by planetary change. *Nature Communications* **2021**, *12* (1), 3985. DOI: 10.1038/s41467-021-23286-7.
(5) Sies, H.; Belousov, V. V.; Chandel, N. S.; Davies, M. J.; Jones, D. P.; Mann, G. E.; Murphy, M. P.; Yamamoto, M.; Winterbourn, C. Defining roles of specific reactive oxygen species (ROS) in cell biology and physiology. *Nature Reviews Molecular Cell Biology* **2022**, *23* (7), 499-515. DOI: 10.1038/s41580-022-00456-z.
(6) Yu, T.-W.; Anderson, D. Reactive oxygen species-induced DNA damage and its modification: a chemical investigation. *Mutation Research/Fundamental and Molecular Mechanisms of Mutagenesis* **1997**, *379* (2), 201-210.
(7) Farmer, E. E.; Mueller, M. J. ROS-mediated lipid peroxidation and RES-activated signaling. *Annual review of plant biology* **2013**, *64*, 429-450.
(8) Cabiscol Català, E.; Tamarit Sumalla, J.; Ros Salvador, J. Oxidative stress in bacteria and protein damage by reactive oxygen species. *International Microbiology, 2000, vol. 3, núm. 1, p. 3-8* **2000**.
(9) Harraan, D. Aging: a theory based on free radical and radiation chemistry. **1955**. Stefanatos, R.; Sanz, A. The role of mitochondrial ROS in the aging brain. *FEBS Letters* **2018**, *592* (5), 743-758. DOI: https://doi.org/10.1002/1873-3468.12902.
(10) Harris, I. S.; DeNicola, G. M. The Complex Interplay between Antioxidants and ROS in Cancer. *Trends in Cell Biology* **2020**, *30* (6), 440-451. DOI: 10.1016/j.tcb.2020.03.002 (acccessed 2023/08/10).
(11) Zhou, Y.; Zhen, Y.; Wang, G.; Liu, B. Deconvoluting the Complexity of Reactive Oxygen Species (ROS) in Neurodegenerative Diseases. *Frontiers in Neuroanatomy* **2022**, *16*, Mini Review. DOI: 10.3389/fnana.2022.910427.
(12) Chen, Y.; Fang, Z.-M.; Yi, X.; Wei, X.; Jiang, D.-S. The interaction between ferroptosis and inflammatory signaling pathways. *Cell Death & Disease* **2023**, *14* (3), 205.
(13) Kawagishi, H.; Finkel, T. Unraveling the Truth About Antioxidants: ROS and disease: finding the right balance. *Nature Medicine* **2014**, *20* (7), 711-713. DOI: 10.1038/nm.3625.
(14) Foret, M. K.; Lincoln, R.; Do Carmo, S.; Cuello, A. C.; Cosa, G. Connecting the "Dots": From Free Radical Lipid Autoxidation to Cell Pathology and Disease. *Chemical Reviews* **2020**, *120* (23), 12757-12787. DOI: 10.1021/acs.chemrev.0c00761.
(15) Pratt, D. A.; Mills, J. H.; Porter, N. A. Theoretical Calculations of Carbon−Oxygen Bond Dissociation Enthalpies of Peroxyl Radicals Formed in the Autoxidation of Lipids. *Journal of the American Chemical Society* **2003**, *125* (19), 5801-5810. DOI: 10.1021/ja034182j.
(16) Yin, H.; Xu, L.; Porter, N. A. Free radical lipid peroxidation: mechanisms and analysis. *Chemical reviews* **2011**, *111* (10), 5944-5972.
(17) Shah, R.; Shchepinov, M. S.; Pratt, D. A. Resolving the Role of Lipoxygenases in the Initiation and Execution of Ferroptosis. *ACS Central Science* **2018**, *4* (3), 387-396. DOI: 10.1021/acscentsci.7b00589.

(18) Dixon, S. J.; Lemberg, K. M.; Lamprecht, M. R.; Skouta, R.; Zaitsev, E. M.; Gleason, C. E.; Patel, D. N.; Bauer, A. J.; Cantley, A. M.; Yang, W. S. Ferroptosis: an iron-dependent form of nonapoptotic cell death. *cell* **2012**, *149* (5), 1060-1072.
(19) Stockwell, B. R.; Friedmann Angeli, J. P.; Bayir, H.; Bush, A. I.; Conrad, M.; Dixon, S. J.; Fulda, S.; Gascón, S.; Hatzios, S. K.; Kagan, V. E.; et al. Ferroptosis: A Regulated Cell Death Nexus Linking Metabolism, Redox Biology, and Disease. *Cell* **2017**, *171* (2), 273-285. DOI: 10.1016/j.cell.2017.09.021 From NLM.
(20) Jiang, X.; Stockwell, B. R.; Conrad, M. Ferroptosis: mechanisms, biology and role in disease. *Nature Reviews Molecular Cell Biology* **2021**, *22* (4), 266-282. DOI: 10.1038/s41580-020-00324-8.
(21) Kerr, J. F.; Wyllie, A. H.; Currie, A. R. Apoptosis: a basic biological phenomenon with wideranging implications in tissue kinetics. *British journal of cancer* **1972**, *26* (4), 239-257.
(22) Arya, R.; White, K. Cell death in development: Signaling pathways and core mechanisms. *Semin Cell Dev Biol* **2015**, *39*, 12-19. DOI: 10.1016/j.semcdb.2015.02.001 From NLM.
(23) Peng, F.; Liao, M.; Qin, R.; Zhu, S.; Peng, C.; Fu, L.; Chen, Y.; Han, B. Regulated cell death (RCD) in cancer: key pathways and targeted therapies. *Signal Transduction and Targeted Therapy* **2022**, *7* (1), 286. DOI: 10.1038/s41392-022-01110-y.
(24) Cookson, B. T.; Brennan, M. A. Pro-inflammatory programmed cell death. *Trends in microbiology* **2001**, *9* (3), 113-114.
(25) Brinkmann, V.; Reichard, U.; Goosmann, C.; Fauler, B.; Uhlemann, Y.; Weiss, D. S.; Weinrauch, Y.; Zychlinsky, A. Neutrophil Extracellular Traps Kill Bacteria. *Science* **2004**, *303* (5663), 1532-1535. DOI: 10.1126/science.1092385 (acccessed 2023/08/11).
(26) Tsvetkov, P.; Coy, S.; Petrova, B.; Dreishpoon, M.; Verma, A.; Abdusamad, M.; Rossen, J.; Joesch-Cohen, L.; Humeidi, R.; Spangler, R. D.; et al. Copper induces cell death by targeting lipoylated TCA cycle proteins. *Science* **2022**, *375* (6586), 1254-1261. DOI: doi:10.1126/science.abf0529.
(27) Liu, X.; Nie, L.; Zhang, Y.; Yan, Y.; Wang, C.; Colic, M.; Olszewski, K.; Horbath, A.; Chen, X.; Lei, G.; et al. Actin cytoskeleton vulnerability to disulfide stress mediates disulfidptosis. *Nature Cell Biology* **2023**, *25* (3), 404-414. DOI: 10.1038/s41556-023-01091-2.
(28) Galluzzi, L.; Vitale, I.; Aaronson, S. A.; Abrams, J. M.; Adam, D.; Agostinis, P.; Alnemri, E. S.; Altucci, L.; Amelio, I.; Andrews, D. W. Molecular mechanisms of cell death: recommendations of the Nomenclature Committee on Cell Death 2018. *Cell Death & Differentiation* **2018**, *25* (3), 486-541.
(29) Eagle, H.; Piez, K. A.; Oyama, V. I. The biosynthesis of cystine in human cell cultures. *Journal of Biological Chemistry* **1961**, *236* (5), 1425-1428.
(30) Tan, S.; Schubert, D.; Maher, P. Oxytosis: a novel form of programmed cell death. *Current topics in medicinal chemistry* **2001**, *1* (6), 497-506.
(31) Seiler, A.; Schneider, M.; Förster, H.; Roth, S.; Wirth, E. K.; Culmsee, C.; Plesnila, N.; Kremmer, E.; Rådmark, O.; Wurst, W. Glutathione peroxidase 4 senses and translates oxidative stress into 12/15-lipoxygenase dependent-and AIF-mediated cell death. *Cell metabolism* **2008**, *8* (3), 237-248.
(32) Dolma, S.; Lessnick, S. L.; Hahn, W. C.; Stockwell, B. R. Identification of genotype-selective antitumor agents using synthetic lethal chemical screening in engineered human tumor cells. *Cancer cell* **2003**, *3* (3), 285-296.
(33) Yang, W. S.; Stockwell, B. R. Synthetic Lethal Screening Identifies Compounds Activating Iron-Dependent, Nonapoptotic Cell Death in Oncogenic-RAS-Harboring Cancer Cells. *Chemistry & Biology* **2008**, *15* (3), 234-245. DOI: https://doi.org/10.1016/j.chembiol.2008.02.010.
(34) Yang, W. S.; Stockwell, B. R. Ferroptosis: Death by Lipid Peroxidation. *Trends in Cell Biology* **2016**, *26* (3), 165-176. DOI: 10.1016/j.tcb.2015.10.014 (acccessed 2023/08/11).
(35) Magtanong, L.; Mueller, G. D.; Williams, K. J.; Billmann, M.; Chan, K.; Armenta, D. A.; Pope, L. E.; Moffat, J.; Boone, C.; Myers, C. L.; et al. Context-dependent regulation of ferroptosis sensitivity. *Cell*

Chemical Biology **2022**, *29* (9), 1409-1418.e1406. DOI: 10.1016/j.chembiol.2022.06.004 (acccessed 2023/08/11).
(36) Dixon, S. J.; Pratt, D. A. Ferroptosis: A flexible constellation of related biochemical mechanisms. *Molecular Cell* **2023**, *83* (7), 1030-1042. DOI: https://doi.org/10.1016/j.molcel.2023.03.005.
(37) Kagan, V. E.; Mao, G.; Qu, F.; Angeli, J. P. F.; Doll, S.; Croix, C. S.; Dar, H. H.; Liu, B.; Tyurin, V. A.; Ritov, V. B.; et al. Oxidized arachidonic and adrenic PEs navigate cells to ferroptosis. *Nature Chemical Biology* **2017**, *13* (1), 81-90. DOI: 10.1038/nchembio.2238.
(38) Magtanong, L.; Ko, P. J.; To, M.; Cao, J. Y.; Forcina, G. C.; Tarangelo, A.; Ward, C. C.; Cho, K.; Patti, G. J.; Nomura, D. K.; et al. Exogenous Monounsaturated Fatty Acids Promote a Ferroptosis-Resistant Cell State. *Cell Chem Biol* **2019**, *26* (3), 420-432.e429. DOI: 10.1016/j.chembiol.2018.11.016 From NLM.
(39) Doll, S.; Proneth, B.; Tyurina, Y. Y.; Panzilius, E.; Kobayashi, S.; Ingold, I.; Irmler, M.; Beckers, J.; Aichler, M.; Walch, A. ACSL4 dictates ferroptosis sensitivity by shaping cellular lipid composition. *Nature chemical biology* **2017**, *13* (1), 91-98.
(40) Eaton, J. K.; Furst, L.; Ruberto, R. A.; Moosmayer, D.; Hilpmann, A.; Ryan, M. J.; Zimmermann, K.; Cai, L. L.; Niehues, M.; Badock, V.; et al. Selective covalent targeting of GPX4 using masked nitrile-oxide electrophiles. *Nat Chem Biol* **2020**, *16* (5), 497-506. DOI: 10.1038/s41589-020-0501-5 From NLM.
(41) Griffith, O. W.; Meister, A. Potent and specific inhibition of glutathione synthesis by buthionine sulfoximine (Sn-butyl homocysteine sulfoximine). *Journal of Biological Chemistry* **1979**, *254* (16), 7558-7560.
(42) Doll, S.; Freitas, F. P.; Shah, R.; Aldrovandi, M.; da Silva, M. C.; Ingold, I.; Goya Grocin, A.; Xavier da Silva, T. N.; Panzilius, E.; Scheel, C. H.; et al. FSP1 is a glutathione-independent ferroptosis suppressor. *Nature* **2019**, *575* (7784), 693-698. DOI: 10.1038/s41586-019-1707-0.
(43) Bersuker, K.; Hendricks, J. M.; Li, Z.; Magtanong, L.; Ford, B.; Tang, P. H.; Roberts, M. A.; Tong, B.; Maimone, T. J.; Zoncu, R.; et al. The CoQ oxidoreductase FSP1 acts parallel to GPX4 to inhibit ferroptosis. *Nature* **2019**, *575* (7784), 688-692. DOI: 10.1038/s41586-019-1705-2.
(44) Hendricks, J. M.; Doubravsky, C. E.; Wehri, E.; Li, Z.; Roberts, M. A.; Deol, K. K.; Lange, M.; Lasheras-Otero, I.; Momper, J. D.; Dixon, S. J. Identification of structurally diverse FSP1 inhibitors that sensitize cancer cells to ferroptosis. *Cell Chemical Biology* **2023**.
(45) Mishima, E.; Ito, J.; Wu, Z.; Nakamura, T.; Wahida, A.; Doll, S.; Tonnus, W.; Nepachalovich, P.; Eggenhofer, E.; Aldrovandi, M.; et al. A non-canonical vitamin K cycle is a potent ferroptosis suppressor. *Nature* **2022**, *608* (7924), 778-783. DOI: 10.1038/s41586-022-05022-3.
(46) Feng, H.; Stockwell, B. R. Unsolved mysteries: How does lipid peroxidation cause ferroptosis? *PLOS Biology* **2018**, *16* (5), e2006203. DOI: 10.1371/journal.pbio.2006203.
(47) Gao, M.; Yi, J.; Zhu, J.; Minikes, A. M.; Monian, P.; Thompson, C. B.; Jiang, X. Role of Mitochondria in Ferroptosis. *Mol Cell* **2019**, *73* (2), 354-363.e353. DOI: 10.1016/j.molcel.2018.10.042 From NLM.
(48) Torii, S.; Shintoku, R.; Kubota, C.; Yaegashi, M.; Torii, R.; Sasaki, M.; Suzuki, T.; Mori, M.; Yoshimoto, Y.; Takeuchi, T.; et al. An essential role for functional lysosomes in ferroptosis of cancer cells. *Biochemical Journal* **2016**, *473* (6), 769-777. DOI: 10.1042/bj20150658 (acccessed 11/30/2023).
(49) von Krusenstiern, A. N.; Robson, R. N.; Qian, N.; Qiu, B.; Hu, F.; Reznik, E.; Smith, N.; Zandkarimi, F.; Estes, V. M.; Dupont, M.; et al. Identification of essential sites of lipid peroxidation in ferroptosis. *Nature Chemical Biology* **2023**, *19* (6), 719-730. DOI: 10.1038/s41589-022-01249-3.
(50) Pedrera, L.; Espiritu, R. A.; Ros, U.; Weber, J.; Schmitt, A.; Stroh, J.; Hailfinger, S.; von Karstedt, S.; García-Sáez, A. J. Ferroptotic pores induce Ca(2+) fluxes and ESCRT-III activation to modulate cell death kinetics. *Cell Death Differ* **2021**, *28* (5), 1644-1657. DOI: 10.1038/s41418-020-00691-x From NLM.
(51) Van Kessel, A. T. M.; Karimi, R.; Cosa, G. Live-cell imaging reveals impaired detoxification of lipid-derived electrophiles is a hallmark of ferroptosis. *Chemical Science* **2022**, *13* (33), 9727-9738, 10.1039/D2SC00525E. DOI: 10.1039/D2SC00525E.

(52) Bacellar, I. O. L.; Oliveira, M. C.; Dantas, L. S.; Costa, E. B.; Junqueira, H. C.; Martins, W. K.; Durantini, A. M.; Cosa, G.; Di Mascio, P.; Wainwright, M.; et al. Photosensitized Membrane Permeabilization Requires Contact-Dependent Reactions between Photosensitizer and Lipids. *Journal of the American Chemical Society* **2018**, *140* (30), 9606-9615. DOI: 10.1021/jacs.8b05014.
(53) Berridge, M. V.; Herst, P. M.; Tan, A. S. Tetrazolium dyes as tools in cell biology: new insights into their cellular reduction. *Biotechnology annual review* **2005**, *11*, 127-152.
(54) Ahmed, S. A.; Gogal, R. M., Jr.; Walsh, J. E. A new rapid and simple non-radioactive assay to monitor and determine the proliferation of lymphocytes: an alternative to [3H]thymidine incorporation assay. *J Immunol Methods* **1994**, *170* (2), 211-224. DOI: 10.1016/0022-1759(94)90396-4 From NLM.
(55) Hannah, R.; Beck, M.; Moravec, R.; Riss, T. CellTiter-Glo™ Luminescent cell viability assay: a sensitive and rapid method for determining cell viability. *Promega Cell Notes* **2001**, *2*, 11-13.
(56) Manual, A. G. Cell Viability Assays.
(57) Chen, Y.; Liu, Y.; Lan, T.; Qin, W.; Zhu, Y.; Qin, K.; Gao, J.; Wang, H.; Hou, X.; Chen, N.; et al. Quantitative Profiling of Protein Carbonylations in Ferroptosis by an Aniline-Derived Probe. *Journal of the American Chemical Society* **2018**, *140* (13), 4712-4720. DOI: 10.1021/jacs.8b01462.
(58) Okimoto, Y.; Watanabe, A.; Niki, E.; Yamashita, T.; Noguchi, N. A novel fluorescent probe diphenyl-1-pyrenylphosphine to follow lipid peroxidation in cell membranes. *FEBS Letters* **2000**, *474* (2-3), 137-140. DOI: https://doi.org/10.1016/S0014-5793(00)01587-8.
(59) Matot, I.; Manevich, Y.; Al-Mehdi, A.-B.; Song, C.; Fisher, A. B. Fluorescence imaging of lipid peroxidation in isolated rat lungs during nonhypoxic lung ischemia. *Free Radical Biology and Medicine* **2003**, *34* (6), 785-790. DOI: https://doi.org/10.1016/S0891-5849(02)01435-1.
(60) Soh, N.; Ariyoshi, T.; Fukaminato, T.; Nakajima, H.; Nakano, K.; Imato, T. Swallow-tailed perylene derivative: a new tool for fluorescent imaging of lipid hydroperoxides. *Organic & Biomolecular Chemistry* **2007**, *5* (23), 3762-3768, 10.1039/B713223A. DOI: 10.1039/B713223A.
(61) Yamanaka, K.; Saito, Y.; Sakiyama, J.; Ohuchi, Y.; Oseto, F.; Noguchi, N. A novel fluorescent probe with high sensitivity and selective detection of lipid hydroperoxides in cells. *RSC Advances* **2012**, *2* (20), 7894-7900, 10.1039/C2RA20816D. DOI: 10.1039/C2RA20816D.
(62) Naguib, Y. M. A fluorometric method for measurement of peroxyl radical scavenging activities of lipophilic antioxidants. *Analytical biochemistry* **1998**, *265* (2), 290-298.
(63) MacDonald, M. L.; Murray, I. V. J.; Axelsen, P. H. Mass spectrometric analysis demonstrates that BODIPY 581/591 C11 overestimates and inhibits oxidative lipid damage. *Free Radical Biology and Medicine* **2007**, *42* (9), 1392-1397. DOI: https://doi.org/10.1016/j.freeradbiomed.2007.01.038.
(64) Krumova, K.; Friedland, S.; Cosa, G. How Lipid Unsaturation, Peroxyl Radical Partitioning, and Chromanol Lipophilic Tail Affect the Antioxidant Activity of α-Tocopherol: Direct Visualization via High-Throughput Fluorescence Studies Conducted with Fluorogenic α-Tocopherol Analogues. *Journal of the American Chemical Society* **2012**, *134* (24), 10102-10113. DOI: 10.1021/ja301680m.
(65) Shah, R.; Farmer, L. A.; Zilka, O.; Van Kessel, A. T. M.; Pratt, D. A. Beyond DPPH: Use of Fluorescence-Enabled Inhibited Autoxidation to Predict Oxidative Cell Death Rescue. *Cell Chem Biol* **2019**, *26* (11), 1594-1607.e1597. DOI: 10.1016/j.chembiol.2019.09.007 From NLM.
(66) Mallais, M.; Hanson, C. S.; Giray, M.; Pratt, D. A. General Approach to Identify, Assess, and Characterize Inhibitors of Lipid Peroxidation and Associated Cell Death. *ACS Chemical Biology* **2023**, *18* (3), 561-571. DOI: 10.1021/acschembio.2c00897.
(67) Oleynik, P.; Ishihara, Y.; Cosa, G. Design and Synthesis of a BODIPY-α-Tocopherol Adduct for Use as an Off/On Fluorescent Antioxidant Indicator. *Journal of the American Chemical Society* **2007**, *129* (7), 1842-1843. DOI: 10.1021/ja066789g.
(68) Khatchadourian, A.; Krumova, K.; Boridy, S.; Ngo, A. T.; Maysinger, D.; Cosa, G. Molecular Imaging of Lipid Peroxyl Radicals in Living Cells with a BODIPY−α-Tocopherol Adduct. *Biochemistry* **2009**, *48* (24), 5658-5668. DOI: 10.1021/bi900402c.

(69) Krumova, K.; Greene, L. E.; Cosa, G. Fluorogenic α-Tocopherol Analogue for Monitoring the Antioxidant Status within the Inner Mitochondrial Membrane of Live Cells. *Journal of the American Chemical Society* **2013**, *135* (45), 17135-17143. DOI: 10.1021/ja408227f.
(70) Greene, L. E.; Lincoln, R.; Cosa, G. Rate of Lipid Peroxyl Radical Production during Cellular Homeostasis Unraveled via Fluorescence Imaging. *Journal of the American Chemical Society* **2017**, *139* (44), 15801-15811. DOI: 10.1021/jacs.7b08036.
(71) Greene, L. E.; Lincoln, R.; Cosa, G. Tuning Photoinduced Electron Transfer Efficiency of Fluorogenic BODIPY-α-Tocopherol Analogues. *Photochemistry and Photobiology* **2019**, *95* (1), 192-201. DOI: https://doi.org/10.1111/php.13062.
(72) Wong, F. H.; AbuArish, A.; Matthes, E.; Turner, M. J.; Greene, L. E.; Cloutier, A.; Robert, R.; Thomas, D. Y.; Cosa, G.; Cantin, A. M.; et al. Cigarette smoke activates CFTR through ROS-stimulated cAMP signaling in human bronchial epithelial cells. *American Journal of Physiology-Cell Physiology* **2018**, *314* (1), C118-C134. DOI: 10.1152/ajpcell.00099.2017.
(73) Foret, M. K.; Do Carmo, S.; Lincoln, R.; Greene, L. E.; Zhang, W.; Cuello, A. C.; Cosa, G. Effect of antioxidant supplements on lipid peroxidation levels in primary cortical neuron cultures. *Free Radical Biology and Medicine* **2019**, *130*, 471-477. DOI: https://doi.org/10.1016/j.freeradbiomed.2018.11.019.
(74) Naguib, M.; Feldman, N.; Zarodkiewicz, P.; Shropshire, H.; Biamis, C.; El-Halfawy, O. M.; McCain, J.; Dezanet, C.; Décout, J.-L.; Chen, Y.; et al. An evolutionary conserved detoxification system for membrane lipid–derived peroxyl radicals in Gram-negative bacteria. *PLOS Biology* **2022**, *20* (5), e3001610. DOI: 10.1371/journal.pbio.3001610.
(75) Sakaya, A.; Durantini, A. M.; Gidi, Y.; Šverko, T.; Wieczny, V.; McCain, J.; Cosa, G. Fluorescence-Amplified Detection of Redox Turnovers in Supported Lipid Bilayers Illuminates Redox Processes of α-Tocopherol. *ACS Applied Materials & Interfaces* **2022**, *14* (11), 13872-13882. DOI: 10.1021/acsami.1c23931.
(76) Sakaya, A.; Bacellar, I. O. L.; Fonseca, J. L.; Durantini, A. M.; McCain, J.; Xu, L.; Vignoni, M.; Thomas, A. H.; Baptista, M. S.; Cosa, G. Singlet Oxygen Flux, Associated Lipid Photooxidation, and Membrane Expansion Dynamics Visualized on Giant Unilamellar Vesicles. *Langmuir* **2023**, *39* (1), 442-452. DOI: 10.1021/acs.langmuir.2c02720.
(77) Cole, F. J. Alle de brieven van Antoni van Leeuwenhoek. *Nature* **1939**, *144* (3658), 956-958. DOI: 10.1038/144956a0.
(78) Hyllner, J.; Mason, C.; Wilmut, I. Cells: from Robert Hooke to cell therapy--a 350 year journey. *Philos Trans R Soc Lond B Biol Sci* **2015**, *370* (1680), 20150320. DOI: 10.1098/rstb.2015.0320 From NLM.
(79) Rust, M. J.; Bates, M.; Zhuang, X. Sub-diffraction-limit imaging by stochastic optical reconstruction microscopy (STORM). *Nature methods* **2006**, *3* (10), 793-796.
(80) Betzig, E.; Patterson, G. H.; Sougrat, R.; Lindwasser, O. W.; Olenych, S.; Bonifacino, J. S.; Davidson, M. W.; Lippincott-Schwartz, J.; Hess, H. F. Imaging intracellular fluorescent proteins at nanometer resolution. *science* **2006**, *313* (5793), 1642-1645.
(81) Klar, T. A.; Jakobs, S.; Dyba, M.; Egner, A.; Hell, S. W. Fluorescence microscopy with diffraction resolution barrier broken by stimulated emission. *Proceedings of the National Academy of Sciences* **2000**, *97* (15), 8206-8210. DOI: doi:10.1073/pnas.97.15.8206.
(82) Balzarotti, F.; Eilers, Y.; Gwosch, K. C.; Gynnå, A. H.; Westphal, V.; Stefani, F. D.; Elf, J.; Hell, S. W. Nanometer resolution imaging and tracking of fluorescent molecules with minimal photon fluxes. *Science* **2017**, *355* (6325), 606-612. DOI: doi:10.1126/science.aak9913.
(83) Acuña, A. U.; Amat-Guerri, F.; Morcillo, P.; Liras, M.; Rodríguez, B. Structure and Formation of the Fluorescent Compound of Lignum nephriticum. *Organic letters* **2009**, *11* (14), 3020-3023.
(84) Stokes, G. G. XXX. On the change of refrangibility of light. *Philosophical transactions of the Royal Society of London* **1852**, (142), 463-562.

(85) Lavis, L. D.; Raines, R. T. Bright Ideas for Chemical Biology. *ACS Chemical Biology* **2008**, *3* (3), 142-155. DOI: 10.1021/cb700248m.
(86) JOSEPH, R. LAKOWICZ:" Principles of Fluorescence Spectroscopy", 1999. KLUWER ACADEMIC/PLENUM PUBLISHERS.
(87) Turro, N. J.; Ramamurthy, V.; Scaiano, J. C. *Modern molecular photochemistry of organic molecules*; University Science Books Sausalito, CA, 2010.
(88) Grimm, J. B.; Lavis, L. D. Caveat fluorophore: an insiders' guide to small-molecule fluorescent labels. *Nature Methods* **2022**, *19* (2), 149-158. DOI: 10.1038/s41592-021-01338-6.
(89) Jameson, D. M.; Ross, J. A. Fluorescence polarization/anisotropy in diagnostics and imaging. *Chemical reviews* **2010**, *110* (5), 2685-2708.
(90) Becker, W. Fluorescence lifetime imaging–techniques and applications. *Journal of microscopy* **2012**, *247* (2), 119-136.
(91) Rajendran, M.; Yapici, E.; Miller, L. W. Lanthanide-Based Imaging of Protein–Protein Interactions in Live Cells. *Inorganic Chemistry* **2014**, *53* (4), 1839-1853. DOI: 10.1021/ic4018739.
(92) Gidwani, B.; Sahu, V.; Shukla, S. S.; Pandey, R.; Joshi, V.; Jain, V. K.; Vyas, A. Quantum dots: Prospectives, toxicity, advances and applications. *Journal of Drug Delivery Science and Technology* **2021**, *61*, 102308. Gil, H. M.; Price, T. W.; Chelani, K.; Bouillard, J.-S. G.; Calaminus, S. D.; Stasiuk, G. J. NIR-quantum dots in biomedical imaging and their future. *Iscience* **2021**, *24* (3).
(93) Shimomura, O.; Johnson, F. H.; Saiga, Y. Extraction, purification and properties of aequorin, a bioluminescent protein from the luminous hydromedusan, Aequorea. *Journal of cellular and comparative physiology* **1962**, *59* (3), 223-239.
(94) Prasher, D. C.; Eckenrode, V. K.; Ward, W. W.; Prendergast, F. G.; Cormier, M. J. Primary structure of the Aequorea victoria green-fluorescent protein. *Gene* **1992**, *111* (2), 229-233.
(95) Chalfie, M.; Tu, Y.; Euskirchen, G.; Ward, W. W.; Prasher, D. C. Green fluorescent protein as a marker for gene expression. *Science* **1994**, *263* (5148), 802-805.
(96) Shaner, N. C.; Campbell, R. E.; Steinbach, P. A.; Giepmans, B. N.; Palmer, A. E.; Tsien, R. Y. Improved monomeric red, orange and yellow fluorescent proteins derived from Discosoma sp. red fluorescent protein. *Nature biotechnology* **2004**, *22* (12), 1567-1572. Shaner, N. C.; Steinbach, P. A.; Tsien, R. Y. A guide to choosing fluorescent proteins. *Nature methods* **2005**, *2* (12), 905-909.
(97) Lincoln, R.; Greene, L. E.; Zhang, W.; Louisia, S.; Cosa, G. Mitochondria Alkylation and Cellular Trafficking Mapped with a Lipophilic BODIPY–Acrolein Fluorogenic Probe. *Journal of the American Chemical Society* **2017**, *139* (45), 16273-16281. DOI: 10.1021/jacs.7b08615.
(98) Ablenas, C. J.; Gidi, Y.; Powdrill, M. H.; Ahmed, N.; Shaw, T. A.; Mesko, M.; Götte, M.; Cosa, G.; Pezacki, J. P. Hepatitis C Virus Helicase Binding Activity Monitored through Site-Specific Labeling Using an Expanded Genetic Code. *ACS Infectious Diseases* **2019**, *5* (12), 2118-2126. DOI: 10.1021/acsinfecdis.9b00220. Gidi, Y.; Robert, A.; Tordo, A.; Lovell, T. C.; Ramos-Sanchez, J.; Sakaya, A.; Götte, M.; Cosa, G. Binding and Sliding Dynamics of the Hepatitis C Virus Polymerase: Hunting the 3′ Terminus. *ACS Infectious Diseases* **2023**. DOI: 10.1021/acsinfecdis.3c00048.
(99) Platnich, C. M.; Hariri, A. A.; Rahbani, J. F.; Gordon, J. B.; Sleiman, H. F.; Cosa, G. Kinetics of Strand Displacement and Hybridization on Wireframe DNA Nanostructures: Dissecting the Roles of Size, Morphology, and Rigidity. *ACS Nano* **2018**, *12* (12), 12836-12846. DOI: 10.1021/acsnano.8b08016.
(100) Glembockyte, V.; Wieneke, R.; Gatterdam, K.; Gidi, Y.; Tampé, R.; Cosa, G. Tris-N-Nitrilotriacetic Acid Fluorophore as a Self-Healing Dye for Single-Molecule Fluorescence Imaging. *Journal of the American Chemical Society* **2018**, *140* (35), 11006-11012. DOI: 10.1021/jacs.8b04681.
(101) Betzig, E.; Chichester, R. J. Single Molecules Observed by Near-Field Scanning Optical Microscopy. *Science* **1993**, *262* (5138), 1422-1425. DOI: doi:10.1126/science.262.5138.1422.
(102) Axelrod, D.; Burghardt, T. P.; Thompson, N. L. Total internal reflection fluorescence. *Annual review of biophysics and bioengineering* **1984**, *13* (1), 247-268.

(103) Funatsu, T.; Harada, Y.; Tokunaga, M.; Saito, K.; Yanagida, T. Imaging of single fluorescent molecules and individual ATP turnovers by single myosin molecules in aqueous solution. *Nature* **1995**, *374* (6522), 555-559.
(104) Paige, M.; Bjerneld, E.; Moerner, W. A Comparison of Through‐the‐Objective Total Internal Reflection Microscopy and Epifluorescence Microscopy for Single‐Molecule Fluorescence Imaging. *Single Molecules* **2001**, *2* (3), 191-201.
(105) Tokunaga, M.; Imamoto, N.; Sakata-Sogawa, K. Highly inclined thin illumination enables clear single-molecule imaging in cells. *Nature Methods* **2008**, *5* (2), 159-161. DOI: 10.1038/nmeth1171.
(106) Allen, J. R. *Light Sheet Fluorescence Microscopy*. Nikon Microscopy U, 2023. https://www.microscopyu.com/techniques/light-sheet/light-sheet-fluorescence-microscopy (accessed 2023.
(107) Minsky, M. Memoir on inventing the confocal scanning microscope. *Scanning* **1988**, *10* (4), 128-138. White, J.; Amos, W.; Fordham, M. An evaluation of confocal versus conventional imaging of biological structures by fluorescence light microscopy. *The Journal of cell biology* **1987**, *105* (1), 41-48.
(108) Gräf, R.; Rietdorf, J.; Zimmermann, T. Live cell spinning disk microscopy. *Microscopy Techniques: -/-* **2005**, 57-75.
(109) Jonkman, J.; Brown, C. M.; Wright, G. D.; Anderson, K. I.; North, A. J. Tutorial: guidance for quantitative confocal microscopy. *Nature Protocols* **2020**, *15* (5), 1585-1611. DOI: 10.1038/s41596-020-0313-9.
(110) Abbe, E. Beiträge zur Theorie des Mikroskops und der mikroskopischen Wahrnehmung. *Archiv für Mikroskopische Anatomie* **1873**, *9* (1), 413-468. DOI: 10.1007/BF02956173.
(111) Hell, S. W. Nobel Lecture: Nanoscopy with freely propagating light. *Reviews of Modern Physics* **2015**, *87* (4), 1169. Betzig, E. Single molecules, cells, and super‐resolution optics (Nobel lecture). *Angewandte Chemie International Edition* **2015**, *54* (28), 8034-8053. Moerner, W. E. Single‐molecule spectroscopy, imaging, and photocontrol: foundations for super‐resolution microscopy (nobel lecture). *Angewandte Chemie International Edition* **2015**, *54* (28), 8067-8093.
(112) Hell, S. W.; Wichmann, J. Breaking the diffraction resolution limit by stimulated emission: stimulated-emission-depletion fluorescence microscopy. *Opt. Lett.* **1994**, *19* (11), 780-782. DOI: 10.1364/OL.19.000780.
(113) Wegel, E.; Göhler, A.; Lagerholm, B. C.; Wainman, A.; Uphoff, S.; Kaufmann, R.; Dobbie, I. M. Imaging cellular structures in super-resolution with SIM, STED and Localisation Microscopy: A practical comparison. *Scientific Reports* **2016**, *6* (1), 27290. DOI: 10.1038/srep27290.
(114) Xu, K.; Zhong, G.; Zhuang, X. Actin, Spectrin, and Associated Proteins Form a Periodic Cytoskeletal Structure in Axons. *Science* **2013**, *339* (6118), 452-456. DOI: doi:10.1126/science.1232251.
(115) Stephan, T.; Roesch, A.; Riedel, D.; Jakobs, S. Live-cell STED nanoscopy of mitochondrial cristae. *Scientific Reports* **2019**, *9* (1), 12419. DOI: 10.1038/s41598-019-48838-2.
(116) Deguchi, T.; Iwanski, M. K.; Schentarra, E.-M.; Heidebrecht, C.; Schmidt, L.; Heck, J.; Weihs, T.; Schnorrenberg, S.; Hoess, P.; Liu, S.; et al. Direct observation of motor protein stepping in living cells using MINFLUX. *Science* **2023**, *379* (6636), 1010-1015. DOI: doi:10.1126/science.ade2676.
(117) Liu, S.; Hoess, P.; Ries, J. Super-Resolution Microscopy for Structural Cell Biology. *Annual Review of Biophysics* **2022**, *51* (1), 301-326. DOI: 10.1146/annurev-biophys-102521-112912.
(118) Waldchen, S.; Lehmann, J.; Klein, T.; van de Linde, S.; Sauer, M. Light-induced cell damage in live-cell super-resolution microscopy. Sci Rep. 5, 15348. 2015.
(119) Gustafsson, M. G. L. Surpassing the lateral resolution limit by a factor of two using structured illumination microscopy. *Journal of Microscopy* **2000**, *198* (2), 82-87. DOI: https://doi.org/10.1046/j.1365-2818.2000.00710.x.

(120) Dertinger, T.; Colyer, R.; Iyer, G.; Weiss, S.; Enderlein, J. Fast, background-free, 3D super-resolution optical fluctuation imaging (SOFI). *Proceedings of the National Academy of Sciences* **2009**, *106* (52), 22287-22292. DOI: doi:10.1073/pnas.0907866106.
(121) Gustafsson, N.; Culley, S.; Ashdown, G.; Owen, D. M.; Pereira, P. M.; Henriques, R. Fast live-cell conventional fluorophore nanoscopy with ImageJ through super-resolution radial fluctuations. *Nature Communications* **2016**, *7* (1), 12471. DOI: 10.1038/ncomms12471.
(122) Culley, S.; Tosheva, K. L.; Matos Pereira, P.; Henriques, R. SRRF: Universal live-cell super-resolution microscopy. *The International Journal of Biochemistry & Cell Biology* **2018**, *101*, 74-79. DOI: https://doi.org/10.1016/j.biocel.2018.05.014.
(123) Hönigsmann, H. History of phototherapy in dermatology. *Photochemical & Photobiological Sciences* **2013**, *12* (1), 16-21. DOI: 10.1039/c2pp25120e.
(124) Gøtzsche, P. C. Niels Finsen's treatment for lupus vulgaris. *J R Soc Med* **2011**, *104* (1), 41-42. DOI: 10.1258/jrsm.2010.10k066 From NLM.
(125) Grzybowski, A.; Pietrzak, K. From patient to discoverer—Niels Ryberg Finsen (1860–1904)—the founder of phototherapy in dermatology. *Clinics in Dermatology* **2012**, *30* (4), 451-455. DOI: https://doi.org/10.1016/j.clindermatol.2011.11.019.
(126) McGlynn, S.; Daigre, J.; Smith, F. External Heavy‐Atom Spin—Orbital Coupling Effect. IV. Intersystem Crossing. *The Journal of Chemical Physics* **1963**, *39* (3), 675-679.
(127) Pham, T. C.; Nguyen, V.-N.; Choi, Y.; Lee, S.; Yoon, J. Recent Strategies to Develop Innovative Photosensitizers for Enhanced Photodynamic Therapy. *Chemical Reviews* **2021**, *121* (21), 13454-13619. DOI: 10.1021/acs.chemrev.1c00381.
(128) Dąbrowski, J. M.; Arnaut, L. G. Photodynamic therapy (PDT) of cancer: from local to systemic treatment. *Photochemical & Photobiological Sciences* **2015**, *14* (10), 1765-1780. Dolmans, D. E.; Fukumura, D.; Jain, R. K. Photodynamic therapy for cancer. *Nature reviews cancer* **2003**, *3* (5), 380-387.
(129) Durantini, A. M.; Heredia, D. A.; Durantini, J. E.; Durantini, E. N. BODIPYs to the rescue: Potential applications in photodynamic inactivation. *European Journal of Medicinal Chemistry* **2018**, *144*, 651-661. DOI: https://doi.org/10.1016/j.ejmech.2017.12.068.
(130) Durantini, A. M.; Greene, L. E.; Lincoln, R.; Martínez, S. R.; Cosa, G. Reactive Oxygen Species Mediated Activation of a Dormant Singlet Oxygen Photosensitizer: From Autocatalytic Singlet Oxygen Amplification to Chemicontrolled Photodynamic Therapy. *Journal of the American Chemical Society* **2016**, *138* (4), 1215-1225. DOI: 10.1021/jacs.5b10288.

Chapter 2: Live Cell Monitoring of Ferroptosis Onset and Progression via a Palette of Tocopherol-based Fluorogenic Probes

Wenzhou Zhang*, Laiyi Xu*, Julia McCain, Terri Lovell, Gonzalo Cosa, *to be submitted.*

2.1 Preface:

As highlighted in **Chapter 1 (Section 1.3.4**), fundamental questions remain unanswered in the fast-growing field of ferroptosis, specifically as to the spatiotemporal origins of lipid peroxidation and the execution of cell death. We champion cell imaging combined with intelligent probe design as the route toward resolving these questions. Here, we deploy a palette of newly designed and prepared fluorogenic probes for lipid peroxidation toward conducting both long timecourse and high-resolution imaging applications. My work seeks to monitor and examine – for the first time – ferroptosis from induction to execution. Via multichannel imaging, we unravel the timing of peroxidation, cell deformation, and membrane permeabilization. We assess the individual contributions of the endoplasmic reticulum (ER), mitochondria, lysosome, and plasma membrane with regards to lipid peroxidation and antioxidant capacity and find the ER to be the key site of lipid peroxidation. In addition, this work uncovers valuable insights, in observing the trafficking of damaged lipids from the interior of the cell towards the plasma membrane.

This chapter is to be submitted as a manuscript and is co-authored with Laiyi Xu as equal contributors. Probe synthesis and characterization was the work of Laiyi Xu, and as such will not be discussed in this thesis.

2.2 Abstract:

Ferroptosis is a regulated form of cell death driven by uncontrollable lipid peroxidation. Distinct from other regulated forms of cell death, ferroptosis is governed by many overlapping regulators, all converging on the formation of lipid peroxyl radicals, accumulation of lipid hydroperoxides, and plasma membrane damage. Various pathways leading to the overproduction of lipid hydroperoxides have been elucidated in recent years, along with small molecule modulators of these pathways to up- or down-regulate ferroptosis in the search of therapeutic applications. While lipid peroxidation has been observed through endpoint imaging measurements, dynamic information is lacking, such as the spatiotemporal development of lipid peroxidation as it relates to cell death and the intracellular contributions of various organelles. In this work, we demonstrate that a palette of newly developed organelle-targeting, fluorogenic α-tocopherol analogues can be employed to (evaluate organelle contributions to ferroptosis rescue and to) observe the direct induction of ferroptosis in real time. Further, we show a proof-of-concept assay in which our probe can be used as an internal standard in assessing ferroptosis rescue. Finally, via high-resolution microscopy and colocalization studies, we demonstrate that the plasma membrane is a site of accumulation of damaged lipids from the interior of the cell in ferroptosis. Taken together, our results validate the potential of live cell monitoring of ferroptosis from start to finish. We illuminate fundamental aspects of ferroptotic cell death, in that plasma membrane damage comes after the total consumption of antioxidants in the cell, along with the source of the membrane damage – trafficked lipid peroxidation products from the interior of the cell. We champion our palette of lipid peroxidation probes as being suitable for the study of numerous aspects of ferroptosis field, and as a valuable toolbox for the community.

2.3 Introduction:

Ferroptosis is an iron-dependent, regulated form of cell death resulting from accumulation of lipid hydroperoxides.[1] Normally detoxified via enzymatic defenses[2] such as the selenocysteine-dependent enzyme glutathione peroxidase (GPX4), the direct inhibition of GPX4 results in lipid hydroperoxide accumulation, whose downstream pathways and byproducts lead to cell death.[1] Ferroptotic cell death can be rescued by either the addition of lipophilic, radical trapping antioxidants, or the chelation of labile iron – preventing Fenton chemistry and further radical formation.[3] From a therapeutic standpoint, ferroptosis serves a unique entry point into many applications. Various cancer lineages have shown increased metabolic vulnerability to ferroptotic cell death, providing opportunities to target these cells and control their proliferation.[4] In addition, lipid peroxidation plays a role in the pathology of many degenerative diseases such as neurodegeneration and ischaemia reperfusion.[5-7] Here ferroptosis inhibition may ameliorate and prevent symptoms.

At the molecular level, lipid hydroperoxides are generated via auto-oxidation of lipid membranes, a process which proceeds in a free radical chain reaction initiated by a suitable reactive oxygen species (ROS).[8] Since ROS are highly reactive, short-lived, and promiscuous in their oxidative targets, the specific site and rate of their generation, as well as the intracellular contributions to ferroptosis are a source of great interest toward deciphering the molecular and cellular interconnections in ferroptosis. While plasma membrane (PM) oxidation and damage has been widely observed and recognized as a hallmark of ferroptosis[9], other sources of lipid-associated ROS, including the endoplasmic reticulum (ER)[10], mitochondria,[11] and lysosome,[8, 10] as well as lipid droplets, which regulate PUFA trafficking have also garnered significant attention. The relevance and roles of these subcellular membranes to ferroptosis have gradually been elucidated over the past decade. Stockwell *et al.* have recently demonstrated that oxidative damage in the ER renders the cell most susceptible to ferroptosis, compared to mitochondria and lysosomes.[12] Mitochondria have been shown to be crucial in ferroptosis induced by inhibition of

system x_c^-, although they are dispensable in ferroptosis induced by GPX4.[13] Constitutive generation of ROS in lysosomes have been reported by Torii *et al*, who proposed the essential role of lysosomal activity in regulating cellular iron equilibria and ROS generation.[14] It has been established that boosting lipid droplet formation renders the cell less sensitive to ferroptosis, while degradation of lipid droplets facilitates ferroptosis.[15] Related, the mechanism of action of various ferroptosis inhibitors in these organelles have also been investigated. To this end, it has been shown that monounsaturated fatty acids (MUFAs) potently inhibit ferroptosis by suppression of ROS accumulation at PM.[16] The ER have been identified as a major site of PUFA incorporation beyond lipid droplets,[12] while accumulation of Fer-1, an antioxidant/ferroptosis suppressor, in mitochondria and lysosomes did not contribute to suppression of ferroptosis induced by erastin.[10] However, the effectiveness of protecting these subcellular membranes from lipid peroxidation has yet to be systematically compared. In addition, although lipid peroxidation, unique cell morphology alternations, including rounding up and formation of blisters, and PM permeabilization have all been commonly observed,[16] it remains unclear how these events correlate with each other in the timeline of ferroptosis. Finally, how lipid peroxidation in these subcellular membranes is correlated in time has not been fully understand. It is currently believed that lipid peroxides initially accumulate in ER and other intercellular membranes, with preferential PM accumulation observed in late stage of ferroptosis.[17] However, it is unknown whether lipid peroxidation spreads from intracellular membranes to PM or whether accumulation of lipid hydroperoxides in these sites happens independent to each other with a temporal delay—when exactly does lipid peroxidation initiate in these subcellular membranes and how it propagates remains to be elucidated.[12, 17, 18]

The lack of temporal resolution posts challenges in understanding the dynamic and heterogenous picture in cellular ferroptosis. In the field of ferroptosis research, endpoint measurements are standard. It is common to assess cell viability[3] via product accumulation assays (i.e. Cell Titer Glo, AlamarBlue), assess lipid peroxidation via fixation-and-staining fluorescence microscopy[12, 16, 19] (i.e. C11 BODIPY), and

metabolic changes via mass spectrometry.[20] While all these methods offer static images of process endpoints, to gain both temporal and spatial information on the onset and progression of ferroptosis, live cell fluorescence imaging becomes a highly desirable method. However, to our knowledge, real-time monitoring of ferroptosis via fluorescence microscopy has yet to be achieved due to the lack of compatible fluorescent probes.

We have previously developed a fluorogenic radical trapping antioxidant, H_4B-PMHC,[21] by linking PMHC – the active moiety of α-tocopherol – with the bright fluorophore BODIPY (**Fig. 2.1a**). In this off-on probe, oxidation of the chromanol warhead by lipid peroxyl radicals abolishes photoinduced electron transfer (PeT) and restores emission, providing a visual indicator of the spatiotemporal progression of lipid autoxidation.

Utilizing the trap-fluorophore scaffold of H_4B-PMHC, in this work we have developed a palette of fluorogenic probes targeting the mitochondria, lysosomes, and plasma membrane, respectively (**Fig 2.1b**). Addition of a targeting moiety further ensures selective partitioning in desired membrane organelles, providing a visual indication of the spatial temporal progression of lipid auto-oxidation. Here, we report the real-time, live-cell monitoring of ferroptosis via fluorescence microscopy, examining the onset and progression of ferroptosis with unprecedented spatial and temporal resolution. We explore ferroptotic cell death induced by RSL3. As a class II ferroptosis inducer, RSL3 directly inhibits GPX4,[3] causing accumulation of lipid hydroperoxides throughout the cell, as opposed to a specific organelle. We found via cell viability assay and widefield fluorescence microscopy studies that our PMHC probes exhibit different potencies toward ferroptosis inhibition, identifying the ER and PM as the most and least effective site for antioxidant intervention, respectively. Using multi-channel imaging experiments, we show that lipid peroxidation and total antioxidant depletion occurs first, followed by cell volume change/swelling, and finally loss of membrane integrity, elucidating a timeline of ferroptosis in cell culture bulk population. Moreover, we quantified real-time fluorescence enhancement of our PMHC probes in cells treated with

RSL3 and found that lipid peroxidation initiates at similar stages with similar rates in lipid droplets/ER, mitochondria, lysosomes, and PM, although previous studies show that lipid peroxidation propagate at different rates at these sites.[12] High resolution imaging (SRRF[22]) employing our PMHC probes enabled ferroptosis to be examined at single cell level. Here lipid peroxidation in lipid droplets and ER is observed concomitantly to be the earliest sites of lipid peroxidation, further emphasising the relevance of these targets for oxidative damage. We identified the unidirectional trafficking of oxidized lipids from intracellular membranes to PM, which happens in addition to local PM peroxidation, contributing to eventual lethal accumulation of lipid hydroperoxides in PM. Together, our findings not only serve to demonstrate the utility of high spatiotemporal tools in ferroptosis research, but also contribute to original observations not accessible through other methods.

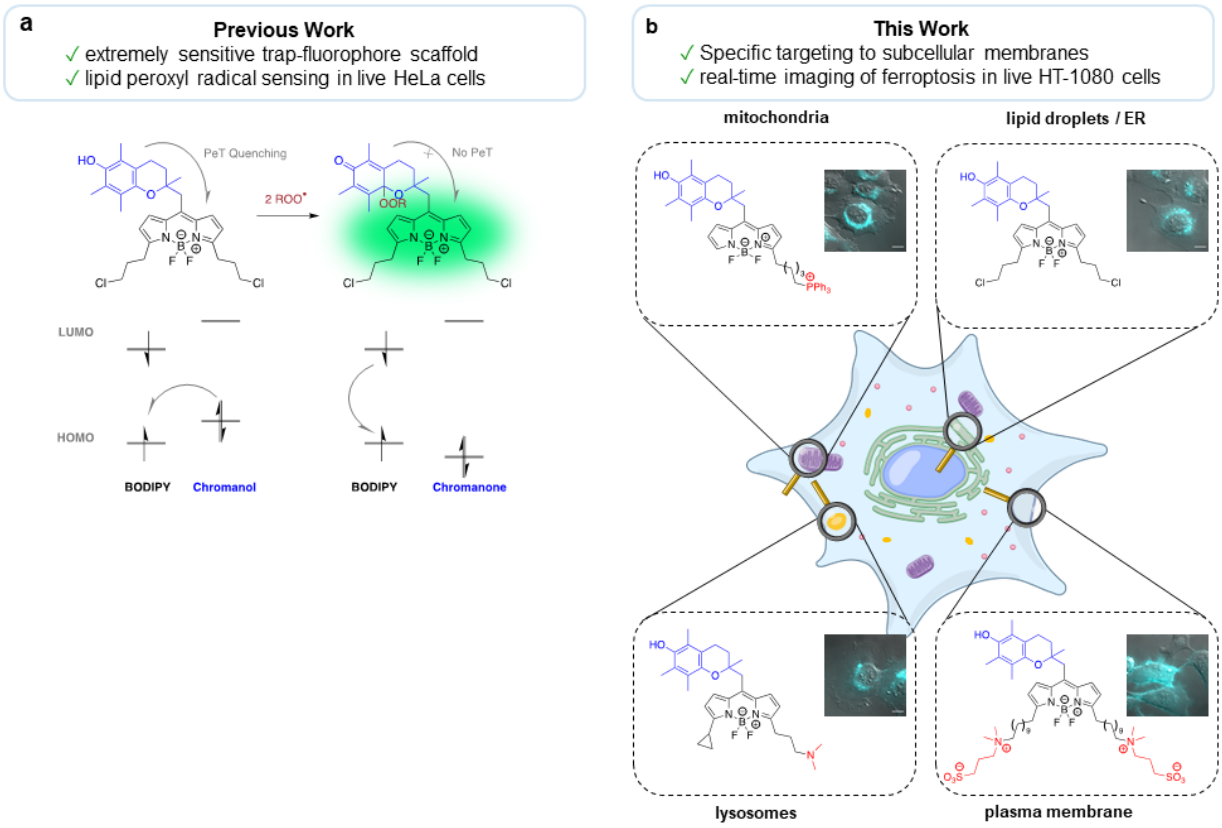

Figure 2.1: a) Mechanism of H4B-PMHC utilizing PeT. b) Structures of new palette of PMHC probes

2.4 Results and discussion:

2.4.1 H_4B-PMHC can be specifically targeted to the mitochondria, lysosomes, and plasma membrane

The contribution of various organelles in ferroptosis is of fundamental importance and the subject of studies. We found that our original probe H_4B-PMHC, which bears two propyl-chloride handles, is promiscuous in all lipid membranes due its high lipophilicity (log P = 5.85). To tackle the challenge of monitoring lipid peroxidation in specific intracellular sites during ferroptosis, in this work we have functionalized H_4B-PMHC with targeting groups to direct the probe to the mitochondria (mito-H_5B-PMHC, triphenylphosphonium cation), lysosomes (lyso-H_4B-PMHC, tertiary amine), and plasma membrane (PM-H_4B-PMHC, long zwitterionic alkyl linker). The scaffold of H_4B-PMHC is preserved in our new palette of probes for its optimized sensitivity. The design and synthesis of this palette of linkers were prepared by Laiyi Xu and thus not discussed in this work. The probe structures are shown in **Figure 2.1b** and photophysical properties characterized and summarized in **Table S2.1**.

2.4.2 Our PMHC probes show different effectiveness in ferroptosis inhibition

Considering that all our probes bear a PMHC moiety, they are organelle-specific antioxidants capable of rescuing cells from ferroptosis. A resazurin reduction assay was employed to compare their potency in inhibiting ferroptosis. Here HT-1080 cells were co-treated with the ferroptosis inducer RSL3 and a PMHC probe (or the parent antioxidant PMHC). After a 3-hour incubation, media containing RSL3 and the probe were removed and cell viability was assessed by developing with resazurin for another 3 hours, before measuring on a plate reader instrument.

As shown in **Fig 2.2a**, consistent with their antioxidant nature, all our probes exhibit a degree of ferroptosis inhibition, as shown by the marked higher viability with increasing concentrations of RSL3 compared to the negative control. Difference in efficacy at the higher RSL3 concentrations were however noticeable, demonstrating a difference in the degree of protection from ferroptosis based on where the

probe partitioned. H_4B-PMHC, which mainly accumulates in the ER and lipid droplets, showed the highest potency in inhibiting ferroptosis. It is noteworthy that, at the same concentration, H_4B-PMHC showed a superior potency compared to that of the parent antioxidant PMHC. Considering that the fluorophore BODIPY itself is a highly lipophilic molecule, we reason that the increased lipophilicity of H_4B-PMHC relative to PMHC promoted lipid membrane embedding, thus rendering the molecule more effective in ferroptosis inhibition. Surprisingly, lyso-H_4B-PMHC exhibited greater potency than mito-H_5B-PMHC, despite the central role of mitochondria in oxidative metabolism.[13] Cells treated with PM-H_4B-PMHC showed the lowest viability, suggesting that PM is the least effective site of antioxidant delivery for ferroptosis inhibition.

We note that although the same probe concentration was used for treatment (i.e. 100 nM), the effective probe concentration inside the cell is not necessary the same between different PMHC probes, as structural differences may result in different partitioning behaviors. To rule out this possibility, we measured logP values of H_4B-PMHC, mito-H_5B-PMHC, lyso-H_4B-PMHC, and PM-H_4B-PMHC via HPLC, and found that all these compounds exhibit similar lipophilicities (**Fig. 2.2b**). This suggests that here the effective probe concentration, and therefore antioxidant concentration, is approximately the same in each of these subcellular membranes. In other words, the difference in potency observed is indeed due to a matter of relevance and roles of these membranes in ferroptosis, rather than an artifact of probe partitioning.

To visualize the impact of our PMHC probes on ferroptosis progression, HT-1080 cells treated with 100 nM of a PMHC probe and RSL3 were imaged using widefield fluorescence microscopy for 3 hours. As the PMHC warhead of our probes is simultaneously an antioxidant preventing ferroptosis, along with the trigger for fluorogenicity to observe lipid peroxidation, in imaging experiments a matter of probe concentration must be considered, such that antioxidant function does not overwhelm radical detection. With H_4B-PMHC, mito-H_5B-PMHC, and lyso-H_4B-PMHC, we observed no fluorescence enhancement or

change in cell morphology (**Fig. 2.2c**), indicating that under these high loadings of RTA, ferroptosis is inhibited by the antioxidant effect of the PMHC warhead. In contrast, cells treated with PM-H_4B-PMHC underwent ferroptosis in the 3-hour time window (**Figure 2.2c,** top right panel), evidenced by fluorescence enhancement accompanied by cell rounding. Reducing the RTA probe loading to 10 nM for H_4B-PMHC, mito-H_5B-PMHC, and lyso-H_4B-PMHC, we observed a clear induction of fluorescence enhancement and characteristic morphology change (**Figure 2.2c**, bottom left panel). This corroborates the cell viability results in **Figure 2.2a**, showing per unit of antioxidant, delivery to the interior membranes is much more efficacious than to the plasma membrane. Together, these results position our palette of PMHC probes as organelle-targeted radical trapping antioxidants, enabling us to position a given amount of antioxidant in a specific subcellular membrane and assess the effect in cell viability under ferroptosis.

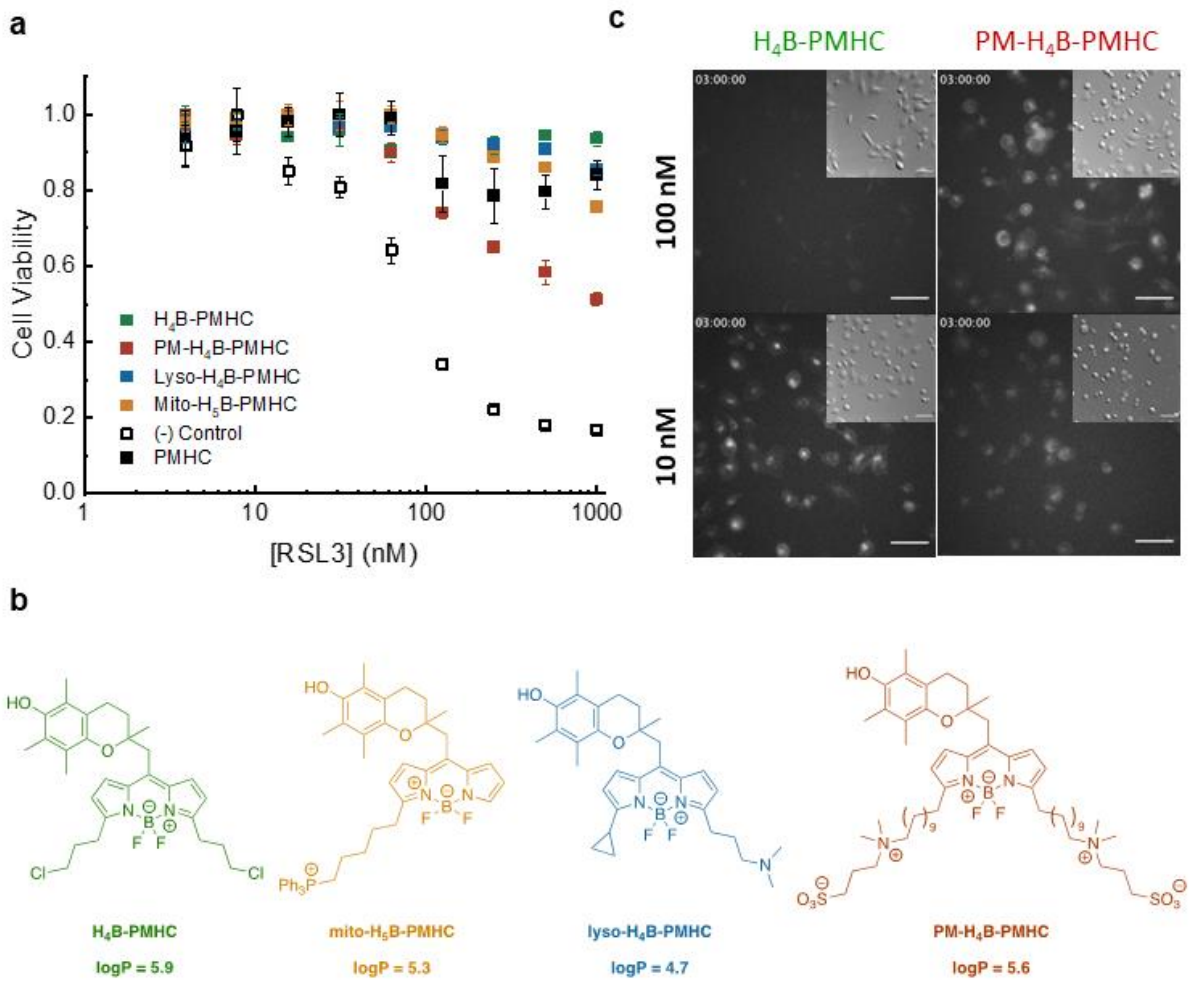

Figure 2.2: Our PMHC probes exhibit different potency for ferroptosis inhibition. a) cell viability assessed via resazurin reduction assay (normalized resazurin intensity) of HT-1080 cells treated with 100 nM H_4B-PMHC (blue), PMHC (violet), mito-H_5B-PMHC (green), lyso-H_4B-PMHC (blue), PM-H_4B-PMHC (red), or no treatment (white) and 0-1000 nM RSL (3hr treatment). Bars = SEM. b) logP values of our PMHC probes determined via the HPLC method. C) representative images of HT-1080 cells treated with H_4B-PMHC (100 nM) or PM-H_4B-PMHC (100 nM) (top) and H_4B-PMHC (10 nM) or PM-H_4B-PMHC (10 nM) (bottom) at 180 min upon RSL3 (1 uM) treatment. 20x Widefield. Scale bar 64 µm

2.4.3 Lipid peroxidation happens at a similar stage and rate in all organelles of interest

To monitor rates of lipid peroxyl radical formation in bulk population, HT-1080 cells were stained with H_4B-PMHC (10 nM) and propidium iodide (PI, 1 µM) and treated with RSL3 (1 µM). They were then imaged using widefield fluorescence microscopy with a 20x objective. Fluorescence enhancement in the

fluorogenic RTA probe channel, marking formation of lipid peroxyl radicals, was quantified via calculating the corrected total cell fluorescence (CTCF). In addition, we obtained statistics on cell death by counting the times at which cells reach the rounded morphology, the characteristic morphological change in ferroptotic cell death previously reported by Dixon *et al*. Finally, to mark the point of membrane permeabilization, the membrane impermeant dye propidium iodide (PI) was used. PI fluorescence intensity enhances upon intercalating DNA, serving as a marker the loss of plasma membrane integrity. The combination of fluorescence and brightfield microscopy yielded a holistic picture of the onset of radical formation, its generation rate, and ultimately cell death.

As shown in **Figure 2.3a-c**, the CTCF of cells treated with RSL3 and stained with H_4B-PMHC exhibited a ~20 minutes incubation period, followed by a rapid rise in intensity to reach a steady regime where intensity increased linearly with time, a manifestation of zeroth order kinetics for RTA probe oxidation, and from where we could abstract rates of antioxidant consumption. Fluorescence intensity of H_4B-PMHC peaked at approximately 100 minutes, following which cell morphology started to change. PI fluorescence started enhancing at ~120 minutes. From this, it is seen that ferroptosis occurs via an ordered mechanism, with the bulk of ROS production happening before morphology change and correlated with membrane compromise. In the absence of ferroptosis inducer RSL3, HT-1080 cells exhibit minimal lipid peroxidation and cell death, in the five-hour observation window chosen (**Fig. S2.3**).

To compare the rate of lipid peroxyl radicals formation (i.e. initiation of lipid peroxidation) in different subcellular membranes, the experiment was repeated with 10 nM mito-H_5B-PMHC, lyso-H_4B-PMHC, or 100 nM of PM-H_4B-PMHC, as shown in **Figure 2.3d**. The rate of lipid peroxyl radical formation in each subcellular membrane was characterized by the time when enhancement starts, which marks the onset lipid peroxidation, and the time when enhancement plateaus, which marks the complete consumption of the probe. We found that upon RSL3 introduction, intensity of our PMHC probes all exhibited a short incubation time (~20 minutes), followed by a linear increase and finally plateauing at

~100 minutes. With all our PMHC probes, cell morphology started to change at ~100 minutes, right after complete antioxidant consumption, followed by PI enhancement starting at ~120 minutes.

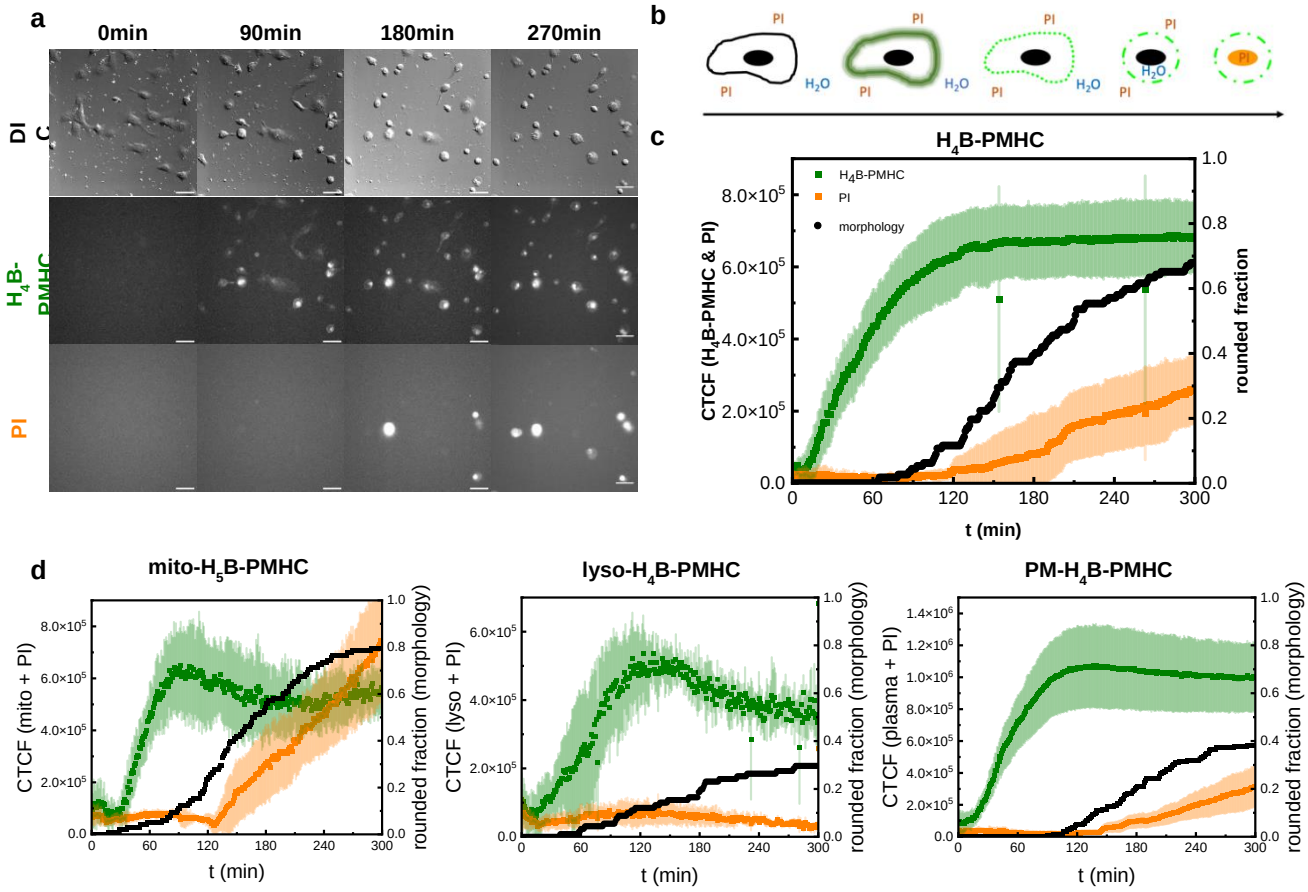

Figure 2.3: a) graphical representation of ferroptosis in real time, illustrating membrane oxidation, morphology change via water entry, and propidium iodide staining (nuclear membrane permeabilization). b) Representative multi-channel images of HT-1080 cell death with RSL3 as ferroptosis inducer (1 µM). Scale bar = 50 µm. c) Profile of HT-1080 cell ferroptotic cell death shown in b. Lipid peroxyl radical measured by H_4B-PMHC fluorescence (10 nM), bars = CTCF SEM, n = 4. Cell death marked visually by time of blebbing, n = 100. Membrane integrity assessed by PI (10 µM) fluorescence. Bars = CTCF SEM, n = 4. d) Enhancement of H_4B-PMHC (10 nM), mito-H_5B-PMHC (10 nM), lyso-H_4B-PMHC (10 nM), and PM-H_4B-PMHC (100 nM) during 5 hours of RSL3 treatment (1 uM). Bars = CTCF SEM.

Our results confirm that lipid peroxyl radicals are generated in all subcellular membranes of interest, including ER/lipid droplets, mitochondria, lysosomes, and PM, in ferroptosis induced by RSL3, contributing to the accumulation of lipid hydroperoxides which leads to ferroptotic cell death. In addition, we observed that, on average, lipid peroxidation initiates at similar rates in these subcellular

membranes. This is to say, while protection of ER/lipid droplets from lipid peroxidation is the most effective in ferroptosis inhibition, lipid peroxidation does not initiate faster in these organelles over the others.

2.4.4 Assessing ferroptosis rescuers in cell culture

To assess the impact of different antioxidants in live cells under ferroptosis, we next co-imaged ferroptotic cells treated with H_4B-PMHC along with other antioxidants, to assess its impact on H_4B-PMHC fluorescence (**Fig 2.4**). Here we monitored the temporal evolution of the fluorogenic antioxidant in the presence of competing antioxidants in HT-1080 cells in presence of RSL3. RTA more potent than H4B-PMHC are expected to prevent intensity enhancement and cell death, while those with lower antioxidant power would not impact the temporal profile of H_4B-PMHC. Propidium iodide (PI) was also added to the cellular imaging milieu to assess for membrane integrity.

When co-treated with the weak phenol-based antioxidant resveratrol (**Figure 2.4a**), up to a concentration of 100 nM, no significant effect can be observed on either H_4B-PMHC fluorescence nor on cell membrane integrity. Treating with PMHC (**Figure 2.4b**), the antioxidant analogue of H_4B-PMHC, a concentration dependence can be observed, with higher concentrations of PMHC co-treatment resulting in the abolishment of both H_4B-PMHC fluorescence and membrane permeabilization. Phenoxazine, identified as a potent lipophilic antioxidant and ferroptosis rescuer, completely suppressed both lipid peroxidation and membrane damage even at low concentrations (**Figure 2.4c**). H_4B-PMHC, can thus be used as an internal standard for assessing antioxidant strength in ferroptosis inhibition, with the reduction in fluorescence correlated with greater antioxidant strength.

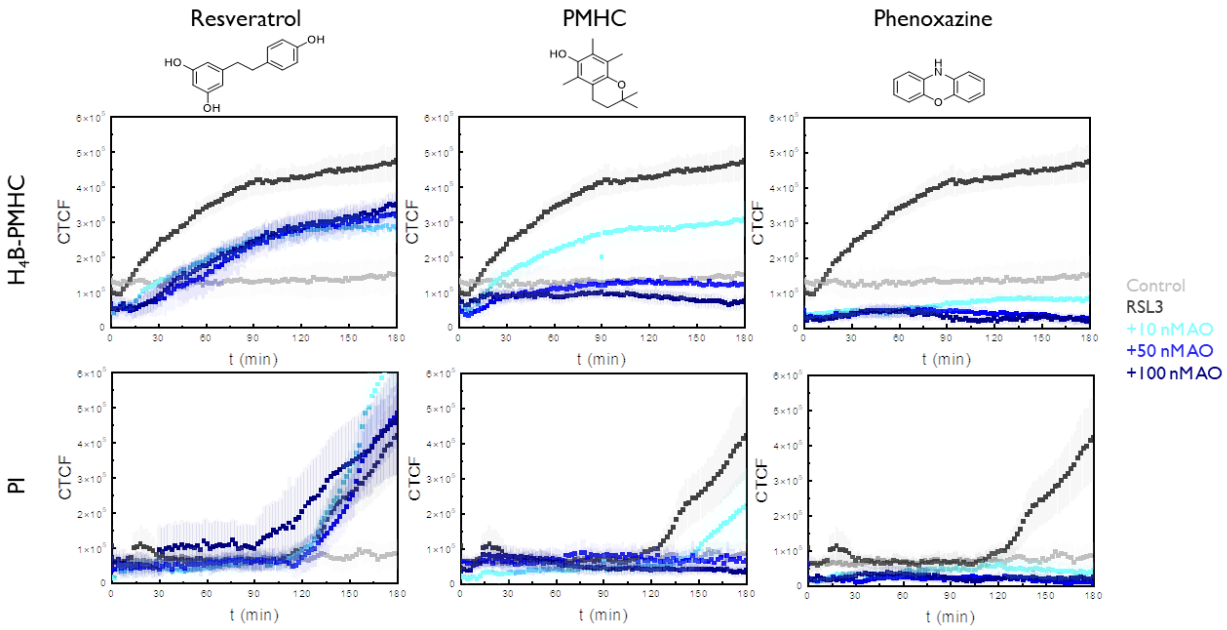

Figure 2.4: Cell fluorescence of HT-1080 cells imaged with H_4B-PMHC (top) and PI (bottom), supplemented with resveratrol (left, weak antioxidant), PMHC (centre, equivalent antioxidant), and phenoxazine (right, strong antioxidant). Bars = SEM, n = 4.

2.4.5 Single cell ferroptosis progression

To gain details on dynamics at the single cell and organelle level, we next conducted imaging at higher magnification and resolution. To visualize formation of lipid peroxyl radicals in lipid droplets and ER simultaneously and to compare their contributions to ferroptosis, we first performed super-resolved radial fluctuation (SRRF) on HT-1080 cells stained with 10 nM H4B-PMHC and treated with 1 µM RSL3. SRRF was chosen over other super-resolution methods given its low laser power requirements and low frame-count requirements for reconstruction, a compromise suitable for live cell imaging. Here we observed in the earliest timepoints (recorded at in the first hour following RSL3 treatment) the illumination of punctate, vesicular structures along with fluorescence intensity from perinuclear sites. Perinuclear membranes slowly became illuminated over time, until after ~75 minutes the illumination of the plasma membrane became apparent – in line with bulk studies (**Fig. 2.5**).

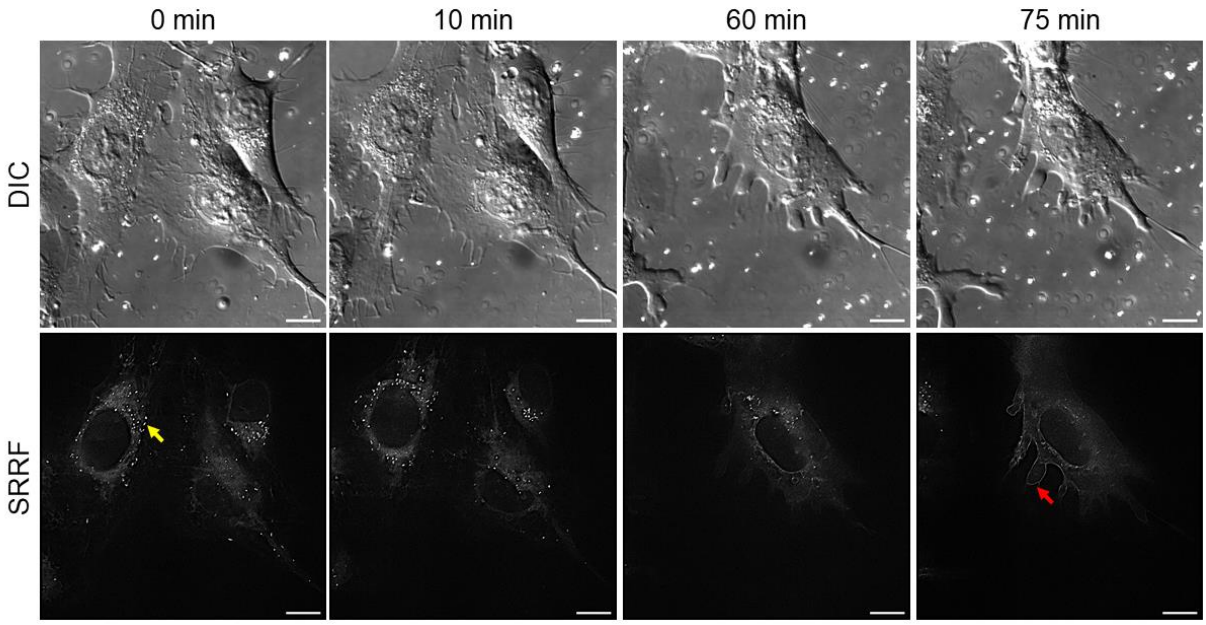

Figure 2.5: SRRF timelapse of H4B-PMHC in HT-1080 cells with RSL3 (1µM). Punctate structures resembling lipid droplets highlighted in earliest timepoint (yellow arrow), followed by the clear resolution of the plasma membrane towards end of observation window (red arrow). Scale bars = 10 microns.

To identify these perinuclear and puncta sites, HT-1080 cells were co-stained with H_4B-PMHC (10 nM) and either ER Tracker Red (1 µM) to label the ER or 1x LipidSpot 610 to label lipid droplets, and treated with 1 µM RSL3. As shown in **Figure 2.6a**, within an hour following RSL3 treatment, a clear induction of fluorescence enhancement is observed in punctate structures, concomitant with weak signals in perinuclear regions. In the next 2 hours, fluorescence continued to enhance at both sites, then colocalization with ER Tracker is gradually lost as PM illumination becomes apparent. Colocalization with ER Tracker revealed that perinuclear sites are ER membranes. In contrast, bright puncta observed do not colocalize with the lipid droplet stain LipidSpot 610 **(Fig 2.6b)**. We hypothesize these punctate structures as secretory vesicles of oxidized lipids, during early stages of ferroptosis. Interestingly, these bright puncta become less apparent as ferroptosis progresses, suggesting likely export or merger with other membranes.

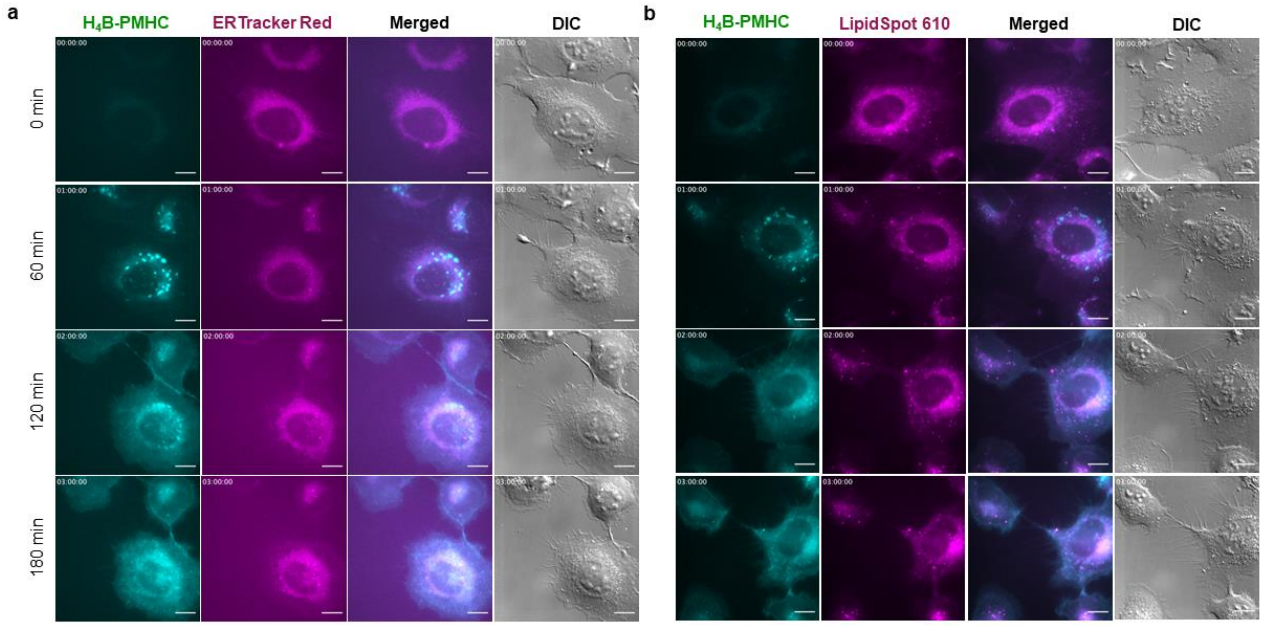

Figure 2.6: 100x HILO timelapses of **H_4B-PMHC** in HT-1080 cells with RSL3 (1 µM), co-stained with a) ERTracker Red (1 uM) or b) 1x LipidSpot 610.

In addition, with H_4B-PMHC, PM illumination is observed concomitant with a gradual loss of signal in puncta. This phenomenon became particularly prominent in late stage of ferroptosis (**Fig. 2.5**). However, H_4B-PMHC is expected to have a similar distribution in the cell with its fluorescent control compound H_4B-CH_3, which shows no staining of PM. This suggests that the adduct between H_4B-PMHC and oxidized lipid (**Fig. 2.1a**) initially formed in the internal membranes is trafficked to the PM as ferroptosis progresses.

2.4.6 PM is a sink and a source of oxidized lipids

To investigate whether the oxidized lipids are also trafficked from mitochondria and lysosomes to PM, the experiment was repeated with mito-H_5B-PMHC and lyso-H_4B-PMHC, co-stained with MitoTracker Deep Red and LysoTracker Deep Red, respectively. As shown in **Figure 2.7a** and **2.7b**, colocalization is initially observed at the onset of fluorescence imaging, along with a corresponding increase in fluorescence intensity due to lipid peroxidation. However, after approximately two hours, prominent fluorescence in the plasma membrane can be observed, along with a loss of colocalization with the MitoTracker or LysoTracker. Considering that loss of dye targeting specificity can result from many other

reasons, such as mitochondria depolarization or simply cleavage of the targeting group from the fluorophore. To rule out this possibility, two fluorescent control compounds, mito-H_5B-CH_3 and lyso-H_4B-CH_3, are employed. Lacking the chromanol warhead, these control compounds do not form fluorescent adducts with lipid peroxyl radicals. As shown in **Figure 2.7c** and **2.7d**, mito-H_5B-CH_3 and lyso-H_4B-CH_3 exhibited good colocalization with MitoTracker Deep Red and LysoTracker Deep Red, respectively, throughout the 3-hour of RSL3 treatment, confirming that tethering the dye to oxidized lipids is necessary for dye trafficking to occur.

In contrast to results with the previous three PMHC probes, with PM-H_4B-PMHC, we observed no trafficking events from the PM to the internal membranes. As shown **Figure 2.7e**, prominent fluorescence enhancement is observed within 2 hours, and showed good colocalization with the red channel throughout the experiment. These results collectively suggest that oxidized lipids initially formed in the internal membranes are trafficked unidirectionally to PM. Two processes are identified that contribute to the lethal accumulation of lipid hydroperoxides in PM: i) PM lipid peroxidation and ii) trafficking of oxidized lipid initially formed in internal membranes to PM. In other words, PM is both a source and a sink of oxidized lipids.

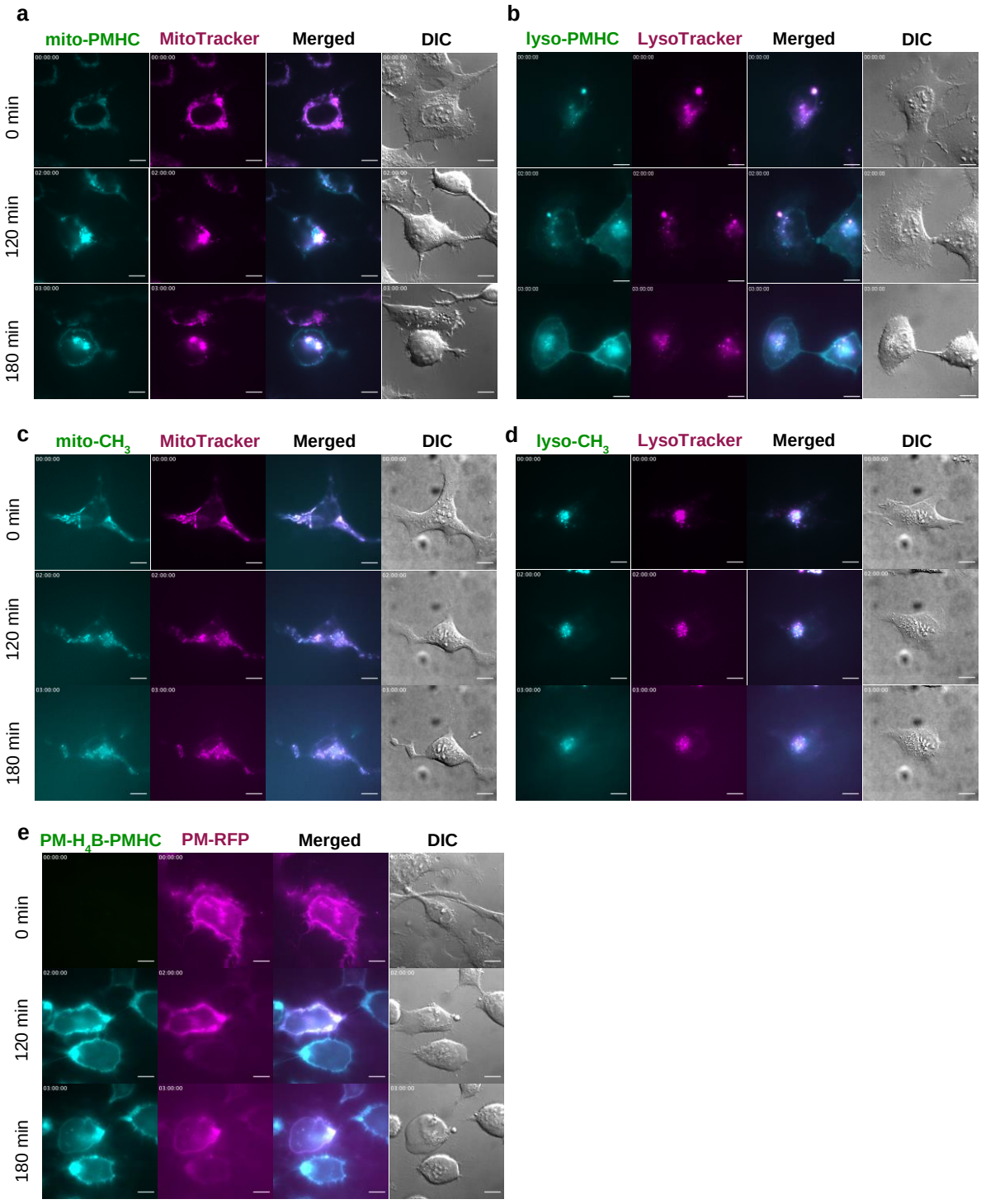

Figure 2.7: 100x HILO timelapses of our PMHC probes in HT-1080 cells treated with RSL3 (1 µM). a) mito-H_5B-PMHC (10 nM) co-stained with MitoTracker Deep Red (25 uM). B) lyso-H_4B-PMHC (10 nM) co-stained with LysoTracker Deep Red (75 nM). c) HT-1080 cells transfected with PM-RFP and stained with PM-H_4B-PMHC (100 nM). d) mito-H_5B-CH_3 (10 nM) co-stained with MitoTracker Deep Red (25 uM). e) lyso-H_4B-CH_3 (10 nM) co-stained with LysoTracker Deep Red (75 nM).

2.4.7 Usage of probes

A point of consideration in the usage of H_4B-PMHC is its comparison to C11 BODIPY 581/591 – a commonly used, promiscuous probe for lipid peroxidation. Clear differences need to be drawn in identifying the merits of each probe and their applications. C11 BODIPY acts as a fluorescent unsaturated lipid analogue, whose emission shifts to shorter wavelengths upon oxidation of its diene interconnection.[23] In a sense, the probe serves as a radical chain propagator. In comparison, H_4B-PMHC, and related compounds used herein act as radical chain terminators, and display antioxidant capacity. As such, experimental conditions need to be considered in studying ferroptosis, as high probe load will delay, if not prevent, ferroptosis – the object of observation. Thus, signal-to-noise and excess antioxidant perturbation to the system need to be balanced. We showed that at an excess of H_4B-PMHC abolishes fluorescence enhancement due to the inhibition of ferroptosis within the timespan of live cell imaging. A 10 nM concentration was shown to be optimum for fluorescence imaging in all modalities (widefield, TIRF/HILO, SRRF), exhibiting minimal perturbation to the antioxidant load while still maintaining good signal-to-noise. This is in sharp contrast to C11 BODIPY, which is usually employed more as a stain than a dye, for taking static measurements instead of in real-time. In addition, the concentration used is usually in the micromolar range compared to nanomolar, which will perturb cell physiology to a greater extent. Thus, our measurements with H_4B-PMHC and its organelle targeted derivatives provide, to the best of our knowledge, the first live cell observations of lipid peroxidation initiation and progression in ferroptosis via direct induction of RSL3.

2.4.8 Potencies of our PMHC probes in ferroptosis suppression

With our palette of PMHC probes used in cell viability assay, we provide an indirect measurement of the efficacy of an equivalent amount of antioxidants delivered to different organelles in ferroptosis rescue. With the equivalent amount (100 nM) of our PMHC probes, we found that H_4B-PMHC exhibited the greatest cell viability, followed by lyso-H_4B-PMHC and mito-H_5B-PMHC, with PM-H_4B-PMHC being the

least potent in ferroptosis rescue. While H_4B-PMHC is non-specifically targeted, it accumulates mainly in the ER and lipid droplets due to its high lipophilicity. We conclude that accumulation of antioxidants in all the subcellular membranes of interest exhibited a certain degree of ferroptosis suppression, and the efficacy can be ranked in descending order: ER/lipid droplets, lysosomes, mitochondria, and PM. Our results align with the work of Stockwell, Min, and Woerpel in using organelle-targeted $FINO_2$ derivatives, serving as a lipophilic endoperoxide, observing the ER to be the key site of ferroptosis sensitivity.[12] Stockwell and colleagues show the ER to be the most sensitive site of ferroptosis induction, and this work complements by showing the ER to be the most effective site of ferroptosis inhibition. We present a physical hypothesis for the relative importance of the ER over other organelles in ferroptosis suppression. As the ER has the largest surface area and thus the highest number of lipid molecules in the cell, a lipid peroxyl radical has a longer lifetime – a reflection of the average distance between membrane antioxidants – in the ER versus in other organelles. As lipid peroxidation is an autocatalytic process, a longer radical lifetime results in a larger chain (i.e. more lipids becoming peroxidized). Therefore, intervention by adding antioxidants and shortening lifetime has a relatively greater impact on the ER than elsewhere. Many variables need to be accounted for, such as antioxidant concentration in each organelle membrane, membrane surface area, etc. Some, such as modulating the size of the ER, are experimentally very challenging. Future studies involving more rigorous kinetic measurements and molecular dynamics studies could help elucidate further the reason for organelle specificity of ferroptosis sensitivity.

In addition, our results highlight the role of mitochondria and lysosomes protection. It has been previously shown by Stockwell and Min that accumulation of ferrostatin-1, an antioxidant-based ferroptosis inhibitor, in mitochondria and lysosomes does not contribute to ferroptosis inhibition.[10] Interestingly, ferrostatin-1 has a much higher erastin-suppressing potency than Trolox, presumably due to its unique profile of radical reactivity compared to phenolic antioxidants.[24] We reason that the

discrepancy we observe may due to higher lipophilicity and targeting specificity of our PMHC probes, emphasising key aspects to consider for developing more potent ferroptosis inhibitors.

2.4.9 Usage of H_4B-PMHC as an internal standard for ferroptosis rescuer assessment

Ferroptosis rescue does not correlate directly with antioxidant potential in solution, shown by Shah and coworkers.[25] Factors such as lipophilicity and accessibility of the antioxidant to lipid peroxides produced influence the efficacy of a potential ferroptosis rescuer/antioxidant. Here, we show H_4B-PMHC occupies a unique position as not only a reporter, but a measuring stick as well. We showed using antioxidants positioned at above and below the ferroptosis rescuing capability of PMHC, the parent antioxidant moiety of our probes, that only ferroptosis rescuers with equivalent or better activity than PMHC can suppress or retard H_4B-PMHC fluorescence. We envision that H_4B-PMHC provides an elegant tool in high throughput screening applications, as a criterion to filter out and select for promising candidates in therapeutics.

2.4.10 Towards the quantification of lipid peroxidation rate in ferroptosis

An actual quantification of lipid peroxidation rates with ferroptosis induction, while possible, is not free from approximations and errors thus introduced. Reasons for this include the difficulty in quantifying the actual intracellular probe concentration due to the complex equilibria between probe partition (into cells) and probe binding to BSA in the media. In addition, the onset of probe enhancement has a certain degree of uncertainty due to the convoluted rates of various processes, such as the portioning of RSL3 into the cell at the start of experiments. However, from stoichiometry, we can provide a maximalist, ceiling rate of lipid peroxyl radical production from the bulk experiment studies. We can assume that the plateau of H_4B-PMHC fluorescence in bulk studies represents the time of total antioxidant consumption, occurring at approximately 100 minutes. Given the 1:2 stoichiometric ratio at which H_4B-PMHC reacts with lipid peroxyl radicals, we can assume that the total number of dye molecules (10 nM in

300 µL media) distributed evenly across the total number of cells (30 000) yields 1.2 x 10^8 molecules peroxyl radicals, for a maximum rate of 1 200 000 radicals per minute. Future works to control more precisely the exact concentration of active antioxidant-bearing probes can be used to more accurately qualify some of the assumptions used and provide more valuable, accurate, and overall useful figures.

2.4.11 Observations on ferroptosis

Multichannel fluorescence imaging allowed us to observe the execution of ferroptotic cell death as an ordered series of events which fundamentally distill down to a physical process – lipid peroxidation overwhelming antioxidant capacity, until pore formation from lipid peroxidation byproducts lead to water entry into the cytoplasm, and finally catastrophic loss of membrane integrity. This is in line with the work of Garcia-Saez and coworkers, who showed that cells undergoing ferroptosis can be rescued by blocking the membrane pores with PEG micelles[26], physically preventing water entry into the cytoplasm. We posit that the cause of membrane permeabilization is lipid-derived aldehydes, shown in our previous collaboration to be capable of lowering the free energy barrier of water molecules crossing the lipid bilayer in molecular dynamics studies.[27]

In bulk, all our PMHC probes exhibited similar fluorescence enhancement curves upon RSL3 treatment, suggesting that lipid peroxidation in ER/lipid droplets, mitochondria, lysosomes, and PM all happen at approximately the same stage and rate following RSL3 treatment. However, with C11-BODIPY, it has been observed that ER exhibited a higher ox/red ratio than PM at early stage of ferroptosis, suggesting ER is oxidized prior to PM.[12] Since measurements with C11-BODIPYs are taken at discrete time points to capture ferroptosis progression, ox/red ratio is a reflection more of the amount of lipid peroxides accumulated at a specific site than of lipid peroxyl radials being generated locally. In contrast, our PMHC probes offer a more continuous, real-time measurement, whose fluorescence enhancement directly correlates with generation of lipid peroxyl radicals. As such, observations with C11-BODIPY and with our

PMHC probes can be considered to complement each other, offering a more complete picture on how different subcellular membranes are involved in ferroptosis: while lipid peroxides first accumulate in ER and followed by PM, at these sites lipid peroxidation initiates and progresses at similar stages and rates.

At the single cell level, high-resolution imaging employing H_4B-PMHC indicates that in RSL3-induced ferroptosis, lipid peroxidation in lipid droplets is observed concomitantly with the ER. While PUFA storage in lipid droplets have been shown to protect membranes from PUFA oxidation,[28] we found that lipid droplets are still essential sites for lipid peroxidation in ferroptosis. Further investigation regarding mechanisms of lipid droplets peroxidation is needed to elucidate their roles in regulating ferroptosis.

We also present evidence via our high-resolution imaging that the plasma membrane is both a sink and a source of lipid peroxidation. Preferential accumulation of lipid hydroperoxides at the plasma membrane has now been established as a hallmark of ferroptosis,[9] primarily observed via C11 BODIPY imaging (see above for a discussion of its usage vs RTA fluorogenic probes). However, it was not established whether lipid peroxidation occurred locally at the site of the plasma membrane, or lipid peroxidation products were trafficked from elsewhere in the cell towards the plasma membrane – whether via an active or passive mechanism. Our results support that both mechanisms contribute to the observed accumulation of oxidized lipids in PM. On one hand, with PM-H_4B-PMHC, fluorescence enhancement is observed exclusively at PM throughout the experiment, indicating lipid peroxyl radicals are produced locally at PM upon GPX4 inhibition. On the other hand, with mito-H_5B-PMHC and lyso-H_4B-PMHC, we present evidence of trafficking. After induction of ferroptosis, both organelle-specific probes exhibited fluorescence enhancement within their respective targeted organelles, indicating lipid peroxidation, which over time colocalization gradually decreased and a pronounced plasma membrane staining became apparent. As probe activation comes from the adduct formation between a lipid peroxyl radical with the PMHC moiety of the RTA probe, the appearance of fluorescence in the plasma membrane despite passive organelle targeting could only occur via an active mechanism, transporting probe-oxidized

lipid adducts from their respective sites of formation to the plasma membrane. Further investigation, via higher resolution and/or single particle tracking, would help to clarify this picture, however the bulk evidence presents evidence to support the active mechanism.

2.5 Conclusions:

Armed with a palette of tocopherol-analogue fluorogenic probes for lipid peroxidation, we present an effective toolbox for the study of ferroptosis, demonstrating both proof-of-concept for applied usage as well as fundamental discovery. H4B-PMHC and its organelle targeted analogues demonstrate an order of magnitude increase in sensitivity over other lipid peroxidation probes (C11 BODIPY). We show H_4B-PMHC to be capable of observing real-time induction of ferroptosis from start to finish, as well as an internal standard in the assessment of ferroptosis rescuers. With organelle-targeted moieties, we lend support to the plasma membrane being a sink not a source of oxidized lipids.

2.6 Materials and methods:

2.6.1 Materials:

Cell culture reagents were purchased through ThermoFisher Scientific. FluoroDish (35mm, FD35) imaging dishes were purchased through World Precision Instruments, Inc. µ-Slide 8 well (ibiTreat, glass bottom, cat. no. 80827) chambered coverslips were purchased through Ibidi, USA.

2.6.2 Cell Culture:

HT-1080 cells (ATCC CCL-121) were obtained via a material transfer agreement from the Brent Stockwell laboratory (Columbia University) and cultured in DMEM with glutamine and sodium pyruvate (Gibco: 11995-065) and supplemented with 10% FBS (Gibco: A31607-02), 1% penicillin-streptomycin (Gibco: 15140) and 1x Non-Essential Amino Acids (Gibco: 11140050). Cells were maintained at 37 °C and 5% humidified CO_2 in a tissue incubator, and passaged regularly at sub-confluency.

Buthionine Sulfoximine treatment: cells were plated at a density of 15000/well and treated with 10 µM BSO (solubilized in PBS) directly into culture media, incubated overnight for 12-24hr. Prior to imaging, cells were washed 3x with LCIS + 5% glucose, and incubated with H4B-PMHC (100 nM, 0.33% DMSO) for 10 minutes. Cells were then transferred into phenol-free DMEM and imaged.

Propidium iodide: PI (10µM, 0.33% DMSO) was co-administered with treatments – control (0.33% DMSO), RSL3 (1uM, 0.33% DMSO) on HT-1080 cells in phenol-free DMEM media (10% FBS, 1x penicillin-streptomycin, 1x non-essential amino acids). Imaging was conducted at 20x magnification widefield fluorescence (488nm, 0.1mW laser power, 50ms, 1 frame/min for 3 hours) using the same microscopy setup as mentioned above.

Mitochondria and lysosome co-staining: MitoTracker Deep Red and LysoTracker Deep Red were used. 15 minutes prior to cell imaging, cells were stained with Mito/LysoTracker in media, prior to washing out and preparing in accordance to BODIPY imaging protocols outlined above.

Resazurin Cell Death Assay: Dose response to RSL3 was characterized by resazurin reduction assay. Cells were seeded 24 hours prior to treatment at a density of 10 000/well in 100 µL in tissue-cultured treated 96-well plates (Corning). A co-treatment of RSL3 (D2 dilution series descending from 1 µM) with 100 nM H_4B-PMHC, 100 nM PMHC, or vehicle control (DMSO) was added to the plates (50 µL additional volume for 150 µL total, 0.33% final DMSO concentration in DMEM culture media) and incubated for three hours. Post-treatment, the media was exchanged with rezasurin (44µM in DMEM culture media) and further incubated for 3 hours. The viability was then assessed by measuring resazurin intensity (ex: 570 nm, em: 590 nm) via a plate reader.

2.6.3 Microscopy:

Images were acquired on a Nikon Eclipse Ti2 microscope, with brightfield differential interference contrast (DIC), epifluorescence, spinning disk confocal (CREST X-Light V2 L-FOV) and total internal

reflection fluorescence (TIRF) modalities. The unit was equipped with a Perfect Focus System (PFS) and a motorized filter block turret for multichannel imaging. Cells were maintained at 37 °C and 5% humidified CO_2 with a stage-top incubator (Tokai Hit). For TIRF and SRRF images, fluorescence excitation (488 nm) was filtered using a multiband beam splitter (ZT488/640rpc, Chroma Technology). Emissions were captured using a back illuminated EM-CCD camera (Andor iXon Ultra DU-897).

2.6.4 Cell Imaging:

Cells were seeded one day prior to imaging, 15 000 cells/well in ibidi 8-well slides for widefield experiments and 30 000 cells per dish for TIRF experiments. Widefield fluorescence experiments were performed using a 20x objective (Nikon CFI Plan Apo VC 20x, NA = 0.75, air, DIC). TIRF was imaged utilizing a 100x objective (Nikon CFI SR Apochromat TIRF 100x, NA = 1.49, oil, DIC)

2.6.5 Image Analysis:

CTCF: Image analysis was performed using FIJI/ImageJ[29]. Quantifications of fluorescence enhancements in cells by corrected total cell fluorescence (CTCF) was previously utilized by our group[21, 30, 31] and adapted from previously published protocol[32]:

$$CTCF = \frac{IntDensity_{totalcellarea} - (total\ cell\ area\ \times BkgFluorescence)}{N_{cells}}$$

Where $IntDensity_{totalcellarea}$ is the integrated intensity of the pixels for all cells in the image, $total\ cell\ area$ is the number of pixels of all the cells, BkgFluorescence is the mean fluorescence intensity per pixel for a region containing no cells and N_{cells} is the number of cells in the image. A FIJI macro was used to identify cell area from DIC images via a variance-based method.[31]

Cell Death Timeline: For each field of view, the time at which cells reach a rounded morphology (Fig S3) from flat was marked and counted individually. Four FOVs were compiled and summed for population statistics.

Super Resolution Radial Fluctuation (SRRF): SRRF imaging of H_4B-PMHC was conducted at 100x/1.45 NA TIRF modality, in the same imaging set up as described above. Cell imaging was done in the same condition as described above. At each time point, 100 frames were acquired at 20 ms exposure time (2s exposure in total). Image processing was done using default settings on the nanoJ-SRRF plugin in FIJI/ImageJ.

2.7 Supplementary information:

2.7.1 Photophysical characterization of probe

Table S2.1: Photophysical properties of novel organelle-targeting dyes in acetonitrile

	$\boldsymbol{\varepsilon}$ $(\times \mathbf{10^3}\ \boldsymbol{M^{-1}cm^{-1}})$	$\boldsymbol{\phi_{fl}}$	**Fluorescence lifetime (ns)**
H_4B-PMHC [a]	8.2	0.001	NA
H_4B-CH3 [a]	7.9	0.94	5.60
Mito- H_5B-PMHC	5.4	0.012	6.54
Mito- H_5B-CH3	4.8	0.7	6.38
Lyso- H_4B-PMHC	7.5	0.004	0.14, 0.44
Lyso- H_4B-CH3	6.8	0.65	0.9
PM- H_4B-PMHC [b]	8.2	0.013	0.16, 5.62
PM- H_4B-CH3 [b]	8.2	0.8	5.51

a – previously reported[21], b – values measured in methanol instead of acetonitrile

2.7.2 Behaviour of probe in cells

We examined the stability and fidelity of our probes once reacted with peroxyl radicals in cells (**Fig. S2.1**). To generate the necessary buildup of radicals, cells were treated with RSL3 – the direct inhibitor of GPX4 – for 1 hour. H_4B-PMHC was added to cells in Live Cell Imaging Solution (LCIS, a HEPES-based buffer) and its cellular enhancement upon reactivity monitored via imaging. The maximum of fluorescence enhancement/CTCF was reached at approximately one hour. At the point of CTCF plateau, at which all free dye has been consumed, the media was exchanged to phenol-free DMEM – to better reflect the imaging conditions above. At this point, the fluorescence trajectory can be seen declining, until reaching a plateau of approximately half the original maximum. The enduring fluorescence shows

the fidelity of H_4B-PMHC has both a positional and a spatiotemporal marker of lipid peroxidation generated in ferroptosis.

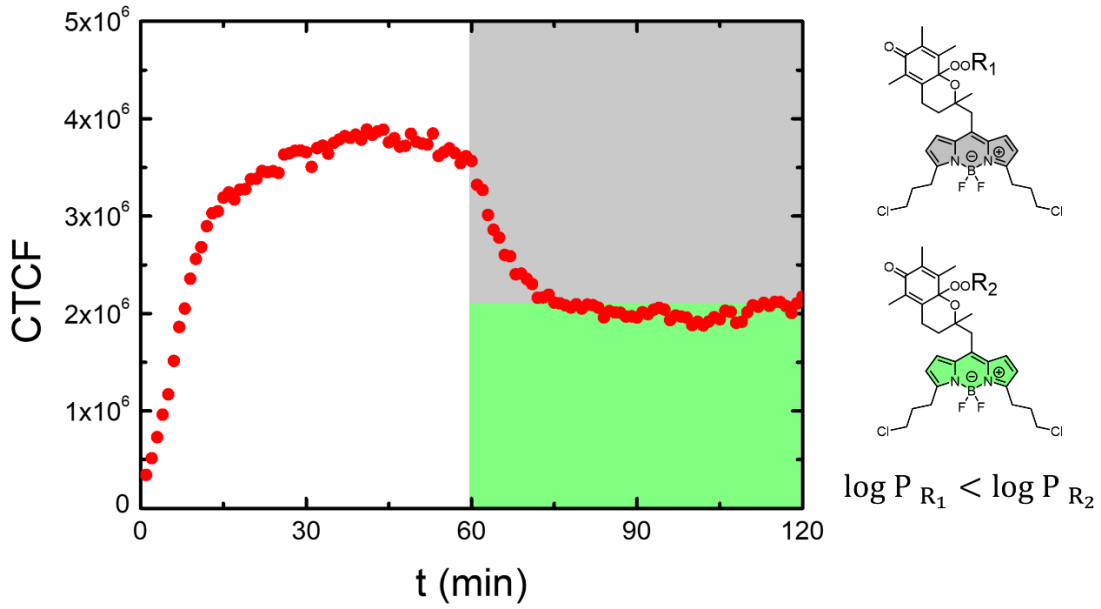

Figure S2.1: H4B-PMHC fluorescence (100 nM) in HT-1080 cells pre- and post-media exchange. Lipid peroxidation was induced with RSL3 (1µM) in LCIS (white region) and then exchanged into phenol-free DMEM (grey/green region).

2.7.3 Indirect inhibition of GPX4

To observe long timescale induction of ferroptosis via the indirect inhibition of GPX4, we used the small molecule inhibitor buthionine sulfoxomine (BSO, Fig. S2.2). GPX4 activity can also be indirectly regulated via its substrate glutathione. BSO is a bonafide downregulator of intracellular glutathione concentration by acting as a substrate mimic in a key step of glutathione biosynthesis[33]. We treated cells with BSO for varying amounts of time, up to 24 hours, prior to incubating and imaging with H_4B-PMHC. We observe that cell fluorescence is directly related to the length of BSO exposure. With longer treatment of BSO, more glutathione is depleted, and therefore less GPX4 activity and more lipid peroxidation. Therefore, H_4B-PMHC can be used to correlate the cumulative oxidative stress cells have been subjected to, on the timescale of tens of hours, making it a useful tool for assessing indirect inhibition of GPX4 via glutathione synthesis inhibition.

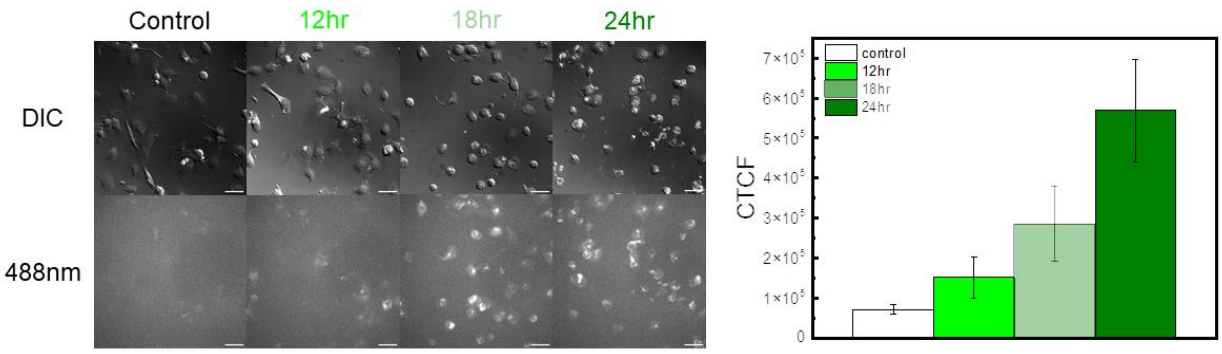

Figure S2.2: Profile of **H_4B-PMHC** fluorescence (100 nM), corresponding to lipid peroxidation, post BSO treatment (12-24hr, 10 µM). Bars = CTCF SEM, n = 4.

2.7.4 Full timeline of ferroptosis with organelle targeted PMHC probes

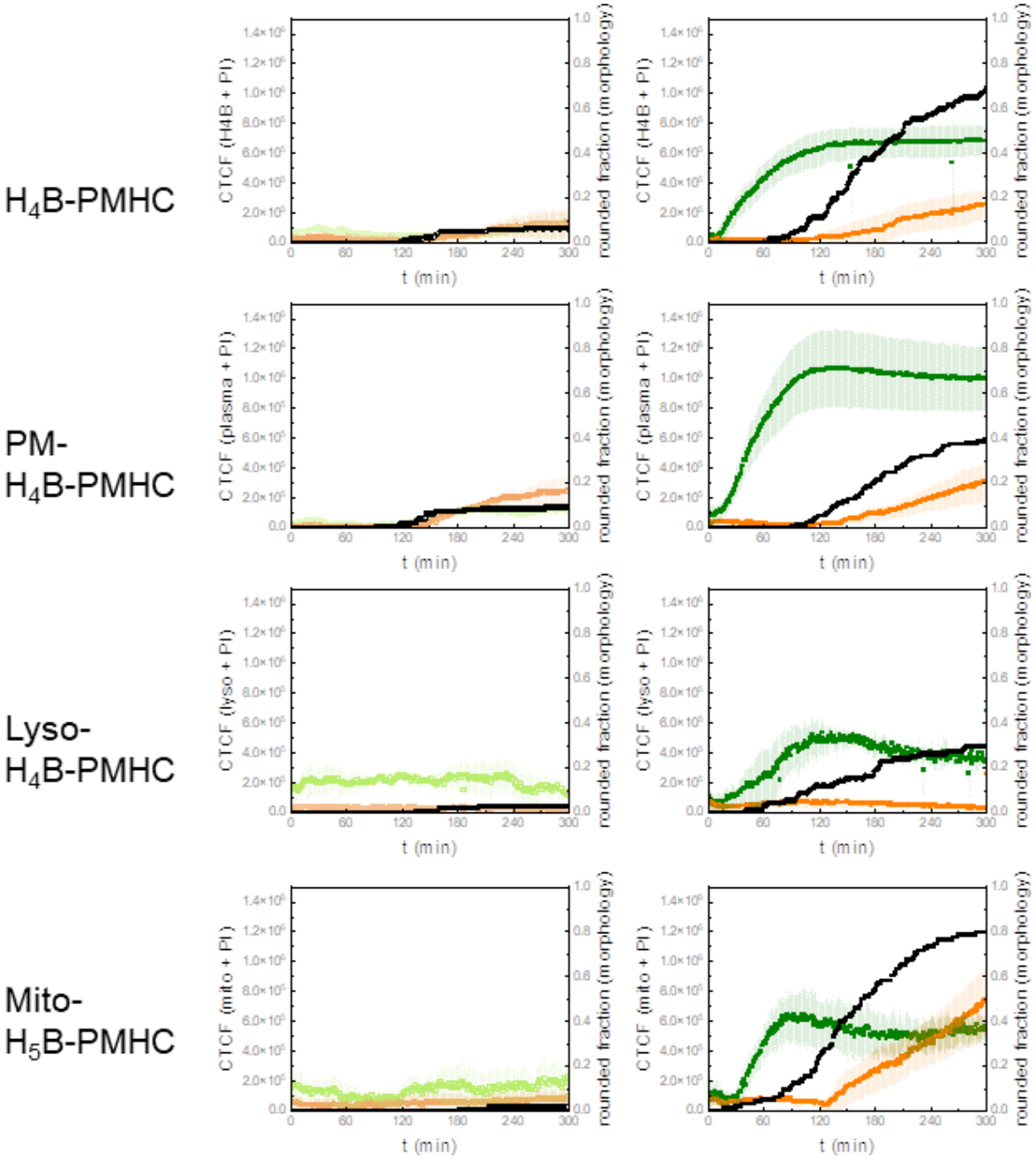

Figure S2.3: Profile of HT-1080 cell death with RSL3 ferroptosis inducer (1 µM, right column) and in basal (left row) conditions. Lipid peroxyl radical measured by H_4B-PMHC fluorescence (10 nM), bars = CTCF SEM, n = 4. Cell death marked visually by time of blebbing, n = 100. Membrane integrity assessed by PI (10 µM) fluorescence. Bars = CTCF SEM, n = 4.

2.8 References

(1) Dixon, S. J.; Lemberg, K. M.; Lamprecht, M. R.; Skouta, R.; Zaitsev, E. M.; Gleason, C. E.; Patel, D. N.; Bauer, A. J.; Cantley, A. M.; Yang, W. S. Ferroptosis: an iron-dependent form of nonapoptotic cell death. *cell* **2012**, *149* (5), 1060-1072.
(2) Bersuker, K.; Hendricks, J. M.; Li, Z.; Magtanong, L.; Ford, B.; Tang, P. H.; Roberts, M. A.; Tong, B.; Maimone, T. J.; Zoncu, R.; et al. The CoQ oxidoreductase FSP1 acts parallel to GPX4 to inhibit ferroptosis. *Nature* **2019**, *575* (7784), 688-692. DOI: 10.1038/s41586-019-1705-2.
(3) Yang, W. S.; Stockwell, B. R. Synthetic Lethal Screening Identifies Compounds Activating Iron-Dependent, Nonapoptotic Cell Death in Oncogenic-RAS-Harboring Cancer Cells. *Chemistry & Biology* **2008**, *15* (3), 234-245. DOI: https://doi.org/10.1016/j.chembiol.2008.02.010.
(4) Stockwell, B. R.; Friedmann Angeli, J. P.; Bayir, H.; Bush, A. I.; Conrad, M.; Dixon, S. J.; Fulda, S.; Gascón, S.; Hatzios, S. K.; Kagan, V. E.; et al. Ferroptosis: A Regulated Cell Death Nexus Linking Metabolism, Redox Biology, and Disease. *Cell* **2017**, *171* (2), 273-285. DOI: 10.1016/j.cell.2017.09.021 From NLM.
(5) Chen, Y.; Fang, Z.-M.; Yi, X.; Wei, X.; Jiang, D.-S. The interaction between ferroptosis and inflammatory signaling pathways. *Cell Death & Disease* **2023**, *14* (3), 205.
(6) Jiang, X.; Stockwell, B. R.; Conrad, M. Ferroptosis: mechanisms, biology and role in disease. *Nature Reviews Molecular Cell Biology* **2021**, *22* (4), 266-282. DOI: 10.1038/s41580-020-00324-8.
(7) Zhou, Y.; Zhen, Y.; Wang, G.; Liu, B. Deconvoluting the Complexity of Reactive Oxygen Species (ROS) in Neurodegenerative Diseases. *Frontiers in Neuroanatomy* **2022**, *16*, Mini Review. DOI: 10.3389/fnana.2022.910427.
(8) Foret, M. K.; Lincoln, R.; Do Carmo, S.; Cuello, A. C.; Cosa, G. Connecting the "Dots": From Free Radical Lipid Autoxidation to Cell Pathology and Disease. *Chemical Reviews* **2020**, *120* (23), 12757-12787. DOI: 10.1021/acs.chemrev.0c00761.
(9) Magtanong, L.; Ko, P. J.; To, M.; Cao, J. Y.; Forcina, G. C.; Tarangelo, A.; Ward, C. C.; Cho, K.; Patti, G. J.; Nomura, D. K.; et al. Exogenous Monounsaturated Fatty Acids Promote a Ferroptosis-Resistant Cell State. *Cell Chem Biol* **2019**, *26* (3), 420-432.e429. DOI: 10.1016/j.chembiol.2018.11.016 From NLM.
(10) Gaschler, M. M.; Hu, F.; Feng, H.; Linkermann, A.; Min, W.; Stockwell, B. R. Determination of the Subcellular Localization and Mechanism of Action of Ferrostatins in Suppressing Ferroptosis. *ACS Chemical Biology* **2018**, *13* (4), 1013-1020. DOI: 10.1021/acschembio.8b00199.
(11) Gao, M.; Yi, J.; Zhu, J.; Minikes, A. M.; Monian, P.; Thompson, C. B.; Jiang, X. Role of Mitochondria in Ferroptosis. *Mol Cell* **2019**, *73* (2), 354-363.e353. DOI: 10.1016/j.molcel.2018.10.042 From NLM.
(12) von Krusenstiern, A. N.; Robson, R. N.; Qian, N.; Qiu, B.; Hu, F.; Reznik, E.; Smith, N.; Zandkarimi, F.; Estes, V. M.; Dupont, M.; et al. Identification of essential sites of lipid peroxidation in ferroptosis. *Nature Chemical Biology* **2023**, *19* (6), 719-730. DOI: 10.1038/s41589-022-01249-3.
(13) Gao, M.; Yi, J.; Zhu, J.; Minikes, A. M.; Monian, P.; Thompson, C. B.; Jiang, X. Role of Mitochondria in Ferroptosis. *Molecular Cell* **2019**, *73* (2), 354-363.e353. DOI: https://doi.org/10.1016/j.molcel.2018.10.042.
(14) Torii, S.; Shintoku, R.; Kubota, C.; Yaegashi, M.; Torii, R.; Sasaki, M.; Suzuki, T.; Mori, M.; Yoshimoto, Y.; Takeuchi, T.; Yamada, K. An essential role for functional lysosomes in ferroptosis of cancer cells. *Biochemical Journal* **2016**, *473* (6), 769-777. DOI: 10.1042/bj20150658 (acccessed 11/30/2023).
(15) Lin, Z.; Liu, J.; Kang, R.; Yang, M.; Tang, D. Lipid Metabolism in Ferroptosis. *Advanced Biology* **2021**, *5* (8), 2100396. DOI: https://doi.org/10.1002/adbi.202100396 (acccessed 2023/08/17).
(16) Magtanong, L.; Ko, P.-J.; To, M.; Cao, J. Y.; Forcina, G. C.; Tarangelo, A.; Ward, C. C.; Cho, K.; Patti, G. J.; Nomura, D. K.; et al. Exogenous Monounsaturated Fatty Acids Promote a Ferroptosis-Resistant Cell State. *Cell Chemical Biology* **2019**, *26* (3), 420-432.e429. DOI: https://doi.org/10.1016/j.chembiol.2018.11.016.

(17) Pope, L. E.; Dixon, S. J. Regulation of ferroptosis by lipid metabolism. *Trends in Cell Biology* **2023**. DOI: https://doi.org/10.1016/j.tcb.2023.05.003.
(18) Magtanong, L.; Mueller, G. D.; Williams, K. J.; Billmann, M.; Chan, K.; Armenta, D. A.; Pope, L. E.; Moffat, J.; Boone, C.; Myers, C. L.; et al. Context-dependent regulation of ferroptosis sensitivity. *Cell Chemical Biology* **2022**, *29* (9), 1409-1418.e1406. DOI: 10.1016/j.chembiol.2022.06.004 (acccessed 2023/08/11).
(19) Kagan, V. E.; Mao, G.; Qu, F.; Angeli, J. P. F.; Doll, S.; Croix, C. S.; Dar, H. H.; Liu, B.; Tyurin, V. A.; Ritov, V. B.; et al. Oxidized arachidonic and adrenic PEs navigate cells to ferroptosis. *Nature Chemical Biology* **2017**, *13* (1), 81-90. DOI: 10.1038/nchembio.2238.
(20) Chen, Y.; Liu, Y.; Lan, T.; Qin, W.; Zhu, Y.; Qin, K.; Gao, J.; Wang, H.; Hou, X.; Chen, N.; et al. Quantitative Profiling of Protein Carbonylations in Ferroptosis by an Aniline-Derived Probe. *Journal of the American Chemical Society* **2018**, *140* (13), 4712-4720. DOI: 10.1021/jacs.8b01462.
(21) Greene, L. E.; Lincoln, R.; Cosa, G. Rate of Lipid Peroxyl Radical Production during Cellular Homeostasis Unraveled via Fluorescence Imaging. *Journal of the American Chemical Society* **2017**, *139* (44), 15801-15811. DOI: 10.1021/jacs.7b08036.
(22) Gustafsson, N.; Culley, S.; Ashdown, G.; Owen, D. M.; Pereira, P. M.; Henriques, R. Fast live-cell conventional fluorophore nanoscopy with ImageJ through super-resolution radial fluctuations. *Nature Communications* **2016**, *7* (1), 12471. DOI: 10.1038/ncomms12471.
(23) Drummen, G. P. C.; van Liebergen, L. C. M.; Op den Kamp, J. A. F.; Post, J. A. C11-BODIPY581/591, an oxidation-sensitive fluorescent lipid peroxidation probe: (micro)spectroscopic characterization and validation of methodology. *Free Radical Biology and Medicine* **2002**, *33* (4), 473-490. DOI: https://doi.org/10.1016/S0891-5849(02)00848-1.
(24) Dixon, Scott J.; Lemberg, Kathryn M.; Lamprecht, Michael R.; Skouta, R.; Zaitsev, Eleina M.; Gleason, Caroline E.; Patel, Darpan N.; Bauer, Andras J.; Cantley, Alexandra M.; Yang, Wan S.; et al. Ferroptosis: An Iron-Dependent Form of Nonapoptotic Cell Death. *Cell* **2012**, *149* (5), 1060-1072. DOI: https://doi.org/10.1016/j.cell.2012.03.042.
(25) Shah, R.; Farmer, L. A.; Zilka, O.; Van Kessel, A. T. M.; Pratt, D. A. Beyond DPPH: Use of Fluorescence-Enabled Inhibited Autoxidation to Predict Oxidative Cell Death Rescue. *Cell Chem Biol* **2019**, *26* (11), 1594-1607.e1597. DOI: 10.1016/j.chembiol.2019.09.007 From NLM.
(26) Pedrera, L.; Espiritu, R. A.; Ros, U.; Weber, J.; Schmitt, A.; Stroh, J.; Hailfinger, S.; von Karstedt, S.; García-Sáez, A. J. Ferroptotic pores induce Ca(2+) fluxes and ESCRT-III activation to modulate cell death kinetics. *Cell Death Differ* **2021**, *28* (5), 1644-1657. DOI: 10.1038/s41418-020-00691-x From NLM.
(27) Bacellar, I. O. L.; Oliveira, M. C.; Dantas, L. S.; Costa, E. B.; Junqueira, H. C.; Martins, W. K.; Durantini, A. M.; Cosa, G.; Di Mascio, P.; Wainwright, M.; et al. Photosensitized Membrane Permeabilization Requires Contact-Dependent Reactions between Photosensitizer and Lipids. *Journal of the American Chemical Society* **2018**, *140* (30), 9606-9615. DOI: 10.1021/jacs.8b05014.
(28) Bailey, Andrew P.; Koster, G.; Guillermier, C.; Hirst, Elizabeth M. A.; MacRae, James I.; Lechene, Claude P.; Postle, Anthony D.; Gould, Alex P. Antioxidant Role for Lipid Droplets in a Stem Cell Niche of Drosophila. *Cell* **2015**, *163* (2), 340-353. DOI: 10.1016/j.cell.2015.09.020 (acccessed 2023/09/02).
(29) Schindelin, J.; Arganda-Carreras, I.; Frise, E.; Kaynig, V.; Longair, M.; Pietzsch, T.; Preibisch, S.; Rueden, C.; Saalfeld, S.; Schmid, B.; et al. Fiji: an open-source platform for biological-image analysis. *Nature Methods* **2012**, *9* (7), 676-682. DOI: 10.1038/nmeth.2019.
(30) Foret, M. K.; Do Carmo, S.; Lincoln, R.; Greene, L. E.; Zhang, W.; Cuello, A. C.; Cosa, G. Effect of antioxidant supplements on lipid peroxidation levels in primary cortical neuron cultures. *Free Radical Biology and Medicine* **2019**, *130*, 471-477. DOI: https://doi.org/10.1016/j.freeradbiomed.2018.11.019.

(31) Lincoln, R.; Greene, L. E.; Zhang, W.; Louisia, S.; Cosa, G. Mitochondria Alkylation and Cellular Trafficking Mapped with a Lipophilic BODIPY–Acrolein Fluorogenic Probe. *Journal of the American Chemical Society* **2017**, *139* (45), 16273-16281. DOI: 10.1021/jacs.7b08615.
(32) Gavet, O.; Pines, J. Progressive activation of CyclinB1-Cdk1 coordinates entry to mitosis. *Dev Cell* **2010**, *18* (4), 533-543. DOI: 10.1016/j.devcel.2010.02.013 From NLM.
(33) Griffith, O. W.; Meister, A. Potent and specific inhibition of glutathione synthesis by buthionine sulfoximine (Sn-butyl homocysteine sulfoximine). *Journal of Biological Chemistry* **1979**, *254* (16), 7558-7560.

Chapter 3: Sensing Lipid Peroxidation *in vitro* Through Fluorescence Coupled to Chemical Amplification

Zhang, W.; McCain, J.; Bresoli-Obach, R.; Nonell, S.; Cosa, G.; *To be submitted*

3.1 Preface:

In **Chapter 2** we utilized our arsenal of targeted fluorogenic probes to monitor the spatiotemporal formation of lipid peroxyl radicals in ferroptosis, unraveling some fundamental underpinnings of the process. However, the desire for increased sensitivity in identifying the initial sites of lipid peroxidation still remains. In this chapter, we use probe autocatalysis to find sites vulnerable to ROS damage.

Here, we demonstrate the utility of the dormant singlet oxygen photosensitizer H_3BrB-PMHC to simultaneously report on and generate ROS. The probe was conceived bearing juxtaposed antioxidant (chromanol) activity as the probes described in **Chapter 2**, and prooxidant antagonistic chemical activity through the substitution of the BODIPY core with heavy atoms (Br-BODIPY), enabling the autocatalytic, and in general ROS-mediated, activation of the probe. H_3BrB-PMHC was further designed to yield equal proportions of fluorescence and singlet oxygen sensitization quantum yields. The autocatalytic paradigm arising from the juxtaposed antioxidant-prooxidant moieties build in H_3BrB-PMHC was reported previously by our group in a first-generation dormant photosensitizer and recently exploited in bacteria cells. Here we exploit the autocatalytic properties of H_3BrB-PMHC to observe sites of ROS generation with enhanced sensitivity and to achieve efficient photodynamic inactivation in a spatially confined manner. Thus, using high-speed, high-power imaging, we exploit the autocatalytic nature of the probe to examine regions of high ROS sensitivity, which we identify as lipid droplets – the sites of PUFA storage. We conclude with an outlook towards combining H_3BrB-PMHC in ferroptosis, toward achieving a synergy between ferroptosis induction and PDT, as well as sensing the initial sites of lipid peroxidation in ferroptotic cells.

This work, to be submitted as a manuscript, was prepared in cooperation with Julia McCain and Roger Bresoli-Obach.

3.2 Abstract:

The concentration of reactive oxygen species (ROS) in cells is tightly controlled as part of their homeostasis, where elevated ROS levels leads to oxidative stress. The destructive potential of ROS can, however, be harnessed in therapeutics for the treatment of diseases, as exemplified with the use of photodynamic therapy (PDT) in cancer treatment. Present in low concentrations and typically characterized by their short lifetimes, the sensitive and accurate detection of different ROS is of the utmost interest in furthering our understanding of metabolism and disease states. Here, we introduce H_3BrB-PMHC, a dormant fluorogenic photosensitizer bearing a juxtaposed antioxidant (chromanol) and prooxidant (Br-BODIPY) antagonistic chemical activities, to study lipid peroxyl radical generation and achieve PDT in a controlled manner in cells undergoing high levels of ROS production. H_3BrB-PMHC is deactivated through an intramolecular photoinduced electron transfer pathway. Probe activation takes place in the presence of either lipid peroxyl or alkoxyl free radicals, becoming highly emissive while also generating singlet oxygen (a ROS typically generated in PDT), with both processes taking place with comparable quantum yields. Notably, controlled singlet oxygen release by activated H_3BrB-PMHC can go on to activate more probes, leading to signal amplification through an autocatalytic chemical process. Here we demonstrate the potential of H_3BrB-PMHC as a sensor of initial sites of ROS production, exploiting the enhanced sensitivity rendered from the chemical and fluorescence amplification. We also illustrate the potential of H_3BrB-PMHC as a PDT agent with high spatiotemporal specificity in cell inactivation. Through high-speed imaging we unveil a sequential intracellular activation pattern and identify ROS-responsive regions where lipid droplets first, followed by mitochondria and ER, are observed to sequentially undergo ROS generation. Finally, we probe the compatibility of H_3BrB-PMHC with ferroptosis, with an eye on synergistic uses of photodynamic therapy with ferroptosis induction. Taken together, our results demonstrate a versatile platform by which one probe can have two uses – instigating cell death and investigating its causes.

3.3 Introduction:

Reactive oxygen species (ROS) play a central role in many aspects of cell function.[1] Elevation of ROS levels above a basal concentration required for cell signaling and homeostasis is called oxidative stress and contributes to numerous pathologies, such as cancer,[2] neurodegeneration,[3] and inflammation.[4] As such, the quantification and localization of ROS in biological systems is integral in forming better understandings of disease pathologies, along with more accurate diagnoses of disease progression.

The harmful potential of ROS can, on the other hand, be harnessed as therapy for the amelioration of diseases. Photodynamic therapy (PDT) has been a technique utilized since antiquity,[5] exploiting oxygen, light, and a photosensitizer – a compound that can produce ROS upon irradiation with the appropriate wavelength – to spatiotemporally control the delivery of ROS to ablate unhealthy cells/tissues.[6, 7] As ROS, such as singlet oxygen – the most commonly utilized mechanism of cytotoxicity in (type II) PDT[6] – are non-specifically reactive,[8] their delivery must be tightly controlled to avoid unwanted off-target effects. In the context of PDT, layers of control include the delivery of light as well as selective uptake of the photosensitizer by diseased cells.[7] An additional layer of control in ROS production, such as a chemical cue, would be desirable to mitigate damage to healthy tissue.

Recently, our group introduced the concept of a dormant photosensitizer (DoPS)[9] to selectively inactivate cells with elevated levels of ROS – a hallmark of many disease states.[1, 10] The 1st generation dormant photosensitizer Br_2B-PMHC is based on the design of a fluorogenic radical trapping antioxidant (RTA) probe,[11] where the excited state of the chromophore segment in the probe is quenched by photoinduced electron transfer (P*e*T) from the RTA segment.[11] The probe, being non-emissive in its reduced form, readily becomes emissive upon the oxidation of its RTA moiety upon scavenging e.g. lipid peroxyl radicals, abolishing PeT and restoring fluorescence. Here, the substitution of bromine atoms in

the BODIPY chromophore converts the probe into an efficient photosensitizer via the heavy atom effect.[12] This concept of DoPS was previously applied by our group in the selective inactivation of bacteria.[9] Building off the design principle of DoPS, our group recently reported the 2nd generation DoPS – H_3BrB-PMHC (**Scheme 3.1**).[13] Utilizing the fluorogenic lipid peroxidation probe backbone developed by Greene and coworkers,[14] the detection sensitivity of the probe was greatly improved. Here, the substitution by one bromine atom - compared to the two present in the 1st generation DoPS design - afforded a special advantage, namely the fluorescence quantum yield is retained and perfectly balanced with photosensitization where both processes occur with quantum yields close to 0.5. This allows for the real-time observation of probe activation and subsequent photosensitization. Additionally, as probe activation begets more probe activation, the potential for signal amplification means more sensitive detection could potentially be achieved.

Here, we demonstrate the utility of the DoPS compound H_3BrB-PMHC in its dual usage as both a photosensitizer and an autocatalytic probe of lipid peroxidation. We show in bulk microscopy studies that upon irradiation, H_3BrB-PMHC acts as a photosensitizer, showing spatially localized inactivation of cancer cells (with heightened metabolism and ROS levels) upon irradiation with light. Through high magnification microscopy, we show that vesicles of high intensity are the predominant features in the first few frames of imaging, indicative of a high degree of probe activation. Following that, the characteristic morphological structures of mitochondria are visible, and finally the ER/Golgi mass, highlighting what we posit are ROS-sensitive regions of cells.

We next explore the use of H_3BrB-PMHC toward studying ferroptosis and toward exploring a two-pronged therapy to control cell proliferation via ferroptosis and PDT. Ferroptosis[15] is a form of cell death characterized by uncontrollable lipid peroxidation that has captured the attention of the oxidative stress biology community due to its plethora of ways in regulating ROS production,[16] tipping the scale from homeostasis towards cell death. Many small molecule inducers of ferroptotic cell death have been

investigated for their potential as anti-cancer drugs.[17, 18] When using H_3BrB-PMHC in tandem with the ferroptosis inducer RSL3, we notice a slight synergy in PDT activity with ferroptosis along with the preferential oxidation of lipid droplets during the initial onset of ferroptosis.

Taken together, we demonstrate a potent probe with potential applications for theragnostics – exposing and inactivating regions of elevated ROS concentration.

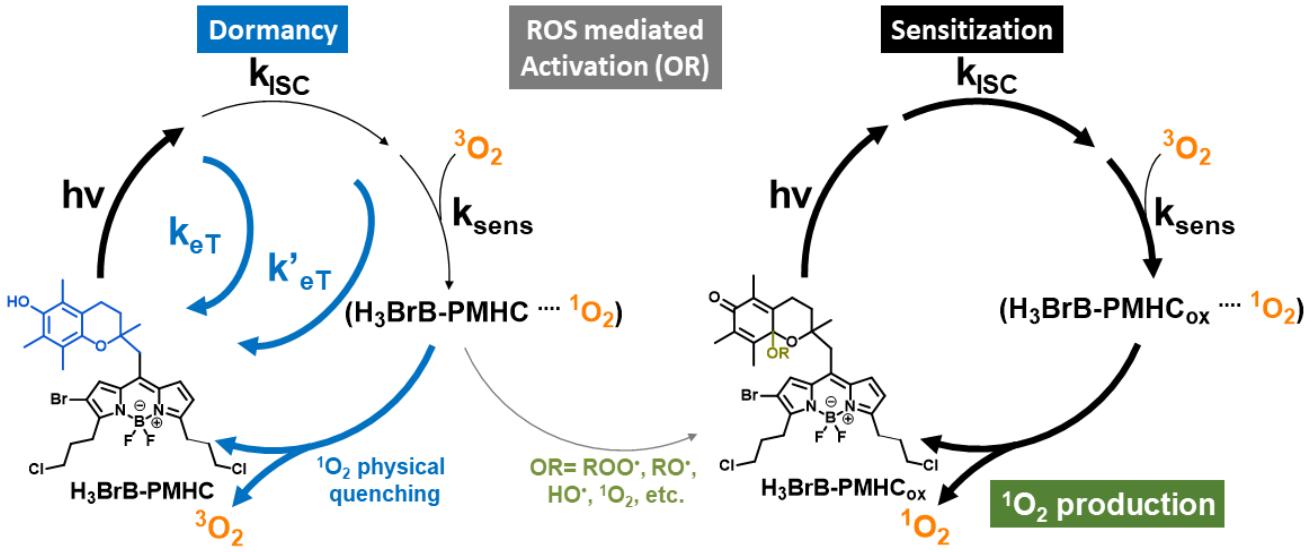

Scheme 3.1: Mode of action of H_3BrB-PMHC.

3.4 Results and discussion:

3.4.1 H_3BrB-PMHC balances fluorescence and singlet oxygen generation

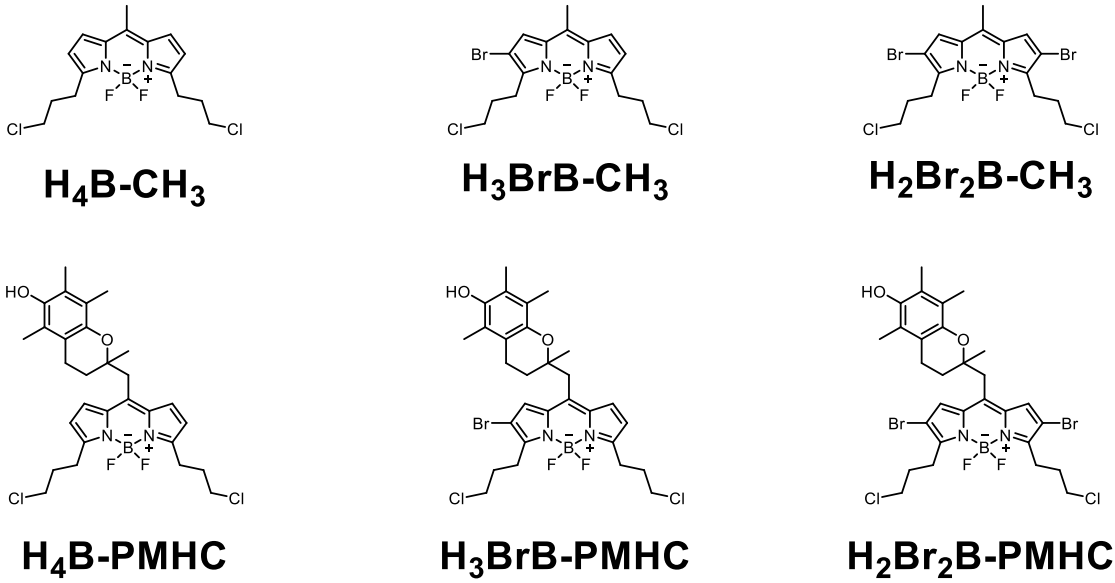

Figure 3.1 Structures of tocopherol-bearing fluorogenic probes H_4B-PMHC, H_3BrB-PMHC, H_2Br_2B-PMHC and their corresponding control compounds

The full synthetic details of H_3BrB-PMHC and other tocopherol-bearing fluorogenic probes have been reported by our group in previous publications,[13, 14] with the photophysical characterisations summarized in **Table 3.1** (see **Fig. 3.1** for structures). The general design principle of heavy atom substitution to facilitate intersystem crossing for singlet oxygen sensitization has been well established in the field[7] and previously reported by our group.[9]

Using the H_4B-PMHC backbone (**Fig. 3.1**), the mono-substitution of bromine was chosen over di-substitution to balance fluorescence and singlet oxygen quantum yields. All PMHC-bearing probes demonstrate dormancy due to PeT, as shown by the extremely low fluorescence quantum yields (ϕ_{fl}). To quantify singlet oxygen quantum yields (ϕ_{Δ}), always-on fluorescent control compounds were used for quantitation, substituting the PMHC moiety for a methyl and abolishing PeT. The substitution of two bromines in the BODIPY core results in a significantly decreased fluorescence quantum yield compared

to one substitution (0.48 to 0.35 in going from H_3BrB-CH_3 to H_2Br_2B-CH_3), with negligible gains in singlet oxygen sensitization (0.48 to 0.51 in going from H_3BrB-CH_3 to H_2Br_2B-CH_3).

Table 3.1: spectroscopic properties of chromanol-bearing fluorogenic probes H_4B-PMHC, H_3BrB-PMHC, H_2Br_2B-PMHC and their corresponding control compounds.

	λ_{abs} (nm)	λ_{em} (nm)	ε ($\times 10^3\ M^{-1}\ cm^{-1}$)	ϕ_{fl}	ϕ_{Δ}
H_4B-PMHC	509	533	82	0.001	-
H_3BrB-PMHC	520	533	60	0.0007	-
H_2Br_2B-PMHC	537	551	73	0.001	-
H_4B-CH_3	502	516	79	0.94	-
H_3BrB-CH_3	513	525	56	0.48	0.48
H_2Br_2B-CH_3	529	544	60	0.35	0.51

3.4.2 H_3BrB-PMHC Effectively Induces Cell Death with Light Exposure

We tested the efficacy of H_3BrB-PMHC as a PDT agent by demonstrating light-induced cell death with HeLa cells (**Fig. 3.2**). Fluorescence microscopy was employed to accomplish the dual role of light dosing and monitoring cells.

To gauge the delivery of H_3BrB-PMHC into cells, we initially examined the intensity of an analogous always-fluorescent control compound (H_3BrB-CH_3), lacking the PMHC mediated intramolecular PeT quenching mechanism, as it partitions into cells. In imaging conditions, when H_3BrB-CH_3 was delivered into cells in Live Cell Imaging Solution (LCIS) in 0.33% DMSO (vehicle), it was found that a plateau of fluorescence intensity was achieved at approximately 15 minutes. Upon exchange of the buffer solution, it was found that fluorescence intensity dropped slightly due to the removal of free dye from solution, of which a plateau occurred in approximately 15 minutes as well (**Fig. S3.1**). This established our imaging conditions to maximize signal-to-background for imaging.

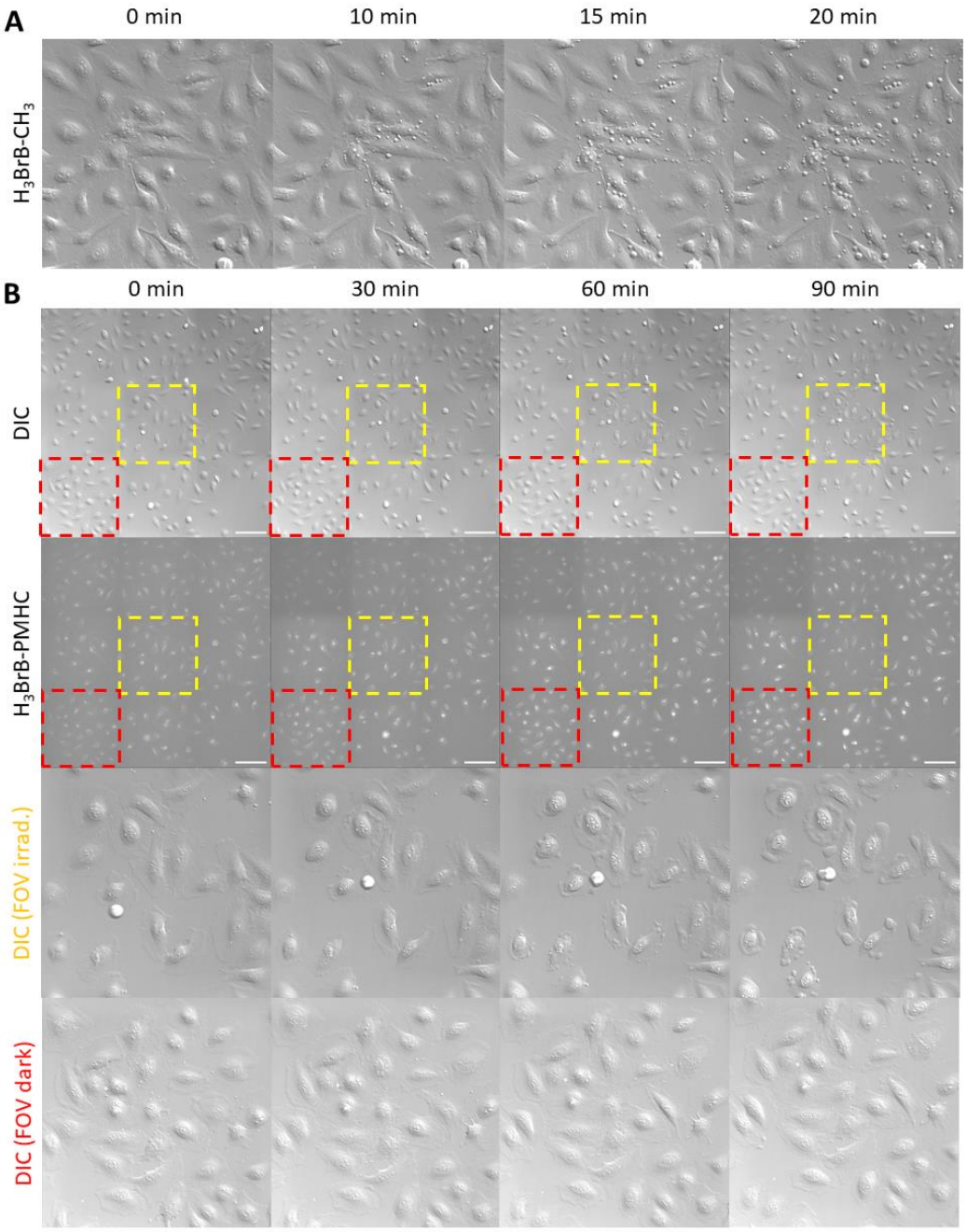

Figure 3.2: Dormant photosensitizer demonstrating spatially controlled cell killing A) HeLa cells with 100 nM control (always active) $H_3BrB\text{-}CH_3$, incubated for 10 min in LCIS prior to media exchange, irradiated continuously at 0.5 mW laser power (488 nm, 5 W/cm^2) for 20 minutes, with observable blebbing by 10 minutes. B) HeLa cells with 100 nM DoPS H_3BrB-PMHC (dormant photosensitizer), incubated for 10 min in LCIS prior to media exchange, irradiated continuously at 0.5 mW laser power (488 nm, 5 W/cm^2) for 90 minutes. Images were captured by widefield microscopy at 20x magnification, along with neighbouring fields of view adjacent to the irradiated FOV and stitched together. Brightfield DIC images are displayed in the first row showing cell morphology. The second row shows the DIC overlaid with fluorescence of the same region. Dashed boxes highlight the region of irradiation (yellow) along with neighbouring FOV (red). Third and fourth rows display the expanded irradiated and non-irradiated regions for ease of viewing. Scale bar = 150 µm.

After establishing conditions to deliver H_3BrB-PMHC into cells, we next examined photoinactivation. We irradiated HeLa cells continuously after treatment with the probe, and captured brightfield differential inference contrast (DIC) and fluorescence images of the field of view (FOV) of irradiation along with its neighbouring FOVs to examine the area of effect of photoinactivation. First, to gauge singlet oxygen generation in the absence of a deactivation mechanism (always active compounds), we monitored the control compound H_3BrB-CH_3, which does not require activation by oxidation prior to photosensitization upon light exposure. Upon constant irradiation with H_3BrB-CH_3, cell membrane blebbing – a characteristic morphology in apoptotic cell death[19] – is recorded in as early as 10 minutes following the start of the irradiation (**Fig. 3.2A**). Next, we examined H_3BrB-PMHC. Within the region of irradiation (**Fig. 3.2B**), cell membrane blebbing is much more attenuated and controlled, becoming apparent only after 30 minutes, where within the window of observation it appears to be highly spatially localized to the region of irradiation only. The initial activation of the probe is due to the basal level of endogenous metabolic ROS production, we reason, which next results in autocatalytic activation, thus resulting in delayed photoinactivation in contrast to the speed at which control compound H_3BrB-CH_3 inactivates cells under otherwise identical conditions. We monitored the fluorescence intensity, a measure of probe activation, of H_3BrB-PMHC in cells with light irradiation by measuring the corrected total cell fluorescence intensity (CTCF). The CTCF of H_3BrB-PMHC undergoes an approximately two-fold enhancement with light irradiation. Under identical conditions, the signal intensity of the fluorogenic (non-photosensitizing) RTA H_4B-PMHC remains constant (**Fig. 3.3**). While the signal intensity change of H_3BrB-PMHC is consistent with the mechanism of action (initial activation upon ROS scavenging), it is important to comment on the lower signal intensity of H_3BrB-PMHC in comparison to H_4B-PMHC (control). This is attributed to the lower fluorescence quantum yield of H_3BrB-PMHC, due to the addition of the heavy atom and increased triplet quantum yield. It is also consistent with a lower overall absorption extinction coefficient (see **Table 3.1**) for H_3BrB-PMHC vs its fluorogenic

RTA analogue H_4B-PMHC, and the red-shifted absorption spectrum of the former resulting from the incorporation of the Br atom to the BODIPY chromophore. Combined, the bathochromic shift and lower overall extinction coefficient result in reduced absorption at 488 nm, the laser excitation used herein. We previously reported H_4B-PMHC, the fluorogenic but non-photosensitizing control, to measure basal ROS metabolism[14] via its fluorescence enhancement. Notably, under the conditions used for photoinactivation – continuous light irradiation – H_4B-PMHC showed negligible fluorescence enhancement over time. This is likely due to minimal probe activation (by metabolic ROS), contrary to H_3BrB-PMHC, where autocatalysis amplifies the initial ROS production. Activation of H_3BrB-PMHC leads to the production of $^1O_2$, which result in the formation of lipid hydroperoxides and further activation of H_3BrB-PMHC. That no larger enhancement of H_3BrB-PMHC was observed is consistent with the rate of enhancement being approximately equal to the rate of photobleaching for this probe under our experimental conditions, accounting for the drop in intensity after ~ 30 min of irradiation (**Fig 3.3**. right panel). As dye photobleaching is a function of intersystem crossing/population of the triplet excited state, the faster rate of photobleaching for the DoPS H_3BrB-PMHC versus H_4B-PMHC is not surprising.

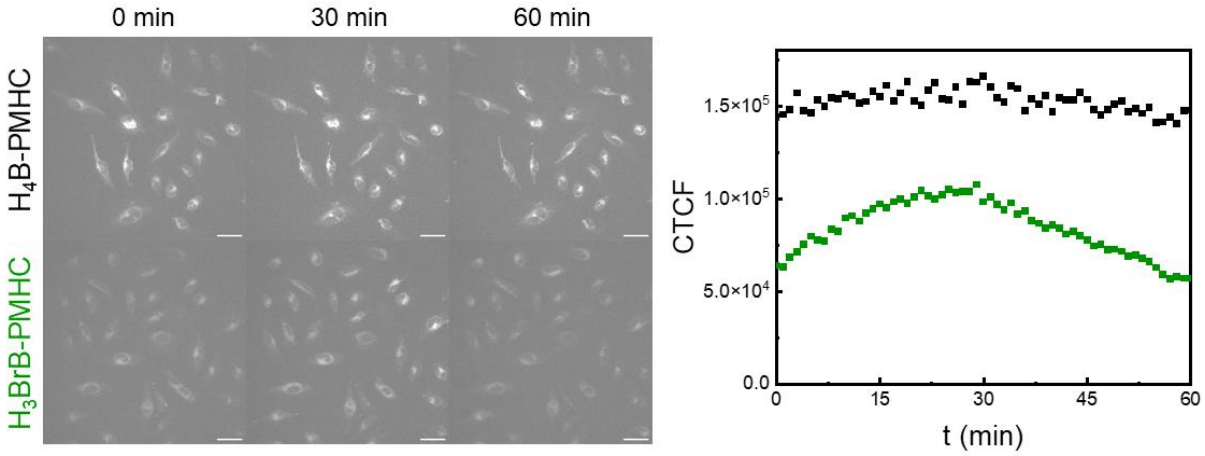

Figure 3.3: CTCF of HeLa cells with 100 nM photosensitizing H_3BrB-PMHC (green) and non-photosensitizing H_4B-PMHC (black), irradiated continuously at 0.5 mW laser power (488 nm). Scale bar = 50 µm.

3.4.3 H_3BrB-PMHC as an Imaging Agent Reveals ROS Sensitive Regions within Cells

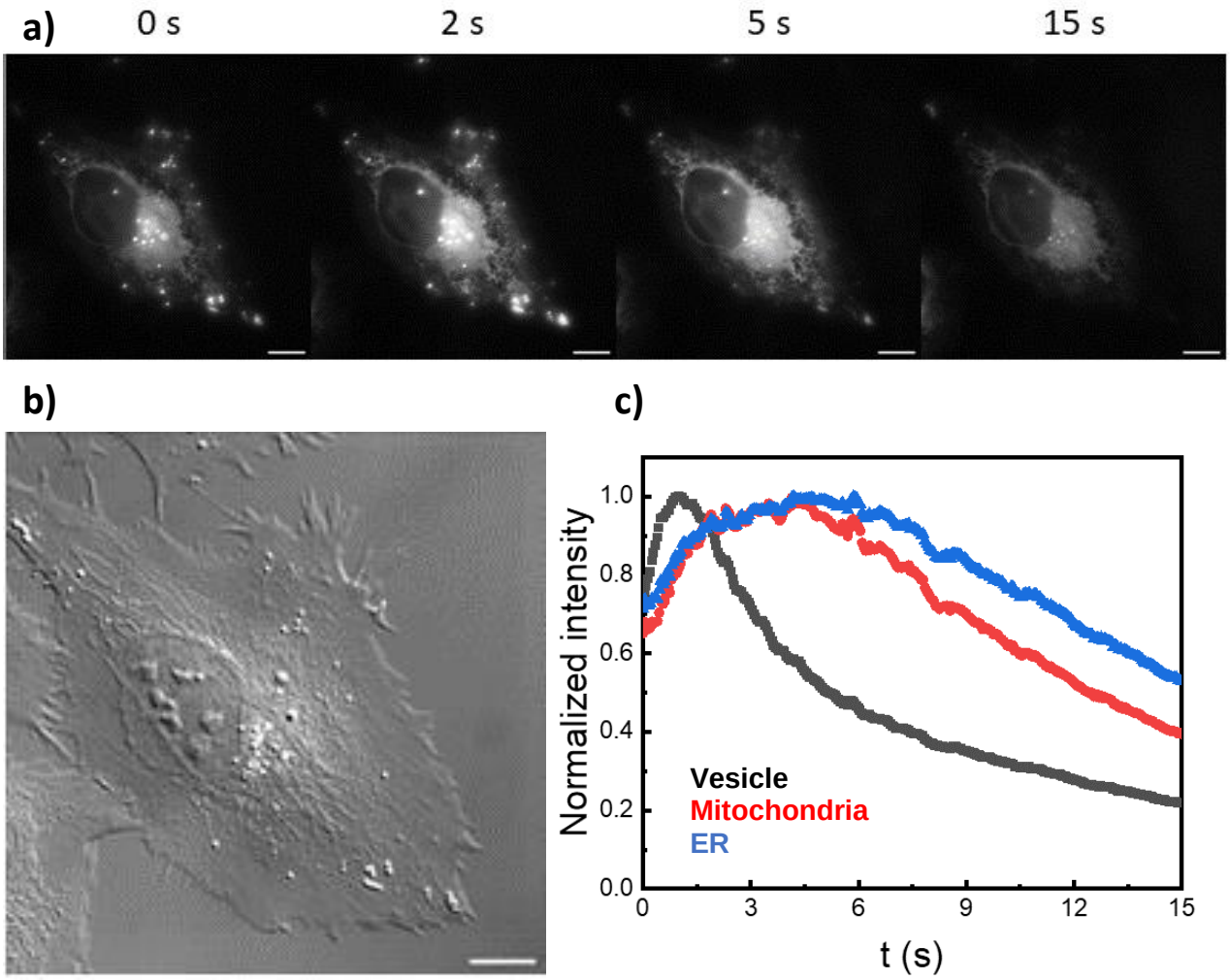

Figure 3.4: a) High speed imaging of 100 nM H_3BrB-PMHC in a single HeLa cell. Fast time stacks (50 ms exposure) were collected continuously. Images were collected at 100x in TIRF modality (1 mW 488 nm laser). Scale bar = 10 µm. b) DIC image of cell. c) enhancement in various subcellular locations: vesicle structure (black), mitochondria (red), ER (blue). ROIs selected by morphology segmentation (**Section 3.6.6**)

To interrogate intracellular dynamics, we next exploited the autocatalytic nature of our probe, under high-speed imaging (50 ms exposure). We reasoned that at high light dosage/laser power, faster probe activation will occur due to autocatalysis, enabling the visualization of the earliest formed radical species or areas of increased ROS production to be amplified. Consequently, at high laser power, a faster acquisition speed could be utilized due to the heightened fluorescence intensity increase with time. In

fast, high magnification (100x) timelapses of cells treated with H_3BrB-PMHC (**Fig. 3.4**), we observed a sequential activation of the probe in various organelles of the cell. High intensity punctate structures are the predominately featured in the first few frames of imaging. Following that, the characteristic morphological structures of mitochondria are appear, and finally the ER/Golgi mass. We quantified the fluorescence enhancements of these key features at various timepoints based on morphology segmentation (**Section 3.6.6**).

3.4.4 Characterisation of ROS Sensitive Vesicles

Our initial suspicion regarding the observation of vesicle/punctate structures are that they correspond to stress granules – structures typically formed during oxidative stress. Here, liquid-liquid phase separation drives the formation of many granule-like structures in cells, commonly termed as membrane-less organelles, driving a wide variety of biological functions.[20] Stress granules, RNA-protein assemblages, are sites of stalled translation within the cell cytoplasm in which heat-shock and other stress response proteins aggregate around mRNA and the translational machinery as a protective mechanism against cell stress.[21, 22]

To test for the hypothesis that stress granules are originally involved in H_3BrB-PMHC activation, we resorted to a bona fide method of generating stress granules using arsenite.[23] In mammalian cells, it has been shown that sub-millimolar concentrations of $NaAsO_2$ can induce stress granule assembly on the scale of minutes from exposure, observed through the fluorescent labeling of canonical proteins involved in stress granule assembly.[21-23] Cells treated with the non-photosensitizing fluorogenic RTA probe H_4B-PMHC, when exposed to arsenite stress, displayed an overall increase in ROS levels relative to basal metabolism, as seen in the non-specific enhancement of fluorescence in all cellular structures and membranes (**Fig. 3.5**). However, no aggregation and formation of granule-like structures was observed, indicating stress granules not to be a culprit of the observed hotspots of H_3BrB-PMHC fluorescence.

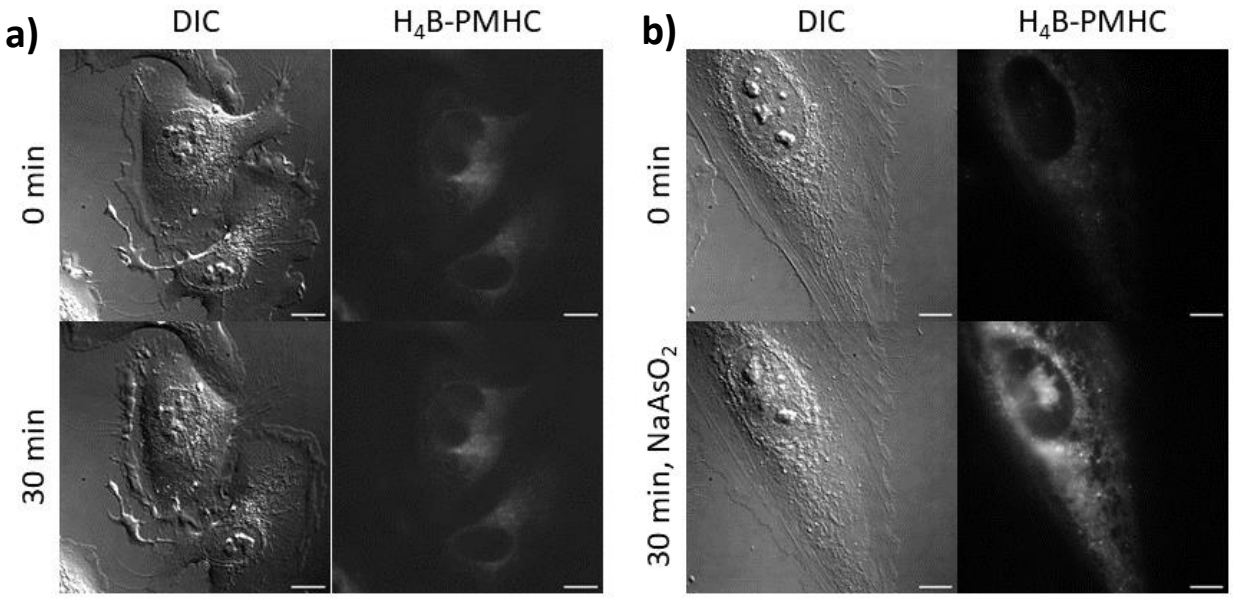

Figure 3.5: Impact of arsenite stress on cells a) HeLa cell with 100 nM H_4B-PMHC incubated in LCIS for 10 min prior to media exchange, imaged for 30 min. b) HeLa cell with 100 nM H_4B-PMHC incubated in LCIS for 10 min prior to media exchange, treated with $NaAsO_2$ (0.5mM , 30min). Scale bars = 10 μm.

We next investigated lipid droplets as the site where enhanced oxidative stress is recorded via monitoring H_3BrB-PMHC activation. Lipid droplets are the site of neutral lipid storage.[24] Composed of a single phospholipid bilayer shell and a core packed with triglycerides, lipid droplets play a critical role in the mediation of lipid metabolism,[24] serving as the intermediary of many building materials. To induce lipid droplet formation, we starved cells in buffer solution, inducing autophagy – the breakdown lipid products that will eventually become stored in lipid droplets. It was reported by Nguyen and colleagues that lipid droplet biogenesis can be regulated by the activity of diacylglycerol acyltransferase 1 and 2 (DGAT1/2), which are enzymes along the lipid assembly pathway, where lipid droplet assembly is critically impaired with DGAT1/2 inhibition.[25] We monitored H_3BrB-PMHC intensity in imaging studies concomitant with the induction and inhibition of lipid droplet formation via starvation and DGAT1/2 inhibition (**Fig. 3.6**). H_3BrB-PMHC intensity, a marker of oxidation, correlated with conditions inducing formation of the vesicle structures, supporting that these structures are primarily visualizing lipid droplets as the first sites of activation in high power time course imaging.

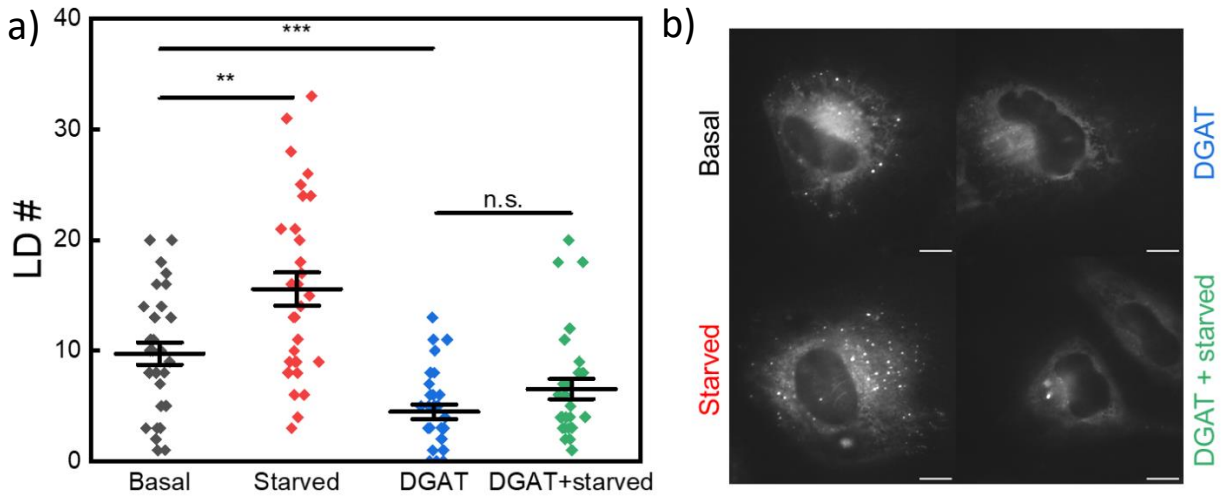

Figure 3.6: a) Lipid droplet count in HeLa cells at various conditions, monitored upon H_3BrB-PMHC activation, and b) representative images. HeLa cells treated with DGAT-1/2 inhibitors (20 µM T863 20 + 10 µM PF-06424439, 6hr) and/or starved (PBS, 3hr). N=30, bars = mean +/- 1 SEM. Asterisk indicates significance by t-test, ** $p < 0.01$ and *** = $p < 0.001$. Scale bars on images = 12 µm.

It has previously been reported by Bailey and colleagues in a drosophila model that oxidative stress induces the formation of lipid droplets in neuronal cells.[26] Via lipid peroxidation measurements, it was found that lipid droplets experienced a lower degree of oxidation than cellular membranes despite being packed with easily oxidizable unsaturated fatty acids. A physical sequestration mechanism was proposed, suggesting that vulnerable lipid building materials are shuttled into lipid droplets and away from oxidative stress.

The BODIPY core of the probe is highly lipophilic and often used as the backbone of lipid membrane stains.[27] Naturally, H_3BrB-PMHC should partition into regions of high lipophilicity such as lipid droplets. However, in comparison to mitochondria for example, lipid droplets are not sites of high enzymatic activity which can generate ROS and activate H_3BrB-PMHC. We suggest that the reason for heightened sensitivity of lipid droplets to H_3BrB-PMHC may be partly due to spatial confinement, where a single ROS-mediated activation event would be required to trigger the rest via photoinduced singlet oxygen generation from H_3BrB-PMHC$_{ox}$, in a small organelle in which there is a relatively higher probe concentration than elsewhere.

3.4.5 Potential promising application for synergy with ferroptosis induction

Having characterized the potential of H_3BrB-PMHC as a sensor we next explored the possibility of synergizing the effects of our dormant photosensitizer with ferroptosis – cell death via excess lipid peroxyl radical generation and associated lipid peroxidation.[15] We reasoned that the autocatalytic properties of the antioxidant/prooxidant compound H_3BrB-PMHC could be used in tandem with ferroptosis inducers – currently explored as potential therapeutics for cancers[17, 28] – to amplify their mechanism of action: exacerbating oxidative stress in sites already undergoing lipid peroxidation. For this purpose, we employed a bulk assay consisting of an LED light array for PDT studies under exposure to ferroptosis inducers and assessed cell viability with the resazurin assay (**Fig. 3.7**). We found that with light irradiation, a slight decrease in the EC50 of the ferroptosis inducer RSL3 is observed (279 to 202 nM), however the sampling in the region of interest is low enough that makes the difference not significant. A parallel must be drawn however between these PDT results and those from the microscope (**Fig. 3.2**), in that the light array for PDT here is orders of magnitude lower in power – 2.6 mW/cm^2 compared to 5 W/cm^2. Higher light dosage could accentuate the EC50 differences.

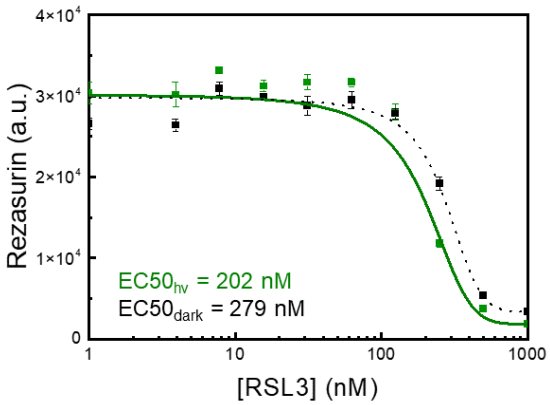

Figure 3.7: Cell viability of HT-1080 cells treated with dormant photosensitizer H_3BrB-PMHC, with (green) and without (black) light exposure. Dilution series (0-1000 nM) of ferroptosis inducer RSL3 in HT-1080 cells with 100 nM H_3BrB-PMHC were incubated for 1.5hr and then irradiated with light (2.6 mW/cm^2, peak wavelength at 520 nm) for 30 min. The cells were then incubated for 24 hours and developed with resazurin for a further 2 hr prior to viability measurement. Bars = SEM.

3.4.6 Autocatalysis as a mechanism for increased detection sensitivity:

The self-amplification mechanism of H_3BrB-PMHC stands to be of great utility for the observation of sensitive lipid peroxidation events. Of particular interest is the onset of lipid peroxidation in ferroptosis. While the field has shown remarkable growth in the 20 years since its inception, fundamental questions remain to be answered,[29] such as the primary/first sites of lipid peroxidation and the contributions of various organelles in the onset of ferroptosis. Recent works by Stockwell and colleagues as well as ourselves (**Chapter 2**) have pointed to the ER as the key organelle involved in the induction of ferroptosis.[30] Notably, increased sensitivity in the probes used could play a big role in elucidating the exact spatiotemporal aspects of lipid peroxidation induction.

To provide insights into the localization of lipid peroxidation earlier in the ferroptosis progression, we next explored imaging with H_3BrB-PMHC, reasoning that data acquisition in quick bursts at different stages of the ferroptosis progression would shed light on foci of ROS generation (**Fig. 3.8**). Similar to results in HeLa cells, imaging with HT1080 cells treated with RSL3 at the earliest stages of ferroptosis induction (10 min, 30 min) displayed punctate structures with lipid droplets being the first structures to be prominently illuminated. Following the course of ferroptosis, the plasma membrane became the dominant feature post-120 min, congruent with the established understanding of ferroptosis with plasma membrane damage as the final morphological feature prior to cell death (**Chapter 2**).[16] These results raise questions of what role lipid droplets play in ferroptosis. While previous works by Stockwell, Min, and Woerpel have shown that the complete ablation of lipid droplets does not prevent ferroptosis upon GPX4 inhibition,[30] these structures remain an untapped pool of oxidizable lipids, perhaps capable of playing a role in alternative pathways of ferroptosis induction.

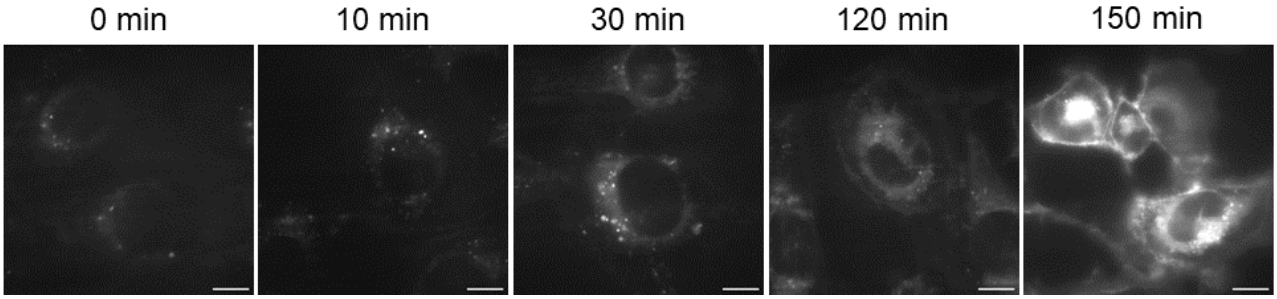

Figure 3.8: Ferroptosis induced (1 µM RSL3) in HT-1080 cells imaged with H_3BrB-PMHC (10 nM in DMEM). Cells were imaged continuously under conditions identical to those in **Fig. 3.4**, to amplify sites of probe activation. Frames taken from time-courses of individual cell acquisitions at various times post RSL3 treatment. Bar = 10 µm.

3.5 Conclusion:

Here we present the second-generation dormant photosensitizer, H_3BrB-PMHC, with its balanced rates of fluorescence emission and intersystem crossing as a dual-purpose probe for ROS sensing and generation of singlet oxygen, a specific ROS involved in lipid peroxidation via the *ene* reaction. With its two layers of control over singlet oxygen generation, the photosensitizer is only active in areas of ROS generation and light dosing displaying high spatial specificity in cell killing. Utilizing high power, fast frame acquisition imaging, we demonstrate an ordered sequence of activation of the probe within cells, highlighting ROS sensitive regions which preferentially oxidizes the probe, which we posit as the sites of PUFA storage. Lastly, utilizing H_3BrB-PMHC in conjunction with ferroptosis, we demonstrate promising avenues for further exploration of synergistic PDT as well as investigation into the early stages of lipid peroxidation in ferroptosis.

3.6 Experimental:

3.6.1 Materials:

Cell culture reagents were purchased through ThermoFisher Scientific. RSL3 and DGAT inhibitors were purchased through Sigma Aldrich. FluoroDish (35mm, FD35) imaging dishes were purchased through World Precision Instruments, Inc. µ-Slide 8 well (ibiTreat, tissue culture treated, cat. no. 80826) chambered coverslips were purchased through Ibidi, USA.

3.6.2 Cell Culture:

HeLa cells (ATCC: CCL-2) were cultured in DMEM with glutamine and sodium pyruvate (Gibco: 11995-065) and supplemented with 10% FBS (Gibco: A31607-02) and 1% penicillin-streptomycin (Gibco: 15140). HT-1080 cells (ATCC CCL-121) were maintained in the same media composition as HeLa cells, except for the additional supplementation of non-essential amino acids (Gibco: 11140050). Cells were maintained at 37 °C and 5% humidified CO_2 in a tissue incubator.

3.6.3 Microscopy:

Images were acquired on a Nikon Eclipse Ti microscope, with brightfield differential interference contrast (DIC), epifluorescence, and total internal reflection fluorescence (TIRF) modalities. The unit was equipped with a Perfect Focus System (PFS) and a motorized filter block turret for multichannel imaging. Cells were maintained at 37 °C and 5% humidified CO_2 with a stage-top incubator (Tokai Hit). Fluorescence excitation (488 nm) was filtered and directed towards the objective using a multiband beam splitter (ZT488/640rpc, Chroma Technology). Emissions were filtered through a ZET488/640m emission filter and then captured using a back illuminated EM-CCD camera (Andor iXon Ultra DU-897).

3.6.4 PDT with ferroptosis:

Cells were seeded at 5000 cells/well and incubated for 24hr. The cells were then co-treated with H_3BrB-PMHC and a dilution series of RSL3 and incubated for 90min in phenol-free DMEM. Afterwards, the plates were then irradiated for 30 minutes using an LED array (EXPO-LED, Luzchem Research, 5×4W tube lamps with peak wavelength at 520 nm and FWHM of 31 nm, output power = 2.6 mW/cm^2) with dark control covered in aluminum foil. Following light treatment, the cells were replaced in media and incubated for 24 hours, prior to addition of resazurin (44 μM) for 2 hours and measured on a place reader. EC50 calculations were performed by fitting a dose response curve in OriginPro 2022.

3.6.5 Cell Imaging:

Cells were seeded one day prior to imaging, 15 000 cells/well in ibidi 8-well slides for widefield experiments and 30 000 cells per dish for TIRF experiments. Widefield fluorescence experiments were performed using a 20× objective (Nikon CFI Plan Apo VC 20×, NA = 0.75, air, DIC). TIRF was imaged utilizing a 100× objective (Nikon CFI SR Apochromat TIRF 100×, NA = 1.49, oil, DIC)

3.6.6 Image Analysis:

Image analysis was performed using FIJI/ImageJ.[31] Quantifications of fluorescence enhancements in cells by corrected total cell fluorescence (CTCF) was previous utilized by our group[14] and adapted from previously published protocol[32]:

$$CTCF = \frac{IntDensity_{totalcellarea} - (total\ cell\ area\ \times BkgFluorescence)}{N_{cells}}$$

Where $IntDensity_{totalcellarea}$ is the integrated intensity of the pixels for all cells in the image, *total cell area* is the number of pixels of all the cells, *BkgFluorescence* is the mean fluorescence intensity per pixel for a region containing no cells and N_{cells} is the number of cells in the image.

Regions of interest (ROI) for vesicle regions were performed by intensity thresholding from the initial frames of the timelapse. Mitochondria, identified morphologically from DIC images, are challenging to segment as many are in close proximity and/or contact with the ER, in addition to spectral crosstalk from MitoTracker (**Fig S3.2**). As such, a manual selection of a region distant from the ER mass was selected. The ER ROI was selected via intensity thresholding of the timelapse at 20s and applied to the full timelapse.

Lipid droplet quantification was performed using the SpotCounter plugin on FIJI, at a noise tolerance of 2000 and box size of 10.

3.7 Supporting Information:

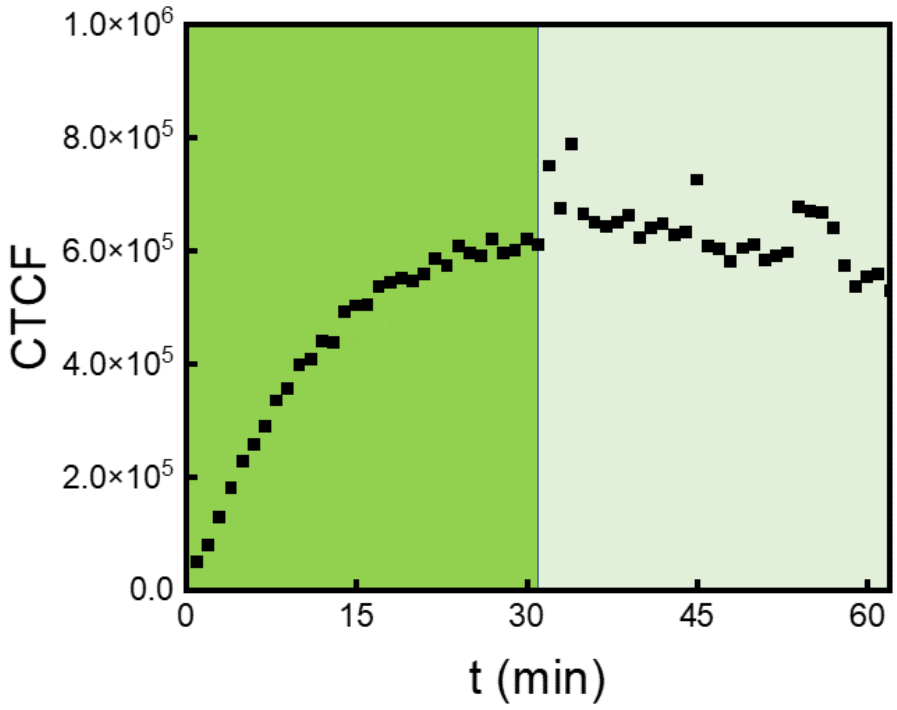

Figure S3.1: Partition in and out of $H_3BrB\text{-}CH_3$. 100 nM of dye was added in LCIS and imaged at 1 frame/min (488 nm, 0.1 mW) for 30 minutes to observe partitioning in of the dye (dark green). The media was then exchanged and imaged again for a further 30 minutes to observe partitioning out of the dye (light green).

3.8 References:

(1) Halliwell, B.; Gutteridge, J. M. C. *Free Radicals in Biology and Medicine*; Oxford University Press, 2015. DOI: 10.1093/acprof:oso/9780198717478.001.0001.
(2) Harris, I. S.; DeNicola, G. M. The Complex Interplay between Antioxidants and ROS in Cancer. *Trends in Cell Biology* **2020**, *30* (6), 440-451. DOI: 10.1016/j.tcb.2020.03.002 (acccessed 2023/08/10).
(3) Zhou, Y.; Zhen, Y.; Wang, G.; Liu, B. Deconvoluting the Complexity of Reactive Oxygen Species (ROS) in Neurodegenerative Diseases. *Frontiers in Neuroanatomy* **2022**, *16*, Mini Review. DOI: 10.3389/fnana.2022.910427.
(4) Chen, Y.; Fang, Z.-M.; Yi, X.; Wei, X.; Jiang, D.-S. The interaction between ferroptosis and inflammatory signaling pathways. *Cell Death & Disease* **2023**, *14* (3), 205.
(5) Hönigsmann, H. History of phototherapy in dermatology. *Photochemical & Photobiological Sciences* **2013**, *12* (1), 16-21. DOI: 10.1039/c2pp25120e.
(6) Dąbrowski, J. M.; Arnaut, L. G. Photodynamic therapy (PDT) of cancer: from local to systemic treatment. *Photochemical & Photobiological Sciences* **2015**, *14* (10), 1765-1780.
(7) Pham, T. C.; Nguyen, V.-N.; Choi, Y.; Lee, S.; Yoon, J. Recent Strategies to Develop Innovative Photosensitizers for Enhanced Photodynamic Therapy. *Chemical Reviews* **2021**, *121* (21), 13454-13619. DOI: 10.1021/acs.chemrev.1c00381.
(8) Sies, H.; Belousov, V. V.; Chandel, N. S.; Davies, M. J.; Jones, D. P.; Mann, G. E.; Murphy, M. P.; Yamamoto, M.; Winterbourn, C. Defining roles of specific reactive oxygen species (ROS) in cell biology and physiology. *Nature Reviews Molecular Cell Biology* **2022**, *23* (7), 499-515. DOI: 10.1038/s41580-022-00456-z.
(9) Durantini, A. M.; Greene, L. E.; Lincoln, R.; Martínez, S. R.; Cosa, G. Reactive Oxygen Species Mediated Activation of a Dormant Singlet Oxygen Photosensitizer: From Autocatalytic Singlet Oxygen Amplification to Chemicontrolled Photodynamic Therapy. *Journal of the American Chemical Society* **2016**, *138* (4), 1215-1225. DOI: 10.1021/jacs.5b10288.
(10) Kawagishi, H.; Finkel, T. Unraveling the Truth About Antioxidants: ROS and disease: finding the right balance. *Nature Medicine* **2014**, *20* (7), 711-713. DOI: 10.1038/nm.3625.
(11) Krumova, K.; Greene, L. E.; Cosa, G. Fluorogenic α-Tocopherol Analogue for Monitoring the Antioxidant Status within the Inner Mitochondrial Membrane of Live Cells. *Journal of the American Chemical Society* **2013**, *135* (45), 17135-17143. DOI: 10.1021/ja408227f.
(12) McGlynn, S.; Daigre, J.; Smith, F. External Heavy‐Atom Spin—Orbital Coupling Effect. IV. Intersystem Crossing. *The Journal of Chemical Physics* **1963**, *39* (3), 675-679.
(13) McCain, J.; Martínez, S. R.; Fungo, F.; Sakaya, A.; Cosa, G. Two-Pronged Dormant Photosensitizer-Antibiotic Bacterial Inactivation: Mechanism, Dosage, and Cellular Evolution Visualized at the Single-Cell Level. *Journal of the American Chemical Society* **2023**. DOI: 10.1021/jacs.3c10034.
(14) Greene, L. E.; Lincoln, R.; Cosa, G. Rate of Lipid Peroxyl Radical Production during Cellular Homeostasis Unraveled via Fluorescence Imaging. *Journal of the American Chemical Society* **2017**, *139* (44), 15801-15811. DOI: 10.1021/jacs.7b08036.
(15) Dixon, S. J.; Lemberg, K. M.; Lamprecht, M. R.; Skouta, R.; Zaitsev, E. M.; Gleason, C. E.; Patel, D. N.; Bauer, A. J.; Cantley, A. M.; Yang, W. S. Ferroptosis: an iron-dependent form of nonapoptotic cell death. *cell* **2012**, *149* (5), 1060-1072.
(16) Dixon, S. J.; Pratt, D. A. Ferroptosis: A flexible constellation of related biochemical mechanisms. *Molecular Cell* **2023**, *83* (7), 1030-1042. DOI: https://doi.org/10.1016/j.molcel.2023.03.005.
(17) Jiang, X.; Stockwell, B. R.; Conrad, M. Ferroptosis: mechanisms, biology and role in disease. *Nature Reviews Molecular Cell Biology* **2021**, *22* (4), 266-282. DOI: 10.1038/s41580-020-00324-8.
(18) Lei, G.; Zhuang, L.; Gan, B. Targeting ferroptosis as a vulnerability in cancer. *Nature Reviews Cancer* **2022**, *22* (7), 381-396. DOI: 10.1038/s41568-022-00459-0.

(19) Galluzzi, L.; Vitale, I.; Aaronson, S. A.; Abrams, J. M.; Adam, D.; Agostinis, P.; Alnemri, E. S.; Altucci, L.; Amelio, I.; Andrews, D. W. Molecular mechanisms of cell death: recommendations of the Nomenclature Committee on Cell Death 2018. *Cell Death & Differentiation* **2018**, *25* (3), 486-541.
(20) Shin, Y.; Brangwynne, C. P. Liquid phase condensation in cell physiology and disease. *Science* **2017**, *357* (6357), eaaf4382. DOI: 10.1126/science.aaf4382.
(21) Wheeler, J. R.; Matheny, T.; Jain, S.; Abrisch, R.; Parker, R. Distinct stages in stress granule assembly and disassembly. *eLife* **2016**, *5*, e18413. DOI: 10.7554/eLife.18413.
(22) Takahashi, M.; Higuchi, M.; Matsuki, H.; Yoshita, M.; Ohsawa, T.; Oie, M.; Fujii, M. Stress Granules Inhibit Apoptosis by Reducing Reactive Oxygen Species Production. *Molecular and Cellular Biology* **2013**, *33* (4), 815-829. DOI: 10.1128/mcb.00763-12.
(23) Kroschwald, S.; Maharana, S.; Mateju, D.; Malinovska, L.; Nüske, E.; Poser, I.; Richter, D.; Alberti, S. Promiscuous interactions and protein disaggregases determine the material state of stress-inducible RNP granules. *eLife* **2015**, *4*, e06807. DOI: 10.7554/eLife.06807.
(24) Olzmann, J. A.; Carvalho, P. Dynamics and functions of lipid droplets. *Nature Reviews Molecular Cell Biology* **2019**, *20* (3), 137-155. DOI: 10.1038/s41580-018-0085-z.
(25) Nguyen, T. B.; Louie, S. M.; Daniele, J. R.; Tran, Q.; Dillin, A.; Zoncu, R.; Nomura, D. K.; Olzmann, J. A. DGAT1-Dependent Lipid Droplet Biogenesis Protects Mitochondrial Function during Starvation-Induced Autophagy. *Developmental Cell* **2017**, *42* (1), 9-21.e25. DOI: https://doi.org/10.1016/j.devcel.2017.06.003.
(26) Bailey, Andrew P.; Koster, G.; Guillermier, C.; Hirst, Elizabeth M. A.; MacRae, James I.; Lechene, Claude P.; Postle, Anthony D.; Gould, Alex P. Antioxidant Role for Lipid Droplets in a Stem Cell Niche of Drosophila. *Cell* **2015**, *163* (2), 340-353. DOI: https://doi.org/10.1016/j.cell.2015.09.020.
(27) Qiu, B.; Simon, M. C. BODIPY 493/503 Staining of Neutral Lipid Droplets for Microscopy and Quantification by Flow Cytometry. *Bio Protoc* **2016**, *6* (17). DOI: 10.21769/BioProtoc.1912 From NLM.
(28) Stockwell, B. R.; Friedmann Angeli, J. P.; Bayir, H.; Bush, A. I.; Conrad, M.; Dixon, S. J.; Fulda, S.; Gascón, S.; Hatzios, S. K.; Kagan, V. E.; et al. Ferroptosis: A Regulated Cell Death Nexus Linking Metabolism, Redox Biology, and Disease. *Cell* **2017**, *171* (2), 273-285. DOI: 10.1016/j.cell.2017.09.021 From NLM.
(29) Feng, H.; Stockwell, B. R. Unsolved mysteries: How does lipid peroxidation cause ferroptosis? *PLOS Biology* **2018**, *16* (5), e2006203. DOI: 10.1371/journal.pbio.2006203.
(30) von Krusenstiern, A. N.; Robson, R. N.; Qian, N.; Qiu, B.; Hu, F.; Reznik, E.; Smith, N.; Zandkarimi, F.; Estes, V. M.; Dupont, M.; et al. Identification of essential sites of lipid peroxidation in ferroptosis. *Nature Chemical Biology* **2023**, *19* (6), 719-730. DOI: 10.1038/s41589-022-01249-3.
(31) Schindelin, J.; Arganda-Carreras, I.; Frise, E.; Kaynig, V.; Longair, M.; Pietzsch, T.; Preibisch, S.; Rueden, C.; Saalfeld, S.; Schmid, B. Fiji: an open-source platform for biological-image analysis. *Nature methods* **2012**, *9* (7), 676.
(32) Gavet, O.; Pines, J. Progressive activation of CyclinB1-Cdk1 coordinates entry to mitosis. *Developmental cell* **2010**, *18* (4), 533-543.

Chapter 4: Chemically Tuned, Reversible Fluorogenic Electrophile for Live Cell Nanoscopy

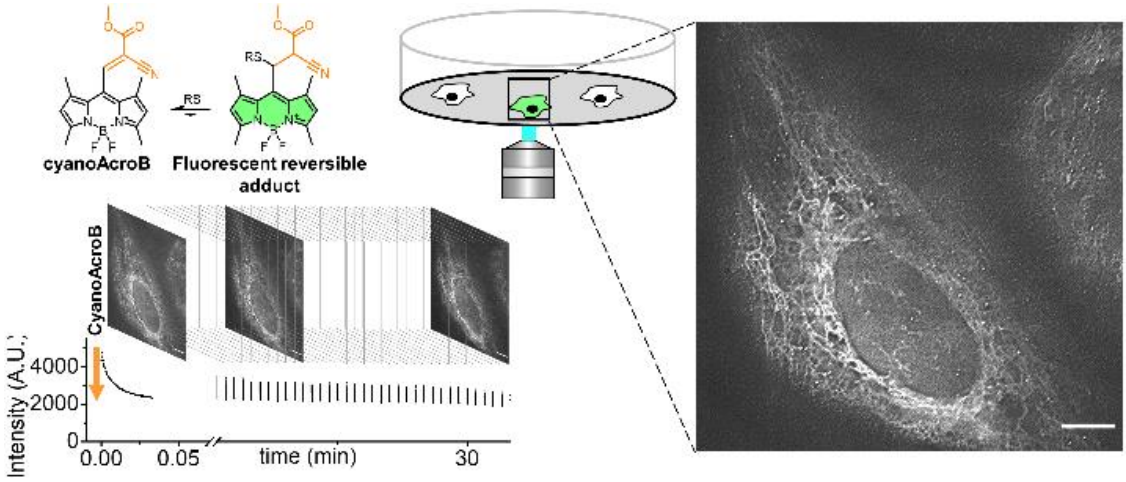

4.1 Preface

We examined the power of imaging for both the investigation of lipid peroxidation (**Chapter 2**) in the context of ferroptosis and the instigation of lipid peroxidation (**Chapter 3**) for PDT and probe autocatalysis. Here, we extend further into the biology of lipid peroxidation to examine the dynamics of lipid-derived electrophiles.

Monitoring the reactions of LDE with cellular nucleophiles has been of interest and achieved previously in our group with the creation of AcroB – a fluorogenic turn-on LDE mimic. While efficacious at highlighting hotspots of LDE reactivity, the accumulation of fluorescent products severely hindered the applicability of AcroB in live cell applications requiring more demanding temporal and spatial resolution.To that end, we introduce the reversible Michael acceptor – cyanoAcroB – as an answer. The incorporation of a cyanoacrylate moiety allows for the observation of reactions with cellular nucleophiles, as fluorescent bursts, but prevents the accumulation of fluorescent products over time that would otherwise overwhelm the signal strength of further chemical events. We demonstrate this by showing good signal-to-noise in localization-based super-resolution microscopy as well as fluctuation-based over the timescale of an hour. In addition, we validated cyanoAcroB in a ferroptosis model system, showing not only the temporal fidelity for observing organelle dynamics on the timescale of tens of minutes, but also a correlation with endogenous LDE production, paving the path for future quantitative works on LDEs in ferroptosis.

This chapter is modified from the original article in the following manner. Probe synthesis was the work of Dr. Richard Lincoln and previously reported in his thesis; it is not included in this chapter. DFT calculations in the original article were the work of Dr. Terri Lowell, also not included in this chapter. The exclusion of the two sections does not influence the conclusions drawn or the imaging data presented and will be referenced when appropriate.

4.2 Abstract:

We report a chemically-tuned fluorogenic electrophile designed to conduct live-cell super resolution imaging by exploiting its stochastic reversible alkylation reaction with cellular nucleophiles. Consisting of a lipophilic BODIPY fluorophore tethered to an electrophilic cyanoacrylate warhead, the new probe cyanoAcroB remains non-emissive due to internal conversion along the cyanoacrylate moiety. Intermittent fluorescence occurs following thiolate Michael addition to the probe followed by retro-Michael reaction, tuned by the cyano moiety in the acrylate warhead and BODIPY decoration. This design enables long-term super-resolved imaging of live cells by preventing fluorescent product accumulation and background increase, while preserving the pool of probe. We demonstrate the imaging capabilities of cyanoAcroB via two methods i) a single molecule localization microscopy imaging NASCA (nanometer accuracy by stochastic chemical activation), and ii) SRRF (super-resolution radial fluctuation). The latter tolerates higher probe concentrations and low imaging powers as it exploits the stochastic adduct dissociation. Super resolved imaging with cyanoAcroB reveals electrophile alkylation is prevalent in mitochondria and endoplasmic reticulum. The 2D dynamics of these organelles within a single cell are unraveled with tens of nanometers spatial and sub-second temporal resolution through continuous imaging of cyanoAcroB extending for tens of minutes. Extending the reversible electrophile mimic platform into a ferroptosis model, we demonstrate an elegant indirect correlation of probe fluorescence with ferroptosis-induced LDE elevation, as well as observations of organelle dynamics of potential interest. Our work underscores the opportunities that reversible fluorogenic probes with bio-inspired warheads bring toward illuminating with super-resolved features chemical reactions in live cells.

4.3 Introduction:

Super-resolution imaging methodologies have become transformative tools in biology, chemistry and physics.[1-6] Enabled by new hardware and software, at the core of super-resolution methods lie the chemical ability to switch fluorophores on and off. Some super-resolution techniques such as STED,[7] GSDIM,[8] and RESOLFT[9] require controlled fluorophore on/off switching that is achieved via photo-activating and photo-deactivating pathways. In turn, other super-resolution techniques based on single-molecule localization microscopy (SMLM) exploit a stochastic on-off cycling.[10-12] Here just a few interspersed fluorophores in a highly densely labeled substrate will glow - and be recorded - in each image frame (snapshot). In this way, the centroid position of each diffraction-limited spot is determined without overlap between closely spaced emitters within the image. Acquiring multiple frames allows the reconstruction of a high-resolution image by combining the positions computed from each frame.

Fuelled by advances in super-resolution imaging there has been an upsurge in the number of fluorescence probes being developed in the past five years for super-resolution. Based on green and red absorbing cyanine dyes,[13] rhodamines,[14-16] silicon rhodamines,[17, 18] and diarylethenes.[19, 20] Guidelines that underpin the search for new dyes include chemical robustness to maximize photon budget, red absorption to minimize cell damage and reduce autofluorescence background, and controlled on-off cycling. While cycling in most dyes comprises of photoactivation of otherwise non-emissive probes, this requires high excitation powers, typically in the UV region,[20] which is detrimental to biological specimens. Recently, spontaneously (thermal) blinking rhodamine derivatives based on an intramolecular spirocyclization reaction were reported.[17, 21] These dyes provide an ingenious way to circumvent the need for high imaging powers, where chemical tuning enables controlling on and off dwell times (rate constants of interconversion). Furthermore, on-off cycling (blinking) was achieved through reversible nucleophilic attack of intracellular glutathione (GSH) to the xanthene fluorophore in living cells. Here the free dye is emissive while its glutathione adduct (dominant species) is colorless.[22]

Chemoselective fluorogenic probes that rely on the induction/enhancement of fluorescence (off to on transition) upon reaction with a molecular entity[23-25] offer an unmatched opportunity for super-resolution imaging. With these probes, chemical reactions of interest occurring stochastically in live cells can be visualized at the single molecule level. Combined with super-resolution imaging techniques such as SMLM based NASCA[26, 27] (nanometer accuracy by stochastic chemical activation), chemoselective fluorogenic probes hold the promise to facilitate the understanding of how different cellular environments modulate chemical reactivity of biological relevance. In this regard, we recently showed that a chemoselective fluorogenic electrophile may be utilized to image mitochondria with super-resolution.[28] Unfortunately, a major caveat with ours, and related fluorogenic probes, is the inability to cycle back to a non-emissive state. Product accumulation over time thus results in a rise in the fluorescence background, reducing the time window for imaging experiments. This may be mitigated through the photobleaching of newly activated probes, yet the high excitation powers needed can cause photodamage in biological samples during live cell imaging.[29]

Here we report the design and preparation of a reversible fluorogenic electrophile cyanoAcroB that enables long term super-resolved imaging for tens of minutes on live cells. The new probe bears a reactive warhead, a chemically-reversible cyanoacrylate moiety, tuned to enable spontaneous (thermal) blinking, associated to Michael addition and retro-Michael reactions. CyanoAcroB was conceived to enable super-resolved imaging of live cells over long-term by preventing fluorescent product accumulation and concomitant background increase, while preserving intact the pool of probe. The work is driven by our desire to monitor the reaction of lipid-derived electrophile[30-34] (LDE) analogues with cellular nucleophiles. Super-resolution fluorescence imaging utilizing NASCA and SRRF[35] (super-resolution radial fluctuation) illustrated the alkylation reaction of the lipophilic electrophile probe with cellular nucleophiles in live cells over tens of minutes (**Fig. 4.1B-C**).[21] CyanoAcroB alkylation was observed in mitochondria and the endoplasmic reticulum (ER). Through the ongoing chemistry within

these organelles, we were in turn able to record these organelle dynamics within the cell. The juxtaposition of organelle dynamics and chemical kinetics can be deconvoluted enabling the correlation of chemical reactivity with organelle motion in live cells. Finally, we turn our probe towards ferroptosis, a form of cell death for which LDEs are heavily implicated in its mechanism of action,[36] and observe intracellular dynamics during cell death progression as well as competitive behaviour between probe fluorescence and endogenous LDE production. Our work underscores the opportunities that reversible fluorogenic probes with bio-inspired warheads bring toward illuminating chemical reactions in live cells with enhanced resolution.

4.4 Results and discussion:

4.4.1 Probe design, preparation and characterization:

To design a lipophilic and fluorogenic electrophile that is reversibly conjugating to nucleophiles we resorted to a BODIPY fluorophore to favour lipid membrane partitioning.[37] Fluorogenicity was in turn sought through incorporation of a reactive electrophilic warhead, an α-β unsaturation at the meso position of a BODIPY dye. Here unsaturation at the meso position rapidly deactivates 1-7 methyl substituted BODIPY fluorophores via internal conversion.[28, 38] Emission is then restored following nucleophilic attack and Michael addition.[28] Reversibility and associated spontaneous (thermal) blinking, was explored via incorporation of a cyanoacrylate electrophile warhead at the meso position. Increased acidity, we reasoned, of the α-proton following nucleophilic attack to the reactive warhead would ensure that thiolate-probe adducts undergo retro-Michael reaction,[39] rapidly dissociating the fluorescent products back to reactants. To further drive the retro-Michael addition we additionally sought to exploit the need for alleviation of the structural strain at meso position observed on 1,7 methyl substituted BODIPY dyes.[40] Accordingly, we expect a low propensity for adduct formation in the new probes with the equilibrium shifted towards reactants, and with rapid dissociation of the adduct

taking place as needed to prevent emissive product accumulation over time and to enable single molecule localization microscopy imaging.

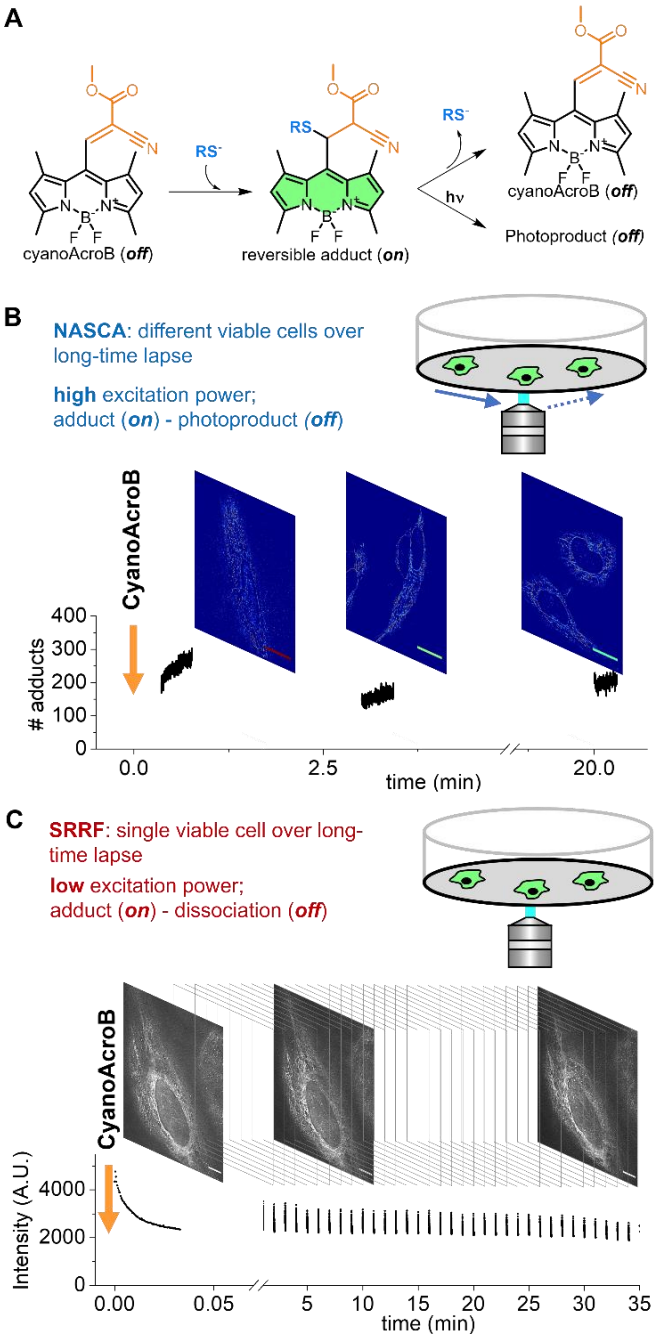

Figure 4.1: Reaction scheme of cyanoAcroB and imaging modalities enabled. **A**) Reaction scheme for the reversible fluorogenic electrophile cyanoAcroB. **B**) cyanoAcroB (25 nM) enables NASCA super resolution imaging in live HeLa cells with roughly the same number of events per cell detected per unit time, over extended time, and for different cells in a plate, with minimal background, acquired upon 488 nm excitation with 412 W/cm^2. **C**) Bursts of 100 - 20 ms exposition – frames are next used to render single reconstructed SRRF super resolution images from a single live HeLa cell imaged for tens of minutes (488 nm excitation with 41 W/cm^2. Scale bar = 10 µm).

Following probe design (Lincoln), the initial DFT validation of fluorgenicity (Lovell), and synthesis (Lincoln), we tested cyanoAcroB in live cell imaging. We confirmed that cyanoAcroB does not lead to product accumulation, consistent with its reversible nature. Here the temporal evolution of the fluorescence intensity arising from cyanoAcroB adduct formation was visualized at low excitation power via widefield microscopy (~0.5 W/cm^2). For cyanoAcroB we recorded low fluorescence intensity, mostly localized in the cell mitochondria (**Fig. S4.1-S4.2**), consistent with adduct formation followed by its rapid dissociation. Under identical conditions, studies with the irreversible electrophile AcroB resulted in the accumulation of fluorescent adducts over time and their endomembrane trafficking[28] as revealed by time-course imaging (**Fig. S4.1**). As expected from our design cyanoAcroB adducts emit only where their formation occurs and dissociate before their major trafficking into other organelles takes place.

4.4.2 NASCA imaging with cyanoAcroB.

To map and count over time the reactions of the probe within the cell, we next conducted NASCA imaging experiments (see **Fig. 4.2-4.3** and **S4.3**). Increasing the laser excitation power ~800-fold to 412 W/cm^2, working in a total internal reflection fluorescence (TIRF) configuration, and imaging at a frequency of 20 Hz allowed us to visualize the formation of single, sparse, cyanoAcroB-adducts. These manifested as single bursts of fluorescence residing on average <1 frame before their dissociation (or photodegradation) occurred. A steady state of fluorescence burst occurrences (cyanoAcroB alkylation and dissociation events) and fluorescence emission was achieved and maintained through the whole imaging window. Here cyanoAcroB−thiolate adducts were generated and dissociated/photobleached at a similar rate (**Fig. 4.2** top, also **Fig. 4.1** for a reaction scheme). In total, 150-200 alkylation events were recorded above threshold per HeLa cell, per frame, following probe addition (**Fig. 4.2** top left). In comparison, photobleaching of hundreds of initial frames (where the time of photobleaching increases with incubation time, see below) were necessary prior to NASCA data acquisition when imaging with the

irreversible probe AcroB under identical conditions (see olive bars in **Fig. 4.2**, middle right panel). Notably, formation of an irreversible fluorescent product with AcroB ultimately prevents SMLM.

The mathematical localization of individual fluorescence bursts - single events for cyanoAcroB reaction - rendered a new super-resolved image combining results from 500 frames (see **Fig. 4.3** and also S4.3). The alkylation events were recorded predominantly in the mitochondria and ER. Sub-diffraction features in these organelles were rendered through NASCA analysis. Colocalization studies with cyanoAcroB imaged with NASCA modality and MitoTracker Deep Red illustrate that cyanoAcroB events localize in the mitochondria (**Fig. S4.6**)

Studies with an intrinsically fluorescent control BODIPY dye showed that the limiting step in adduct formation is the cyanoAcroB probe arrival, rather than thiolate availability within the mitochondria and ER. This conclusion is reached upon comparing the SMLM images rendered upon registering arrival and photobleaching of the control BODIPY dye shown in **Fig. S4.4** (an experiment analogous to PAINT), with NASCA images obtained for cyanoAcroB (and AcroB). In all cases the number of localizations is comparable.

Close inspection of **Fig. 4.2** left and right panels further underscores the differences between the reversible fluorogenic probe cyanoAcroB, its irreversible fluorogenic analogue AcroB and an intrinsically fluorescent BODIPY probe. Both fluorogenic systems give rise to steady-state number of bursts, yet while the reversible one does so over a constant overall intensity, the irreversible one does it against a backdrop of increasing overall intensity with time (compare left to right plots for both probes). In turn the fluorescent compound shows a drop in the number of events with time. Here the probe is photobleached regardless of its location while fluorogenic probes are not photoactive (and thus do not photodegrade) until the adducts are formed). The data underscores the opportunities that reversible fluorogenic probes bring in SMLM imaging.

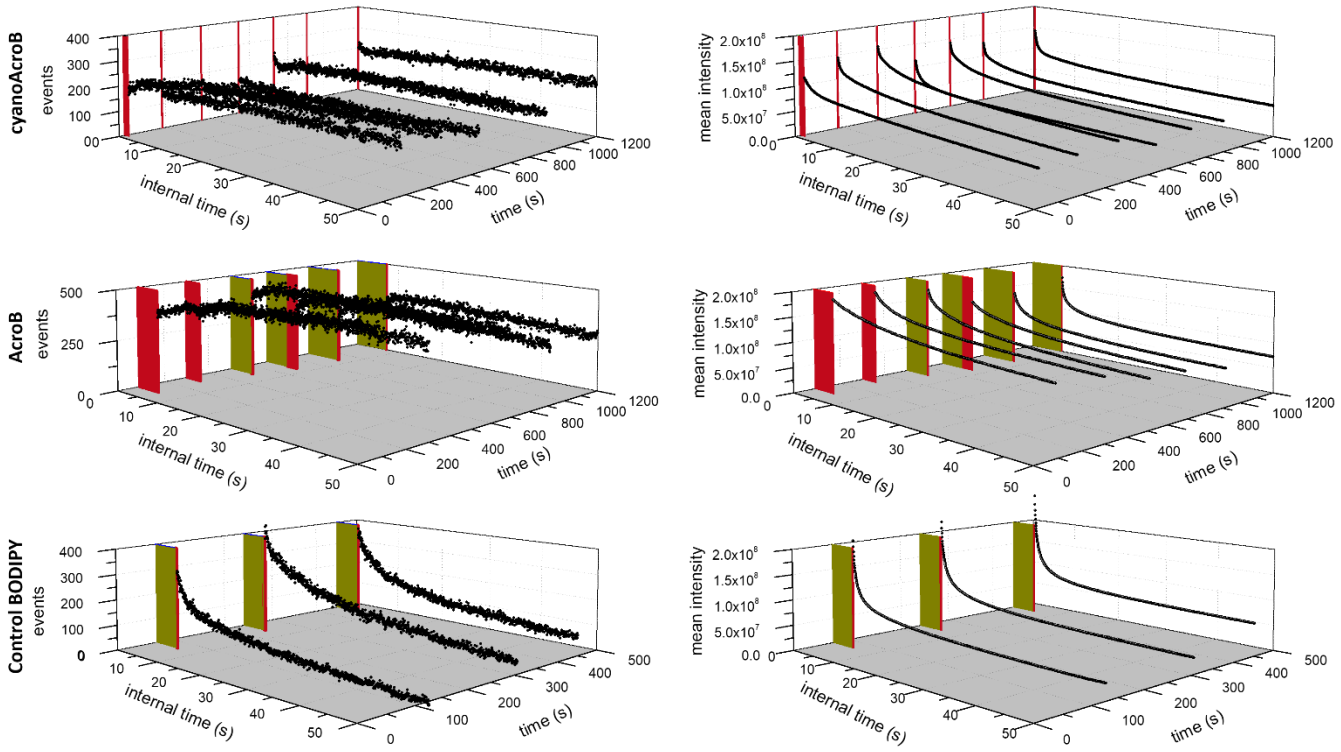

Figure 4.2: Number of events and intensity over time for cyanoAcroB, AcroB, and a control BODIPY. **Left:** number of localization events associated to alkylation by cyanoAcroB, and AcroB, and related to membrane embedding for the control BODIPY dye. Images were obtained for HeLa cells over 50 s (1000 consecutive frames), following treatment with either 25 nM cyanoAcroB, 25 nM AcroB or 25 nm control BODIPY dye (H2B-Et, **Fig.S4.3- S4.4**) and with a laser excitation power of 412 W/cm^2. Event series were recorded on different cells at different times following probe addition, see listed times on the graphs, events are as obtained except for the first trajectory with AcroB which was divided by 2. Pre-photobleaching times (reflected by the olive bar) and frame saturation (reflected by the burgundy bar) were required and occurred, respectively, upon starting imaging. **Right:** fluorescence intensity (photons) per frame recorded over time. See also **Fig. S4.3-S4.4** for super-resolution map of event images rendered over the first 500 frames (discarding saturated frames).

4.4.3 Organelle dynamics imaged via adduct formation.

Given the low background rendered with cyanoAcroB, we subsequently explored whether mitochondria and ER dynamics could be extracted from our electrophile reactivity maps. Mitochondria are highly dynamic structures, a hallmark of cell viability.[41] In NASCA/SMLM, the necessity to combine large numbers of localizations and frames over time (500 frames, 25 s to render a single NASCA image), precluded the observation of mitochondria motion. We thus utilized SRRF analysis on the same images acquired at 412 W/cm^2 excitation, reconstructing images over time upon integrating data from 0.5 s of

exposure (10 acquisition frames) to extract dynamics from our live cell imaging studies. **Fig. 4.3** depicts SRRF reconstruction of a HeLa cell treated with cyanoAcroB. The zoomed regions in the right panels, corresponding to a time difference of 2 seconds, illustrate that a fraction of the mitochondria displays highly dynamic behaviour (depicted by orange arrows). This feature is also observed in NASCA analysis when data were integrated from 0.5 s rather than from the full 25 s data set, albeit data sparsity precludes a clear visualization without a guide. Notably, prolonged photobleaching times such as those required for imaging with the irreversible probe AcroB (e.g. after ~900 s incubation of irreversible probe, where over 10 s of photobleaching are required) negatively impact these organelle dynamics indicating that cell damage takes place during the required preconditioning. Decrease in cell organelle motility with imaging time are marked in comparing the 50 frame SRRF movie reconstruction from initial 25 seconds (500 raw imaging frames) with the subsequent 25 seconds.

We reasoned that while photobleaching may occur during high power NASCA imaging, we could exploit the stochastic elimination reaction tuned in the design of cyanoAcroB - in combination with SRRF imaging - to enable super resolution under low excitation powers thus preventing cellular photodamage. Accordingly, we explored SRRF imaging under 10-fold lower excitation powers (41.2 W/cm^2) and working with either 100 nM or 1 μM probe concentrations. Images were acquired with 20 ms exposure continuously for 50 s, for a total of 2500 frames, which were then integrated into 100 SRRF frames (see **Fig. S4.5** for our optimization of SRRF imaging conditions). Reconstructed SRRF images illustrate mitochondria dynamics were not affected over time under the lower exposure conditions, where similar signal to background ratios were retrieved in both sets of data conducted at low and high cyanoAcroB concentrations.

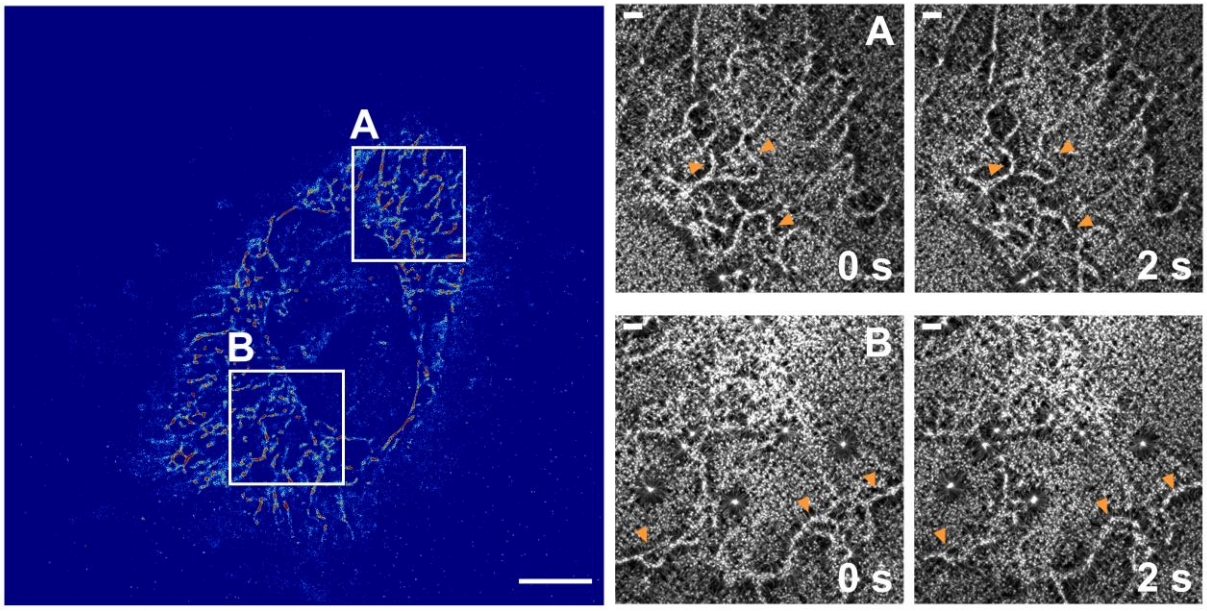

Figure 4.3: Evolution of cyanoAcroB alkylation events in HeLa cell analyzed via NASCA and SRRF. Left: NASCA localizations accumulated over the first 500 frames. Middle and Right: an expanded region analyzed via SRRF, where the image is reconstructed by combining 10 frames of 50 ms duration each, is shown initially and following 2s to illustrate mitochondria 2D dynamics (see orange arrows) as projected in the imaging EMCCD camera). Scale bars 10 µm (left) and 1 µm (center and right). CyanoAcroB was 25 nM, and the excitation power 412 W/cm^2.

4.4.4 Single cell SRRF imaging over extended time.

We finally tested whether super resolved SRRF imaging could be conducted on a single cell for tens of minutes without compromising cell viability or image quality. **Figure 4.4**, top, illustrates reconstructed SRRF images obtained from a single cell monitored over 60 minutes under 41.2 W/cm^2 excitation power. Here the cell was exposed for 2 s every minute to collect a burst of 100 frames of 20 ms exposition each, which were next used to render a single SRRF frame. Organelle dynamics could then be retrieved for up to forty-five minutes of imaging without affecting resolution. Colocalization studies with cyanoAcroB imaged via SRRF modality and MitoTracker Deep Red illustrate that cyanoAcroB localizes in mitochondria (**Fig S4.7**). Notably, the filamentous structures observed bear striking resemblance to ER imaged via super-resolution microscopy.[21] A fading becomes noticeable afterward, which we assign to cellular decay. For comparison we evaluated imaging with the irreversible probe AcroB under otherwise identical conditions. The bottom panel in **Figure 4.4** reveals that the increasing background rapidly, within a minute, precludes SRRF imaging for this irreversible probe.

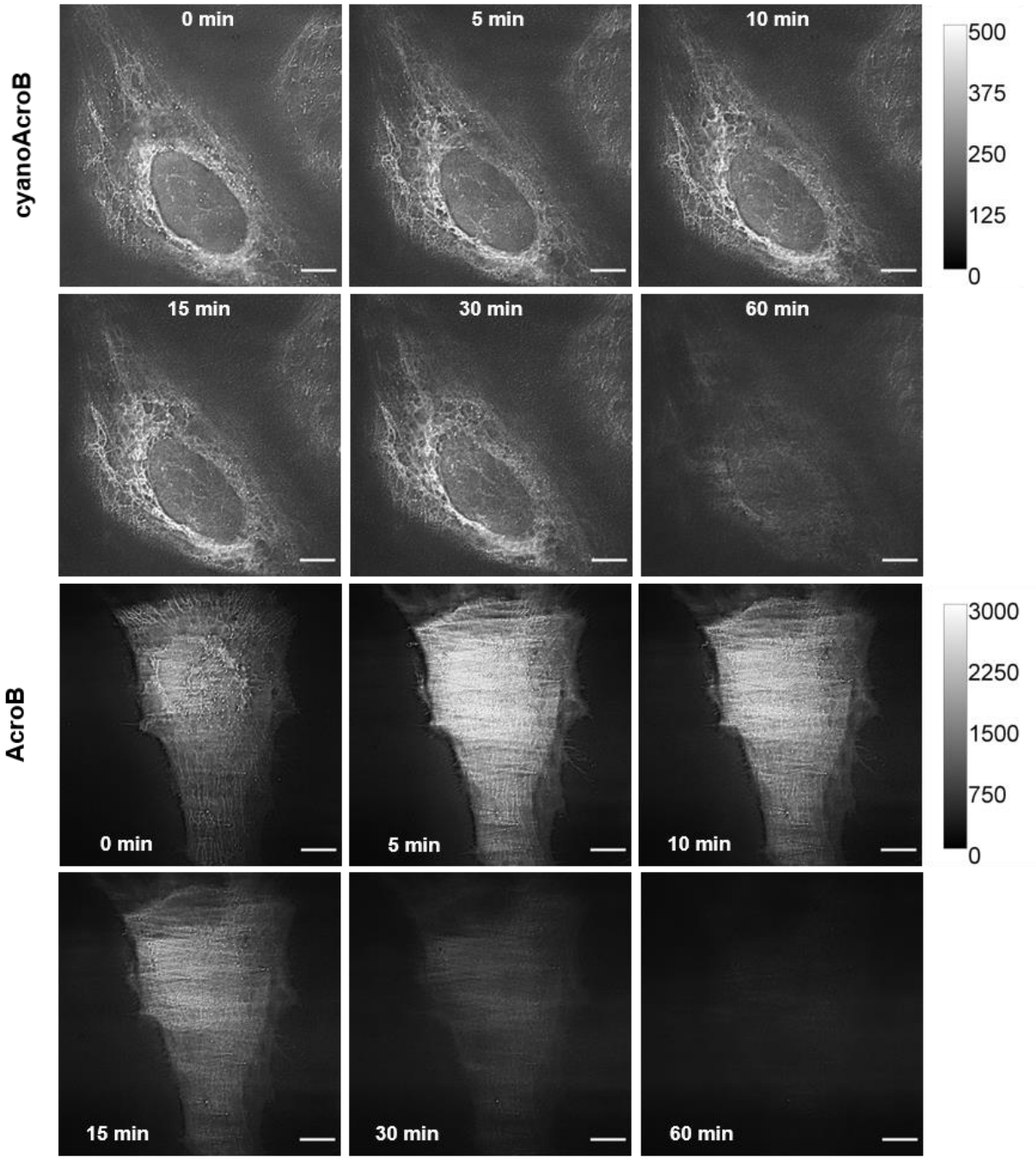

Figure 4.4: cyanoAcroB alkylation events in HeLa cell analyzed *via* SRRF at low imaging powers, contrasted to studies with irreversible probe AcroB. Top: SRRF images with cyanoAcroB reconstructed by combining 100 frames of 20 ms duration each (see also **Fig. 4.1C**). Bottom: SRRF images with AcroB constructed by combining 100 frames of 20 ms duration each. Sequences of 100 frames (leading to 1 SRRF-rendered frame) were taken once per minute for 60 minutes, using 100 nM probe and 41.2 W/cm^2 excitation power. Scale bars are 10 µm.

4.4.5 cyanoAcroB revealing intracellular details by preventing background accumulation in a ferroptosis system

Having underscored the potential of cyanoAcroB for super resolution imaging studies, we next sought to exploit this fluorogenic electrophile in the study of LDE during ferroptosis. LDEs have been implicated in post-translational modifications of key proteins for the induction of, as well as potentially causing the membrane permeabilization pathology characteristic of ferroptosis. Our group recently demonstrated the utility in AcroB in the study of ferroptosis, by quantifying the ratio of its enhancement as well as its background accumulation, to demonstrate the impairment of LDE detoxification associated with LDE accumulation, as a hallmark of ferroptosis.[36] However, the resultant background accumulation occludes the intracellular dynamics of cells undergoing ferroptosis with excess fluorescent products, preventing the quantification of chemical events similar to the NASCA analysis (see above) at the single cell level. Here, we posited cyanoAcroB offers an opportunity to resolve intracellular details, due to the absence of background accumulation, allowing the observation of alkylation real time during ferroptosis progression.

Figure 4.5 displays results obtained with HT-1080 cells – a cell line sensitive to ferroptosis – treated with RSL3 – a bona fide ferroptosis inducer prior to imaging with the LDE mimicking probes AcroB and cyanoAcroB. Several key points of comparison can be made, in between the two probes, as well as upon treatment with ferroptosis inducer. In comparison to AcroB, cyanoAcroB yields a lower signal intensity (**Fig. 4.5A**). In RSL3-treated cells, the mitochondrial network – the site of highest pH and thiolate concentration – is resolved clearly in both the TIRF images as well as the SRRF reconstructions of cyanoAcroB, while AcroB is obscured by high background fluorescence. Here, good signal to noise for cyanoAcroB is maintained for up to one hour of imaging (**Fig. 4.5B**), in congruence with HeLa cell results and further emphasizing the strength of this probe and relevance for the study of biological questions. Most interestingly is the change in cyanoAcroB fluorescence intensity upon ferroptosis induction

(compare **Fig. 4.5A** vs **4.5B**). We reason that the loss of fluorescence upon ferroptosis induction with RSL3 is a result of cyanoAcroB being outcompeted for nucleophiles by the high concentration of LDEs generated from lipid peroxidation. In contrast for AcroB, cell fluorescence intensity increased because fluorescent adduct excretion is inhibited upon RSL3 treatment (compare **Fig. 4.5A** vs **4.5B**), despite the increase in LDE levels outcompeting AcroB for nucleophiles. CyanoAcroB illustrates that lack of excretion is not an impediment for unraveling dynamics and opens up the possibility of quantitative, albeit indirect, measurements of LDE levels throughout the progression of ferroptosis.

Using both AcroB and cyanoAcroB, we report an observation of mitochondrial morphology change (**Fig. 4.6**) in HT-1080 cells upon the induction of ferroptosis with RSL3. In AcroB, the initial occlusion of cytoplasm by fluorescent products resolves over time, likely due to photobleaching. Intracellular structural details could be resolved in SRRF, showing the formation of loop structures. This observation is also seen in cyanoAcroB , which has a propensity for mitochondria – due to preferential activation of the probe in the elevated pH environment favouring thiolate formation – where the formerly filamentous structure characteristic of mitochondria appears to form loops.

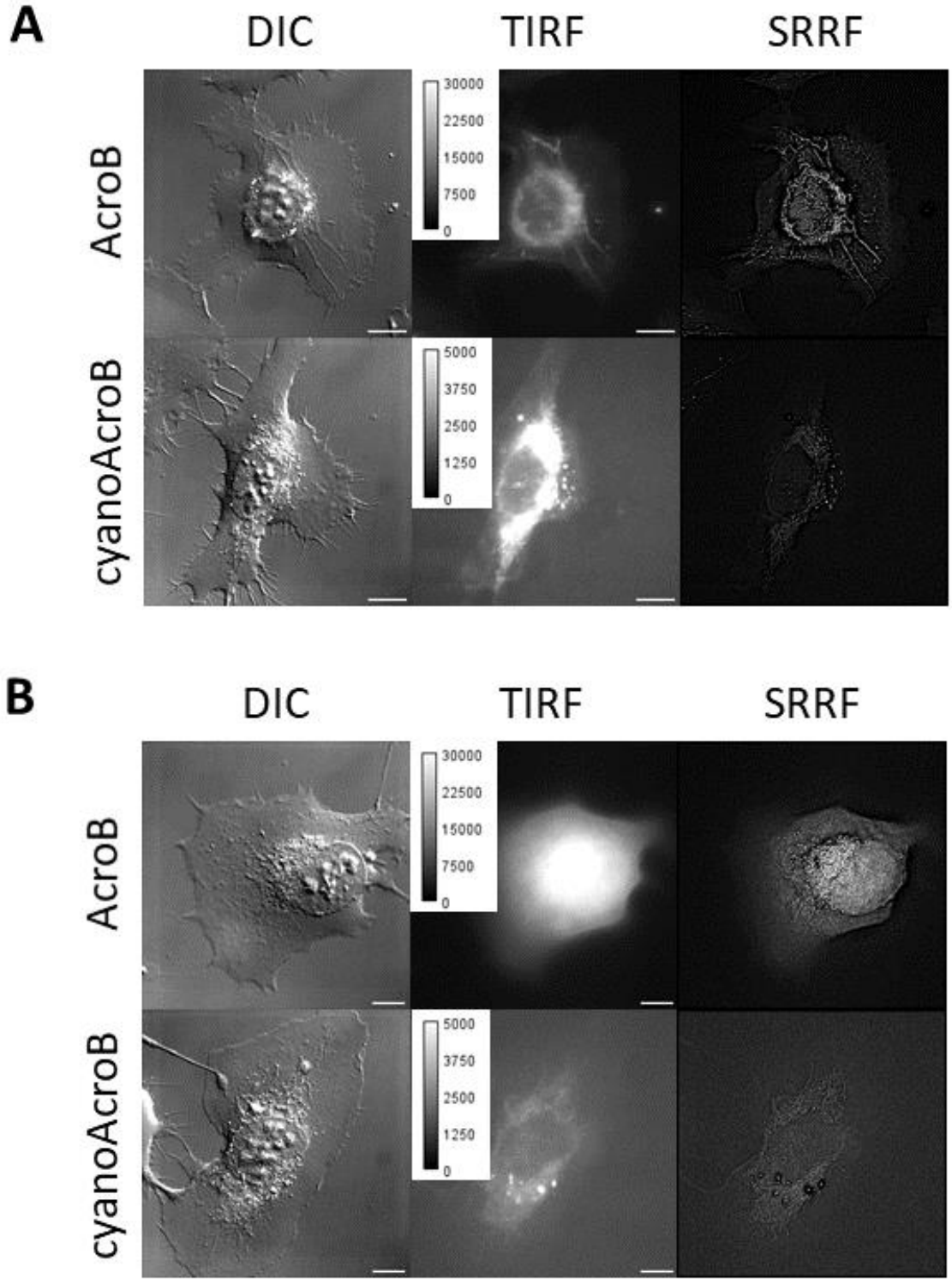

Figure 4.5: SRRF imaging of cyanoAcroB and AcroB in a) basal and b) ferroptosis-induced HT-1080s cell. Cells were treated with RSL3 (1 uM, 1hr) in DMEM prior to exchange into LCIS. cyanoAcroB or AcroB (100nM, 0.33% DMSO) was added immediately prior to imaging. SRRF images were reconstructed from 100x20ms acquisitions at 41.2 W/cm2 excitation power. Scale bars are 12 µm.

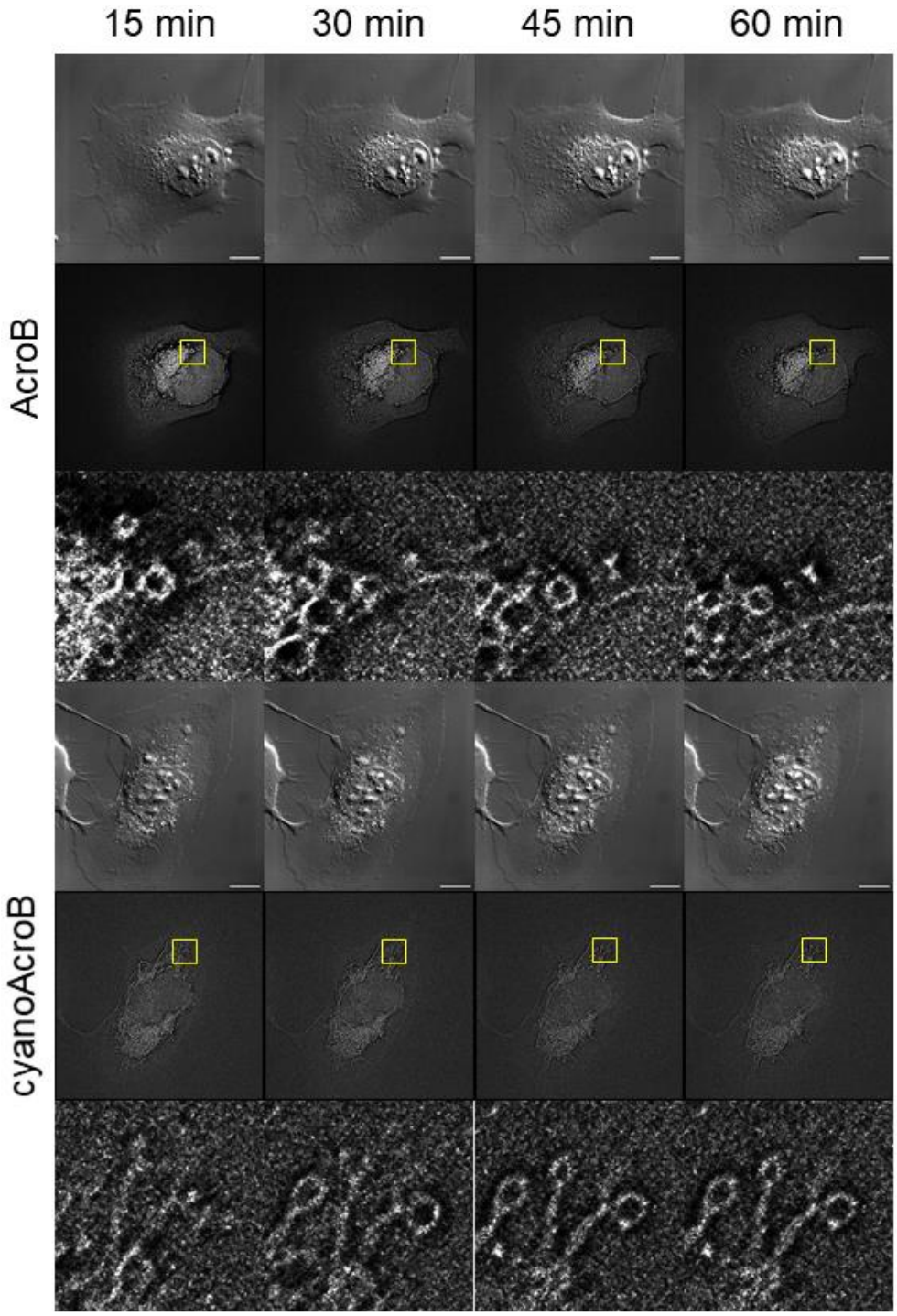

Figure 4.6: Timecourse SRRF imaging of AcroB and cyanoAcroB in ferroptosis-induced HT-1080s cell. Cells were treated with RSL3 (1 uM, 1hr) in DMEM prior to exchange into LCIS. cyanoAcroB or AcroB (100nM, 0.33% DMSO) was added immediately prior to imaging. SRRF images were reconstructed from 100x20ms acquisitions at 41.2 W/cm^2 excitation power. Boxed region zoomed in to highlight to morphologies of interest. Scale bars are 12 µm.

4.5 Conclusions:

Utilizing the chemically reversible fluorogenic probe cyanoAcroB ensures fluorescence intensity remains low over time. This enabled super-resolved experiments to be conducted on single or multiple cells within the same dish, over long-time lapse. CyanoAcroB enables mapping alkylation events in live cells yielding super-resolved charts of reactivity exploiting stochastic chemical activation and deactivation of the probes. Here the lipophilic electrophile reactions are mostly circumscribed to mitochondria and endoplasmic reticulum, due to the number of nucleophilic reactants partly associated with the higher pH in mitochondria. Imaging experiments involving single molecule localization microscopy techniques (NASCA) and methods that involve super-resolution reconstruction based on a gradient field (SRRF) are shown to facilitate the understanding of how different cellular environments modulate reactivity. Working with the reversible electrophile NASCA provides rich kinetic information on nucleophilic reactions with electrophiles, while SRRF enables monitoring single cell for tens of minutes, mapping where chemistry takes place exploiting both the stochastic adduct formation and dissociation. SRRF based analysis of acquired images further permitted monitoring of mitochondria dynamics on single cells for up to forty-five minutes with super resolved features.

From a biological perspective, LDEs are implicated in cellular toxicity and the pathogenesis of neurodegenerative diseases[33, 34] and atherosclerosis,[42] among others. A growing interest in the fate of LDEs in the context of ferroptosis, can also be better explored with cyanoAcroB in comparison to its non-reversible Michael acceptor analogue AcroB. The new probe cyanoAcroB holds opportunities to explore with enhanced spatiotemporal resolution how cellular pathologies and metabolic conditions my affect the spatial and temporal profile of lipophilic electrophile reactivity.

4.6 Materials and methods:

4.6.1 Materials

HPLC grade solvents for spectroscopy, buffers, and cell culture reagents were purchased through ThermoFisher. Water used was purified via a Millipore Milli-Q system. All other chemicals were purchased through MilliporeSigma and used without further purification

4.6.2 Cell culture

HeLa (ATCC CCL-2) were cultured in Dulbecco's Modified Eagle Medium (DMEM, high glucose, L-glutamine, phenol red, pyruvate), supplemented with 10% FBS and 1x penicillin-streptomycin. Cells were maintained at in a humidified incubator at 37°C and 5% CO_2. Cells were passaged at approximately 90% confluency. HT1080 cells (ATCC CCL-121) were cultured identically to HeLas, save for the supplementation of non-essential amino acids in the DMEM.

For imaging, cells were plated on 35mm glass bottom imaging dishes (FluoroDish, World Precision Instruments, Inc.) coated with fibronectin (1 μg/cm^2, Corning) and plated one day prior to imaging at 50% of cell count expected on day of imaging (HeLa doubling time ~1 day). Prior to imaging, media was removed and washed 3x with Live Cell Imaging Solution (LCIS, ThermoFisher).

For mitochondria colocalization experiments: HeLa cells were stained with MitoTracker Deep Red (50 nM, ThermoFisher) for 5 minutes in DMEM. The media was then removed and washed 3x with LCIS prior to cyanoAcroB staining and imaging.

cyanoAcroB/AcroB were prepared in DMSO at 300x concentration used for imaging before being diluted DMEM to 3x concentration (1% v/v). The dye solution was added to the imaging dish prior to imaging to its final 1x concentration (0.33% DMSO v/v).

For cell viability assay, HeLa cells were plated in 96-well plates (Corning) at a density of 10 000 cells/well 24 hour prior to treatment. Cells were then treated with a dilution series of AcroB/cyanoAcroB (0.33% DMSO v/v) across the relevant concentration range for imaging, and incubated for one hour.

Rezasurin was then added to the cells and developed for 4 hours and then measured on a fluorescence well plate reader.

4.6.3 Microscopy

Imaging (DIC was performed on a Nikon Eclipse Ti inverted total internal reflection fluorescence (TIRF) microscope equipped with a motorized turret and Perfect Focus System (PFS).The laser (Agilent MLC-400B) emissions were filtered (ZT488/640rpc, Chroma), and captured using a high numerical aperture oil objective (Nikon CFI SR Apochromat TIRF 100x, NA = 1.49) and an EMCCD camera (Andor iXon Ultra DU-897). Cells were maintained at 37°C and 5% CO_2 using a stage top incubator (Tokai Hit).

4.6.4. Image analysis

SRRF images were analysed with the NanoJ suite of plugins in FIJI/ImageJ. Analysis settings: ring radius 0.5, radiality magnification 5, axes in ring 6, Temporal Radiality Maximum used). Fast timelapse imaging was conducted at 20 ms exposure for 2500 frames (50s total time), and then integrated into 100 SRRF frames at 0.5 s time resolution. Long timecourse imaging was conducted at 20 ms for 100 frames, every minute for 60 minutes.

4.6.8. Instrumentation

Absorption spectra were recorded using a Hitachi U-2800 UV-Vis spectrophotometer and a 1 cm quartz cuvette. Fluorescence spectra were recorded using a PTI QuantaMaster fluorimeter and corrected for detector sensitivity. Fluorescence well plate reader measurements were conducted using a BioTek Synergy H4.

4.7 Supplementary information:

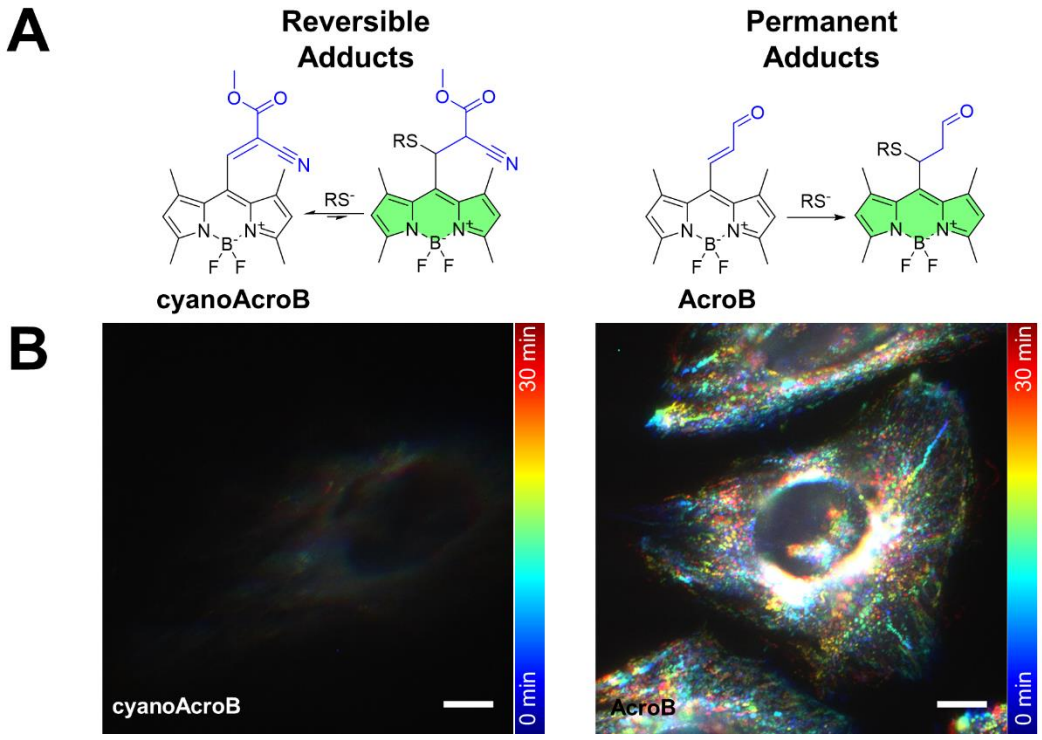

Figure S4.1: Structures of cyanoAcroB and an irreversible electrophile, AcroB. Also shown are differences in the temporal evolution of fluorescence in HeLa cells treated with these fluorogenic electrophiles. HeLa cells were treated with 100 nM of the fluorogenic electrophiles and imaged via widefield microscopy with 50 µW (50 x 10^{-2} W/cm^2) excitation. Color scheme provides a time stamp at which features were recorded. Scale bars are 10 µm.

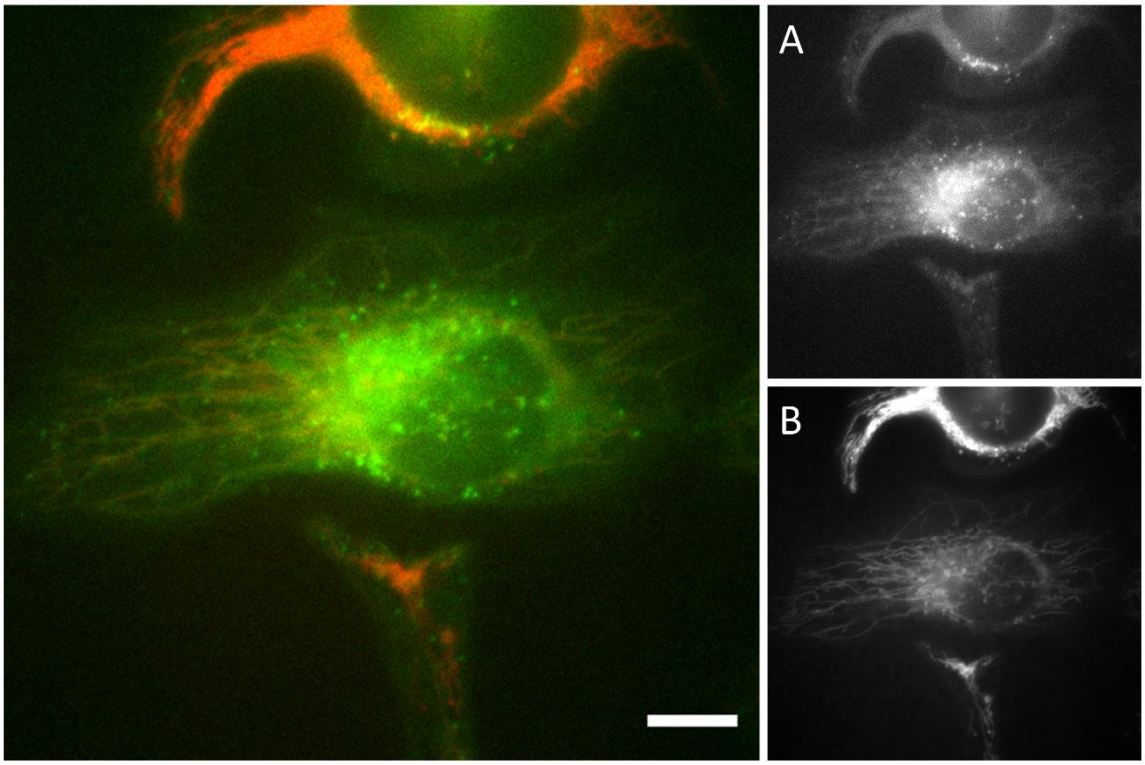

Figure S4.2: Colocalization of cyanoAcroB chemical events with mitochondria stain MitoTracker Deep Red in HeLa cells. HeLa cells were treated with 100 nM cyanoAcroB (green) and 50 nM MitoTracker Deep Red (red) and imaged in widefield configuration with 2 mW excitation (20 W/cm^2)). A) cyanoAcroB fluorescence only. B) MitoTracker fluorescence only. Due to the reversible nature of cyanoAcroB probe, only a small fraction of the dye is emissive at a given time, thus images appear with low contrast under standard imaging conditions. In turn the MitoTracker Deep Red probe, a bright reporter designed to be constantly emissive, yields better quality images under steady state. Scale bar is 10 µm.

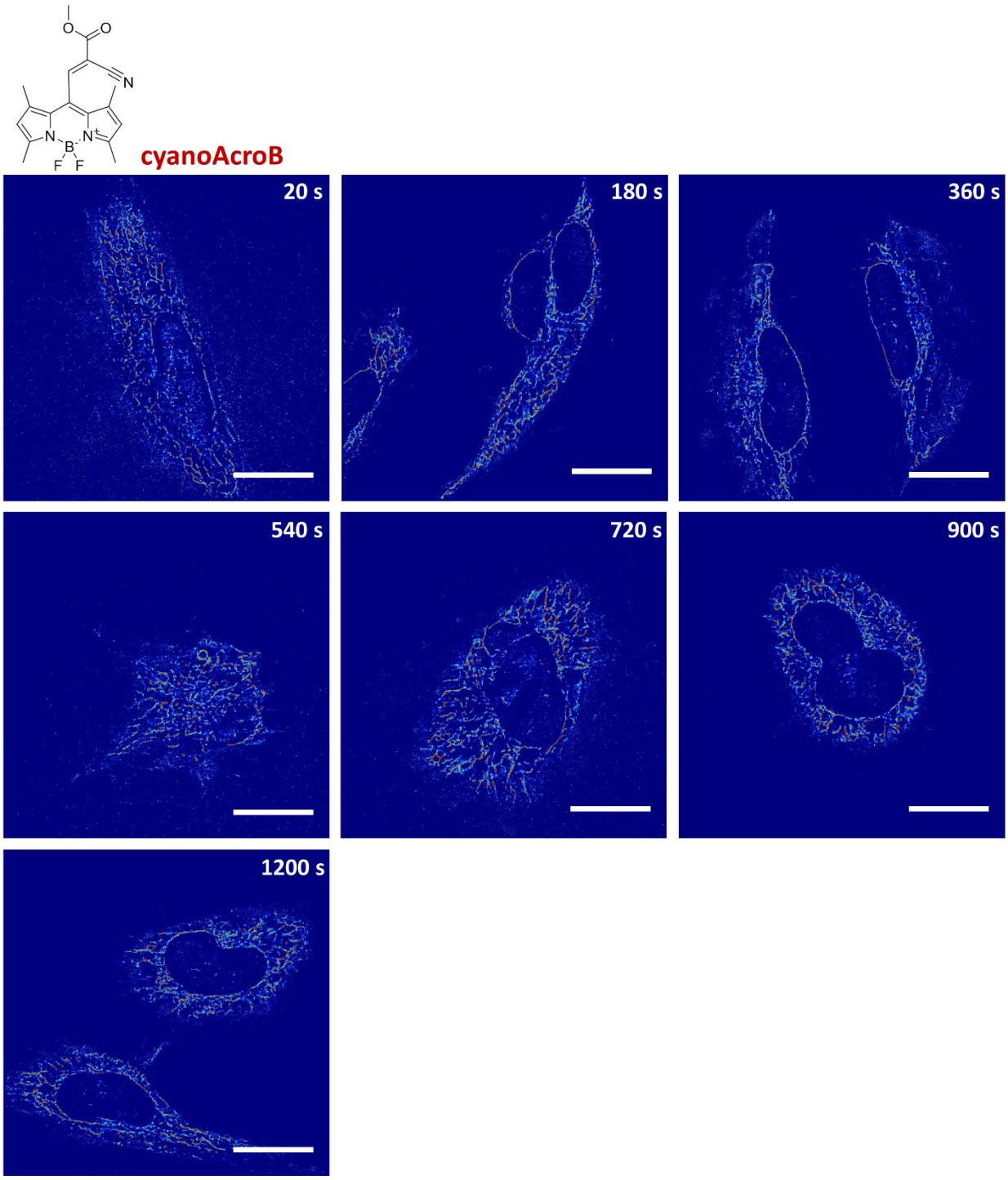

Figure S4.3: Super-resolved mapping of cyanoAcroB alkylation events in HeLa cells recorded at different times following probe addition. Cells were treated with 25 nM cyanoAcroB. Images result from accumulating all events over the first 500 frames (after discarding saturated frames, see also **Fig. 2**) analyzed *via* NASCA. Addition times are listed at the top. Scale bars are 20 µm.

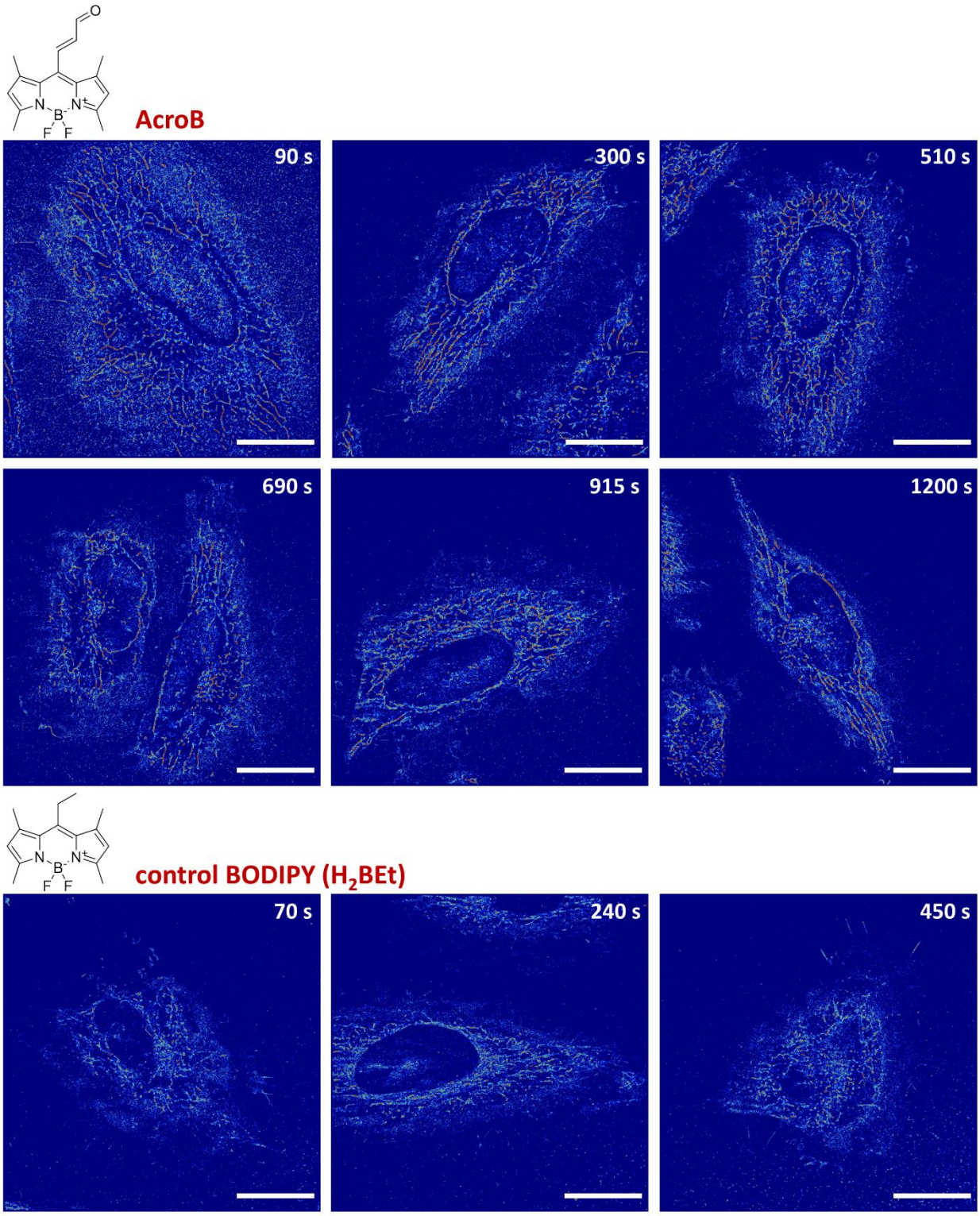

Figure S4.4: Super-resolved mapping of alkylation events by the irreversible electrophile AcroB, analyzed *via* NASCA and localization events of the lipophilic fluorescent control BODIPY dye (H_2BEt), both in HeLa cells, recorded at different times following dye addition. The images correspond to those depicted in **Fig. 2** in the main text. The events were recorded at different times following probe addition (see panel top). Scale bars are 20 µm.

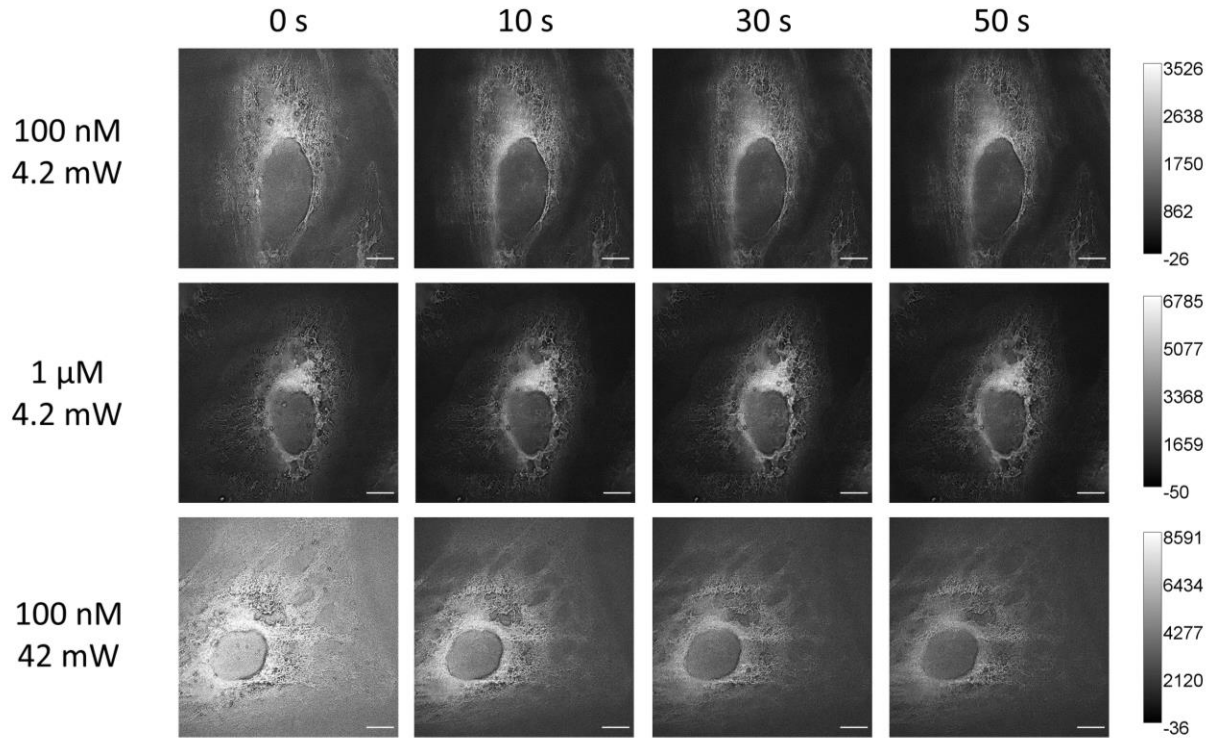

Figure S4.5: Optimization of cyanoAcroB imaging conditions for SRRF fast time lapse imaging. HeLa cells were imaged continuously for 50 s at 20 ms exposure and SRRF images were integrated at 25 frames/construction (0.5 s time resolution each). Here, the only 4 timepoints for each condition are presented. Scale bars are 10 µm. Powers are reported out of the objective, considering that the power is distributed across a 100 x 100 µm region it provides an upper estimate for the power density of 41.2 x 10 W/cm^2 and 412 x 10 W/cm^2.

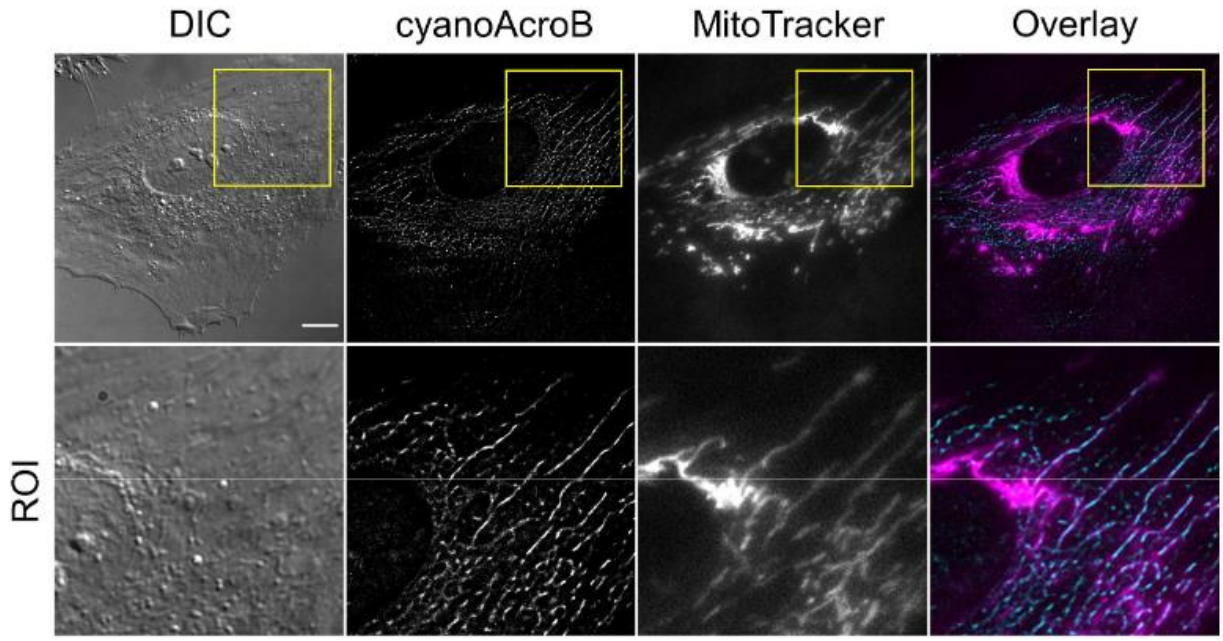

Figure S4.6: Colocalization of cyanoAcroB, imaged via NASCA, with mitochondria marker. HeLa cells were treated with 100 nM cyanoACroB (cyan in overlaid image) and 10 nM MitoTrakcer Deep Red (magenta in overlaid image) and imaged in TIRF configuration with 488 nm, 412 W/cm2 excitation (for cyanoAcroB). Colocalized signals are observed from cyanoAcroB imaged via NASCA modality and MitoTracker Deep Red in mitochondria, characterized by the defined rod-like morphologies. Localizations result from accumulating all events over the first 500 frames (after discarding saturated frames) analyzed via NASCA. ROI is 2.5x size of original image. Scale bar is 10 µm.

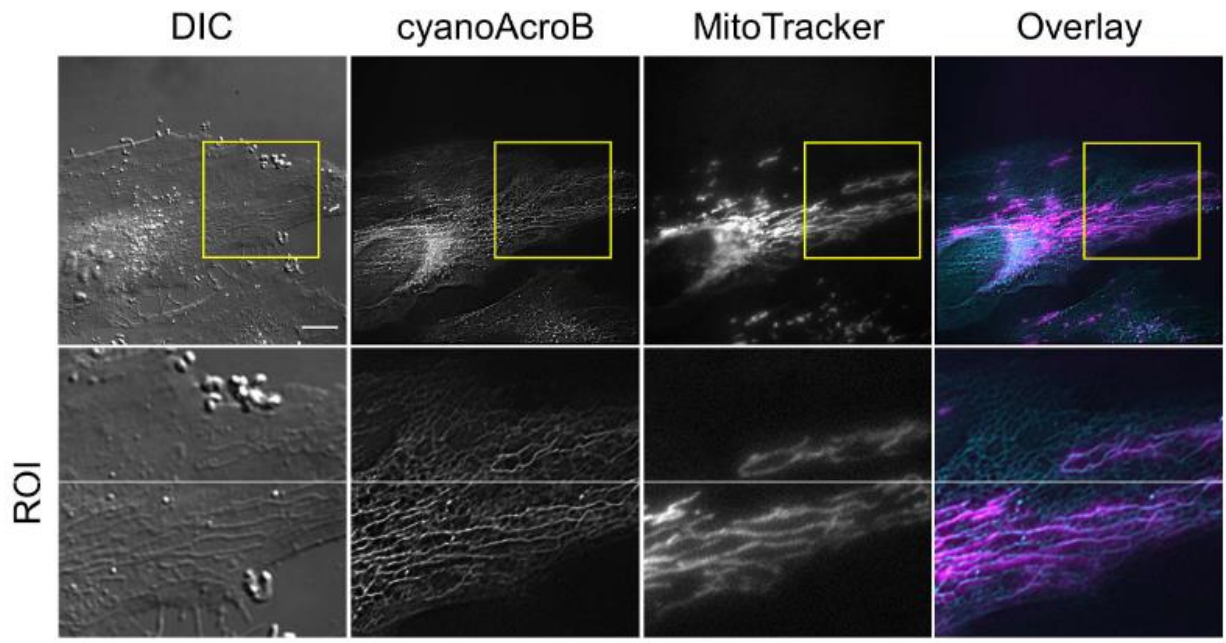

Figure S4.7: Colocalization of cyanoAcroB, imaged via SRRF, with mitochondria marker. HeLa cells were treated with 100 nM cyanoACroB (cyan in overlaid image) and 10 nM MitoTrakcer Deep Red (magenta in overlaid image) and imaged in TIRF configuration with 488 nm, 41.2 W/cm2 excitation (for cyanoAcroB). Colocalized signals are observed from cyanoAcroB imaged via SRRF modality and MitoTracker Deep Red in mitochondria, characterized by the defined rod-like morphologies. It is worth noting in addition that the filamentous structures observed bear striking resemblance to ER imaged via super-resolution microscopy. SRRF image was constructed with 100 frames imaged at 20ms. ROI is 2.5x size of original image. Scale bar is 10 µm.

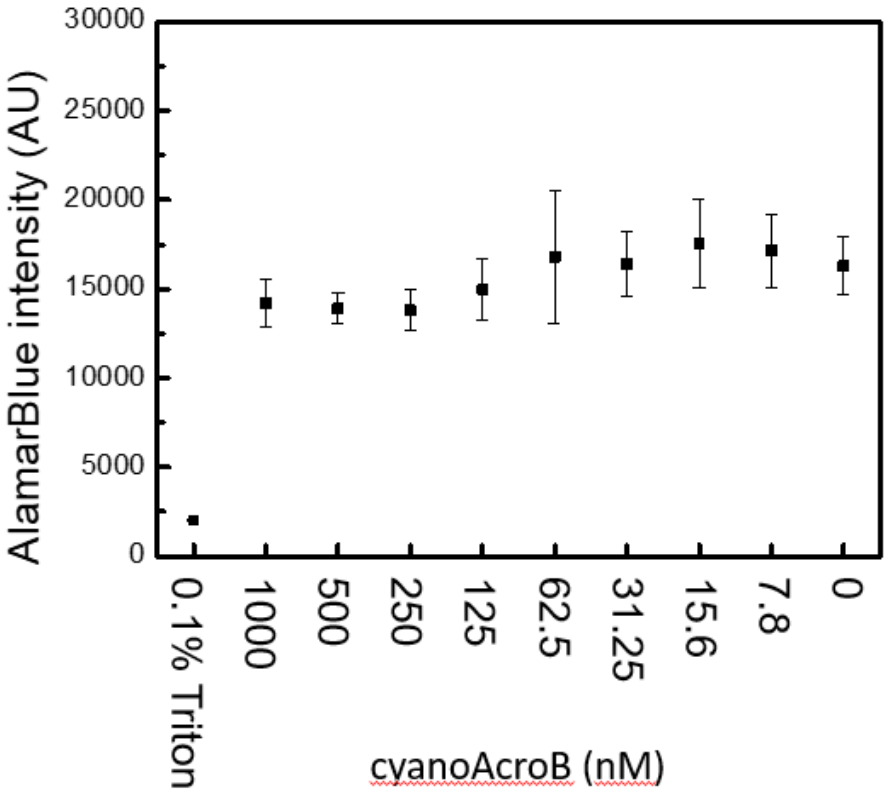

Figure S4.8: Cell viability assessment of cyanoAcroB. Cells were treated for 1hr with varying concentrations of cyanoAcroB before assessment by AlamarBlue assay (resazurin).

4.8 References

(1) Moerner, W. E. Single-Molecule Spectroscopy, Imaging, and Photocontrol: Foundations for Super-Resolution Microscopy (Nobel Lecture). *Angew Chem Int Ed Engl* **2015**, *54* (28), 8067-8093. DOI: 10.1002/anie.201501949.
(2) Biteen, J.; Willets, K. A. Introduction: Super-Resolution and Single-Molecule Imaging. *Chemical Reviews* **2017**, *117* (11), 7241-7243. DOI: 10.1021/acs.chemrev.7b00242.
(3) Sauer, M.; Heilemann, M. Single-Molecule Localization Microscopy in Eukaryotes. *Chemical Reviews* **2017**, *117* (11), 7478-7509. DOI: 10.1021/acs.chemrev.6b00667.
(4) Chen, T.; Dong, B.; Chen, K.; Zhao, F.; Cheng, X.; Ma, C.; Lee, S.; Zhang, P.; Kang, S. H.; Ha, J. W.; et al. Optical Super-Resolution Imaging of Surface Reactions. *Chemical Reviews* **2017**, *117* (11), 7510-7537. DOI: 10.1021/acs.chemrev.6b00673.
(5) Sigal, Y. M.; Zhou, R.; Zhuang, X. Visualizing and discovering cellular structures with super-resolution microscopy. *Science* **2018**, *361* (6405), 880. DOI: 10.1126/science.aau1044.
(6) Möckl, L.; Moerner, W. E. Super-resolution Microscopy with Single Molecules in Biology and Beyond–Essentials, Current Trends, and Future Challenges. *Journal of the American Chemical Society* **2020**. DOI: 10.1021/jacs.0c08178.
(7) Hell, S. W.; Wichmann, J. Breaking the diffraction resolution limit by stimulated emission: stimulated-emission-depletion fluorescence microscopy. *Opt. Lett.* **1994**, *19* (11), 780-782. DOI: 10.1364/OL.19.000780.
(8) Bretschneider, S.; Eggeling, C.; Hell, S. W. Breaking the Diffraction Barrier in Fluorescence Microscopy by Optical Shelving. *Physical Review Letters* **2007**, *98* (21), 218103. DOI: 10.1103/PhysRevLett.98.218103.
(9) Hofmann, M.; Eggeling, C.; Jakobs, S.; Hell, S. W. Breaking the diffraction barrier in fluorescence microscopy at low light intensities by using reversibly photoswitchable proteins. *Proceedings of the National Academy of Sciences, USA* **2005**, *102* (49), 17565. DOI: 10.1073/pnas.0506010102.
(10) Rust, M. J.; Bates, M.; Zhuang, X. Sub-diffraction-limit imaging by stochastic optical reconstruction microscopy (STORM). *Nature Methods* **2006**, *3* (10), 793-796, 10.1038/nmeth929. DOI: http://www.nature.com/nmeth/journal/v3/n10/suppinfo/nmeth929_S1.html.
(11) Hess, S. T.; Girirajan, T. P. K.; Mason, M. D. Ultra-High Resolution Imaging by Fluorescence Photoactivation Localization Microscopy. *Biophysical journal* **2006**, *91* (11), 4258-4272. DOI: 10.1529/biophysj.106.091116.
(12) Betzig, E.; Patterson, G. H.; Sougrat, R.; Lindwasser, O. W.; Olenych, S.; Bonifacino, J. S.; Davidson, M. W.; Lippincott-Schwartz, J.; Hess, H. F. Imaging Intracellular Fluorescent Proteins at Nanometer Resolution. *Science* **2006**, *313* (5793), 1642-1645. DOI: 10.1126/science.1127344.
(13) Dempsey, G. T.; Vaughan, J. C.; Chen, K. H.; Bates, M.; Zhuang, X. Evaluation of fluorophores for optimal performance in localization-based super-resolution imaging. *Nat Methods* **2011**, *8* (12), 1027-1036. DOI: 10.1038/nmeth.1768.
(14) Grimm, J. B.; English, B. P.; Choi, H.; Muthusamy, A. K.; Mehl, B. P.; Dong, P.; Brown, T. A.; Lippincott-Schwartz, J.; Liu, Z.; Lionnet, T.; et al. Bright photoactivatable fluorophores for single-molecule imaging. *Nat Methods* **2016**, *13* (12), 985-988. DOI: 10.1038/nmeth.4034.
(15) Grimm, J. B.; English, B. P.; Chen, J.; Slaughter, J. P.; Zhang, Z.; Revyakin, A.; Patel, R.; Macklin, J. J.; Normanno, D.; Singer, R. H.; et al. A general method to improve fluorophores for live-cell and single-molecule microscopy. *Nat Methods* **2015**, *12* (3), 244-250, Article. DOI: 10.1038/nmeth.3256.
(16) Grimm, J. B.; Muthusamy, A. K.; Liang, Y.; Brown, T. A.; Lemon, W. C.; Patel, R.; Lu, R.; Macklin, J. J.; Keller, P. J.; Ji, N.; et al. A general method to fine-tune fluorophores for live-cell and in vivo imaging. *Nat Methods* **2017**, *14* (10), 987-994, Article. DOI: 10.1038/nmeth.4403.

(17) Uno, S. N.; Kamiya, M.; Yoshihara, T.; Sugawara, K.; Okabe, K.; Tarhan, M. C.; Fujita, H.; Funatsu, T.; Okada, Y.; Tobita, S.; et al. A spontaneously blinking fluorophore based on intramolecular spirocyclization for live-cell super-resolution imaging. *Nat Chem* **2014**, *6* (8), 681-689, Article. DOI: 10.1038/nchem.2002.
(18) Koide, Y.; Urano, Y.; Hanaoka, K.; Piao, W.; Kusakabe, M.; Saito, N.; Terai, T.; Okabe, T.; Nagano, T. Development of NIR fluorescent dyes based on Si-rhodamine for in vivo imaging. *J Am Chem Soc* **2012**, *134* (11), 5029-5031. DOI: 10.1021/ja210375e.
(19) Uno, K.; Bossi, M. L.; Irie, M.; Belov, V. N.; Hell, S. W. Reversibly Photoswitchable Fluorescent Diarylethenes Resistant against Photobleaching in Aqueous Solutions. *Journal of the American Chemical Society* **2019**, *141* (41), 16471-16478. DOI: 10.1021/jacs.9b08748.
(20) Uno, K.; Aktalay, A.; Bossi, M. L.; Irie, M.; Belov, V. N.; Hell, S. W. Turn-on mode diarylethenes for bioconjugation and fluorescence microscopy of cellular structures. *Proceedings of the National Academy of Sciences, USA* **2021**, *118* (14), e2100165118. DOI: 10.1073/pnas.2100165118.
(21) Takakura, H.; Zhang, Y.; Erdmann, R. S.; Thompson, A. D.; Lin, Y.; McNellis, B.; Rivera-Molina, F.; Uno, S.-n.; Kamiya, M.; Urano, Y.; et al. Long time-lapse nanoscopy with spontaneously blinking membrane probes. *Nature Biotechnology* **2017**, *35* (8), 773-780. DOI: 10.1038/nbt.3876.
(22) Morozumi, A.; Kamiya, M.; Uno, S.-n.; Umezawa, K.; Kojima, R.; Yoshihara, T.; Tobita, S.; Urano, Y. Spontaneously Blinking Fluorophores Based on Nucleophilic Addition/Dissociation of Intracellular Glutathione for Live-Cell Super-resolution Imaging. *Journal of the American Chemical Society* **2020**, *142* (21), 9625-9633. DOI: 10.1021/jacs.0c00451.
(23) Chan, J.; Dodani, S. C.; Chang, C. J. Reaction-based small-molecule fluorescent probes for chemoselective bioimaging. *Nat Chem* **2012**, *4* (12), 973-984, 10.1038/nchem.1500.
(24) Krumova, K.; Cosa, G. Fluorogenic probes for imaging reactive oxygen species. In *Photochemistry: Volume 41*, Vol. 41; The Royal Society of Chemistry, 2013; pp 279-301.
(25) Terai, T.; Nagano, T. Fluorescent probes for bioimaging applications. *Current Opinion in Chemical Biology* **2008**, *12* (5), 515-521. DOI: http://dx.doi.org/10.1016/j.cbpa.2008.08.007.
(26) Roeffaers, M. B.; De Cremer, G.; Libeert, J.; Ameloot, R.; Dedecker, P.; Bons, A. J.; Buckins, M.; Martens, J. A.; Sels, B. F.; De Vos, D. E.; et al. Super-resolution reactivity mapping of nanostructured catalyst particles. *Angewandte Chemie (English Edition)* **2009**, *48* (49), 9285-9289, https://doi.org/10.1002/anie.200904944. DOI: 10.1002/anie.200904944.
(27) De Cremer, G.; Sels, B. F.; De Vos, D. E.; Hofkens, J.; Roeffaers, M. B. J. Fluorescence micro(spectro)scopy as a tool to study catalytic materials in action. *Chemical Society Reviews* **2010**, *39* (12), 4703-4717, 10.1039/C0CS00047G. DOI: 10.1039/c0cs00047g.
(28) Lincoln, R.; Greene, L. E.; Zhang, W.; Louisia, S.; Cosa, G. Mitochondria Alkylation and Cellular Trafficking Mapped with a Lipophilic BODIPY-Acrolein Fluorogenic Probe. *Journal of the American Chemical Society* **2017**, *139* (45), 16273-16281, https://doi.org/10.1021/jacs.7b08615. DOI: 10.1021/jacs.7b08615.
(29) Wäldchen, S.; Lehmann, J.; Klein, T.; van de Linde, S.; Sauer, M. Light-induced cell damage in live-cell super-resolution microscopy. *Scientific Reports* **2015**, *5* (1), 15348. DOI: 10.1038/srep15348.
(30) Parvez, S.; Long, M. J. C.; Poganik, J. R.; Aye, Y. Redox Signaling by Reactive Electrophiles and Oxidants. *Chemical Reviews (Washington, D. C.)* **2018**, *118* (18), 8798-8888, https://doi.org/10.1021/acs.chemrev.7b00698. DOI: 10.1021/acs.chemrev.7b00698.
(31) Beavers, W. N.; Rose, K. L.; Galligan, J. J.; Mitchener, M. M.; Rouzer, C. A.; Tallman, K. A.; Lamberson, C. R.; Wang, X. J.; Hill, S.; Ivanova, P. T.; et al. Protein Modification by Endogenously Generated Lipid Electrophiles: Mitochondria as the Source and Target. *Acs Chem Biol* **2017**, *12* (8), 2062-2069, https://doi.org/10.1021/acschembio.7b00480. DOI: 10.1021/acschembio.7600480.

(32) Yin, H.; Xu, L.; Porter, N. A. Free radical lipid peroxidation: mechanisms and analysis. *Chemical Reviews (Washington, D. C.)* **2011**, *111* (10), 5944-5972, https://doi.org/10.1021/cr200084z. DOI: 10.1021/cr200084z.
(33) Halliwell, B.; Gutteridge, J. M. C. *Free Radicals in Biology and Medicine*; Oxford University Press, 2015.
(34) Perluigi, M.; Coccia, R.; Butterfield, D. A. 4-Hydroxy-2-nonenal, a reactive product of lipid peroxidation, and neurodegenerative diseases: a toxic combination illuminated by redox proteomics studies. *Antioxid Redox Signal* **2012**, *17* (11), 1590-1609, https://doi.org/10.1089/ars.2011.4406. DOI: 10.1089/ars.2011.4406.
(35) Gustafsson, N.; Culley, S.; Ashdown, G.; Owen, D. M.; Pereira, P. M.; Henriques, R. Fast live-cell conventional fluorophore nanoscopy with ImageJ through super-resolution radial fluctuations. *Nature Communications* **2016**, *7* (1), 12471. DOI: 10.1038/ncomms12471.
(36) Van Kessel, A. T. M.; Karimi, R.; Cosa, G. Live-cell imaging reveals impaired detoxification of lipid-derived electrophiles is a hallmark of ferroptosis. *Chem Sci* **2022**, *13* (33), 9727-9738. DOI: 10.1039/d2sc00525e From NLM PubMed-not-MEDLINE.
(37) Johnson, I. D.; Kang, H. C.; Haugland, R. P. Fluorescent membrane probes incorporating dipyrromethene boron difluoride fluorophores. *Analytical Biochemistry* **1991**, *198* (2), 228-237. DOI: https://doi.org/10.1016/0003-2697(91)90418-S.
(38) Lincoln, R.; Greene, L. E.; Bain, C.; Flores-Rizo, J. O.; Bohle, D. S.; Cosa, G. When Push Comes to Shove: Unravelling the Mechanism and Scope of Nonemissive meso-Unsaturated BODIPY Dyes. *Journal of Physical Chemistry B* **2015**, *119* (13), 4758-4765. DOI: 10.1021/acs.jpcb.5b02080.
(39) Serafimova, I. M.; Pufall, M. A.; Krishnan, S.; Duda, K.; Cohen, M. S.; Maglathlin, R. L.; McFarland, J. M.; Miller, R. M.; Frodin, M.; Taunton, J. Reversible targeting of noncatalytic cysteines with chemically tuned electrophiles. *Nature Chemical Biology* **2012**, *8* (5), 471-476, https://doi.org/10.1038/nchembio.925. DOI: 10.1038/nchembio.925.
(40) Shivran, N.; Mula, S.; Ghanty, T. K.; Chattopadhyay, S. Steric Strain Release-Directed Regioselective Functionalization of meso-Methyl Bodipy Dyes. *Organic Letters* **2011**, *13* (21), 5870-5873. DOI: 10.1021/ol202490p.
(41) Chan, D. C. Mitochondria: Dynamic Organelles in Disease, Aging, and Development. *Cell* **2006**, *125* (7), 1241-1252. DOI: 10.1016/j.cell.2006.06.010 (acccessed 2020/03/02).
(42) Shibata, T.; Shimozu, Y.; Wakita, C.; Shibata, N.; Kobayashi, M.; Machida, S.; Kato, R.; Itabe, H.; Zhu, X.; Sayre, L. M.; et al. Lipid peroxidation modification of protein generates Nepsilon-(4-oxononanoyl)lysine as a pro-inflammatory ligand. *J Biol Chem* **2011**, *286* (22), 19943-19957. DOI: 10.1074/jbc.M110.187047.

Chapter 5: Conclusions & Outlook

If the writer of these lines has succeeded in providing some material for clarifying these problems, he may regard his labours as not having been fruitless.

-Vladimir Lenin, The Development of Capitalism in Russia (1899)

5.1 Conclusions and Contribution to Original Knowledge

The important role that ROS plays in biology and medicine has long been established. Lipid peroxidation in particular, culminating in the official denomination of ferroptosis in 2012, has been one of the fastest-growing fields by citation count in the past decade. Our contributions to this now centuries-long line of work, at the intersection of oxidative stress, cell death, and metabolism, are the development of a toolset through which vital problems which still elude the field can be better answered.

This thesis describes our efforts in utilizing intelligent probes that activate upon chemical reaction with the reactive species generated from lipid peroxidation, to study the milieu of oxidative stress-related cell death in live cells.

In **Chapter 2**, we demonstrate the power of our fluorogenic tocopherol probes as a versatile platform for the study of ferroptosis. To date, our work remains unparalleled as the only live cell, real-time observation of lipid peroxidation in ferroptosis. With multichannel microscopy, we uncover a sequence of ferroptosis progression, stemming from the total consumption of membrane-available antioxidants prior to irreversible membrane damage and loss of cellular integrity. With organelle-targeting PMHC analogues, we present evidence for the endoplasmic reticulum as a key site of protection against ferroptosis, along with evidence of the trafficking of oxidized lipids from the internal membranes of the cell to the plasma membrane.

In **Chapter 3**, we present H_3BrB-PMHC, a dormant photosensitizer built on a fluorogenic tocopherol analogue backbone and tuned to emit photons and singlet oxygen. Our group previously introduced the concept of dormant photosensitization as a means to: i. achieve signal amplification of ROS presence via an avalanche chemical reaction and associated emission from newly generated compounds, and ii. as a mechanism to exert another layer of control over the highly toxic production of singlet oxygen in photosensitization, through the chemical cue of singlet oxygen. We demonstrate the autocatalytic nature of the probe, as well as its cell killing capabilities within extreme spatial confinement. In addition, at the single-cell level, we demonstrate that the auto-amplification of our probe has the advantage of identifying potential ROS-sensitive regions of cells, namely lipid droplets.

In **Chapter 4**, we present cyanoAcroB, a fluorogenic electrophile specifically designed for live-cell super-resolution imaging. The reversible nature of the cyanoacrylate moiety mimics the reactivity of lipid-derived electrophiles while also limiting the accumulation of fluorescent product formation, to keep signal-to-noise within reasonable limits for extended super-resolved imaging. We demonstrate this with two applications: localization and fluctuation-based super-resolution microscopy. With cyanoAcroB, 2D dynamics of alkylation events – primarily in the endoplasmic reticulum and mitochondria – can be faithfully recorded by NASCA for up to 90 minutes. With SRRF, we show organelle dynamics on the single cell level for up to an hour of imaging and present an application for the study of ferroptosis that indirectly shows the increase in LDE production in ferroptosis and mitochondria deformation into rings/spheroids early in ferroptosis progression.

Our work highlights the potential of chemoselective fluorogenic probes and live cell fluorescence microscopy as a way of obtaining not only static but dynamic information about biological systems. We have progressed from utilizing probes as mere positional markers to reporters of, and even instigators of, chemical reactions. We hope our work illuminates the way for others, and serves as a blueprint for continuous inquiries into the milieu of oxidative stress in cells and cell death.

5.2 Outlook and Future Directions

Methodology development exists in a cyclic relationship with fundamental biology, with better tools revealing more complex systems, which thus necessitates the development of better methods. Ultimately, we hope that the advancement of ROS probes and quantification methodologies such as those described herein can translate into a more complete understanding of ROS-associated diseases and therapeutics. In this regard, with the work highlighted in this thesis, we propose the following avenues of investigation.

5.2.1 Where do ROS (Plural) Come From?

This work, in particular **Chapter 2**, demonstrates the power of live cell imaging. A natural follow-up would be to ask: to what extent can the limit of detection be pushed? Iterative probe design can achieve higher fluorescence enhancement, based on optimal tuning of HOMO-LUMO gaps, as well as tuning of electron donor/acceptor energy levels. May we then reach the point where observing single ROS events become possible? Moreover, armed with the autocatalytic probe outlined in **Chapter 3**, we envision that with continuous light irradiation and singlet oxygen generation, we can amplify the initial sites of ROS production.

5.2.2 Expanding the Scope of Ferroptosis Inducers

With the methods presented in **Chapter 2**, a logical future direction will be to investigate the array of other ferroptosis inducers, operating at different timescales, in different organelles and through different pathways. Ferroptosis is a flexible array of convergent pathways that can be regulated independently of each other. The classifications of ferroptosis inducers, serendipitously discovered by the Stockwell lab and others on the earliest small molecule screens for RAS-selective cancers, was an ad hoc system with no real reason for its grouping. The focus of this thesis was on exploring the induction

of ferroptosis from direct GPX4 inhibition via RSL3[1-2]– a class II ferroptosis inducer. The choice of this inducer was partly based on its rapid action. The action of class I inducers, such as erastin, which was indirectly observed with glutathione depletion via BSO, takes place over a much longer time scale, tens of hours versus tens of minutes for class II inducers, and is typically observed via endpoint measurements for this reason. The details on the mechanism of action of class III (GPX4 depletion, e.g. FIN56[3]) and class IV (iron oxidation, e.g. $FINO_2$[4]) inducers mechanism of action are still needed. We have demonstrated H_4B-PMHC and the palette of organelle-targeted PMHC RTA fluorogenic probes to be most suitable for real-time live cell observations of ferroptosis induction and the monitoring of specific intracellular contributions to ferroptosis and their relative importance. Efforts may be made to examine the spatiotemporal profiles of lipid peroxidation generated by the actions of different ferroptosis inducers within class I-IV and their evolutions over longer timescales. New invaluable mechanistic insights may well result from these efforts

5.2.3 Cell Cycle and Ferroptosis – Long Time Course Live Cell Imaging

Recent reports have garnered the community's interest on the relevance of the cell cycle to ferroptosis induction, a field to which we believe the methods pioneered in this work are uniquely poised to contribute. During amino acid starvation experiments, Homma and coworkers observed, by chance, that the depletion of S-adenosylmethionine, an intermediate in the methionine-cysteine axis of the transsulfuration pathway, can lead to ferroptosis suppression and cell cycle arrest.[5] This calls into question the role of ROS generated during mitosis and other cell cycle checkpoints,[6] as well as, less certainly, the intracellular distribution of antioxidants during the cell cycle,[7] in partly explaining the differential sensitivities of various cell lines to ferroptosis and the heterogeneity of individual cells in the induction of ferroptosis. The Dixon group in a preprint also demonstrated not only influence of cell cycle arrest in ferroptosis sensitivity, but synergy with class II (GPX4), though not class I (system x_c), ferroptosis activation.[8] Questions of long timescale (up to 24 hours), slow evolution, and intracellular

distribution of lipid peroxidation and its onset are well suited to be answered by H_4B-PMHC, related organelle targeting fluorogenic RTAs, and the work highlighted in **Chapter 2**, making such inquiries a logical extension of this research. In addition to endogenously expressed reporters of cell cycle,[9-10] multichannel imaging could correlate lipid peroxidation levels with cell cycle stages on a single-cell level.

5.2.4 The Contribution of Lipid-Derived Electrophiles – Toward Real-Time Observation

Our group has also developed the fluorogenic LDE mimic – AcroB[11] – and used it to investigate the role of LDEs in ferroptosis,[12] referenced and highlighted in **Chapter 4**. Van Kessel and coworkers utilized AcroB to quantify the degree of LDE-adduct formation and export, showing LDE detoxification impairment as a hallmark of ferroptosis. However, AcroB/cyanoAcroB cannot be used in conjunction with our PMHC-bearing RTA fluorogenic probes for two reasons: 1) spectral overlap, due to both having similar backbone fluorophores and 2) incompatible media conditions, as cell media is rich with nucleophiles (protein, amino acids, etc.).

In the same vein of visualizing the spatiotemporal evolution of LDE production and their fate, we envision the development of the next generation of probes to overcome the current limitations: 1) alternative fluorophore backbones with preferably red absorption/emission and 2) protected AcroB/cyanoAcroB, allowing for selective activation by cellular chemistry rather than media additives.

5.2.5 *Citius, Altius, Fortius*

Cell imaging is a compromise between temporal resolution, spatial resolution, and signal-to-noise. High/super-resolution, high contrast techniques such as STORM and STED require high laser power detrimental to cell vitality,[13] calling into question the biological relevance of these techniques. In a balance of resolution, signal-to-noise, and biological relevance, this work chose to utilize SRRF,[14] a

post-processing enhanced resolution technique, as a minimally invasive method to beat the diffraction limit while gaining new levels of intracellular detail.

Future work should follow the developments in the field of post-processing super-resolution techniques more closely and integrate them into the data processing and experimental design pipeline to answer more challenging questions. Examples such as the recently developed SACD (Super-resolution imaging based on Auto Correlation with two-step Deconvolution), an improvement on SOFI (Stochastic Optical Fluctuation Imaging), optimizes the pre-processing requirements down to 20 frames,[15] opening up the avenue to theoretically to observe super-resolved events down to the sub-second. Cost-effective upgrades to conventional microscope setups, such as adding a phase modulating disk in a spinning disk confocal setup, as highlighted by Zhang and colleagues, may introduce SIM capabilities to an existing system at a very low cost.[16]

The motto of the Olympic Games – *Citius, Altius, Fortius* – is particularly apt for the field of cell imaging and our aspirations. Faster (time resolution), Higher (spatial resolution), Stronger (signal-to-noise and biological relevance).

5.2.6 Weighing the Probe – Toward a Better Understanding of H_4B-PMHC reactivity

Lastly, of particular importance to the future, quantitative works utilizing H_4B-PMHC and other PMHC-based fluorogenic probes require deeper mechanistic studies of the probe. For instance, product studies, via LC-MS (thus the weighing pun) or other means, on the actual activated H_4B-PMHC species are needed to better understand their relevance to biological models such as ferroptosis, especially through the assessment of biases towards the capture of certain species of lipid peroxyl radicals.

5.3 References

(1) Dolma, S.; Lessnick, S. L.; Hahn, W. C.; Stockwell, B. R., Identification of genotype-selective antitumor agents using synthetic lethal chemical screening in engineered human tumor cells. *Cancer cell* **2003,** *3* (3), 285-296.

(2) Yang, W. S.; Stockwell, B. R., Synthetic lethal screening identifies compounds activating iron-dependent, nonapoptotic cell death in oncogenic-RAS-harboring cancer cells. *Chemistry & biology* **2008,** *15* (3), 234-245.

(3) Shimada, K.; Skouta, R.; Kaplan, A.; Yang, W. S.; Hayano, M.; Dixon, S. J.; Brown, L. M.; Valenzuela, C. A.; Wolpaw, A. J.; Stockwell, B. R., Global survey of cell death mechanisms reveals metabolic regulation of ferroptosis. *Nat. Chem. Biol.* **2016,** *12* (7), 497-503.

(4) Gaschler, M. M.; Andia, A. A.; Liu, H.; Csuka, J. M.; Hurlocker, B.; Vaiana, C. A.; Heindel, D. W.; Zuckerman, D. S.; Bos, P. H.; Reznik, E.; Ye, L. F.; Tyurina, Y. Y.; Lin, A. J.; Shchepinov, M. S.; Chan, A. Y.; Peguero-Pereira, E.; Fomich, M. A.; Daniels, J. D.; Bekish, A. V.; Shmanai, V. V.; Kagan, V. E.; Mahal, L. K.; Woerpel, K. A.; Stockwell, B. R., FINO2 initiates ferroptosis through GPX4 inactivation and iron oxidation. *Nat. Chem. Biol.* **2018,** *14* (5), 507-515.

(5) Homma, T.; Kobayashi, S.; Fujii, J., Methionine Deprivation Reveals the Pivotal Roles of Cell Cycle Progression in Ferroptosis That Is Induced by Cysteine Starvation. *Cells* **2022,** *11* (10).

(6) Boonstra, J.; Post, J. A., Molecular events associated with reactive oxygen species and cell cycle progression in mammalian cells. *Gene* **2004,** *337*, 1-13.

(7) Diaz Vivancos, P.; Wolff, T.; Markovic, J.; Pallardó, Federico V.; Foyer, Christine H., A nuclear glutathione cycle within the cell cycle. *Biochemical Journal* **2010,** *431* (2), 169-178.

(8) Rodencal, J.; Kim, N.; Li, V. L.; He, A.; Lange, M.; He, J.; Tarangelo, A.; Schafer, Z. T.; Olzmann, J. A.; Sage, J.; Long, J. Z.; Dixon, S. J., A Cell Cycle-Dependent Ferroptosis Sensitivity Switch Governed by EMP2. *bioRxiv* **2023**, 2023.07.19.549715.

(9) Sakaue-Sawano, A.; Ohtawa, K.; Hama, H.; Kawano, M.; Ogawa, M.; Miyawaki, A., Tracing the silhouette of individual cells in S/G2/M phases with fluorescence. *Chem Biol* **2008,** *15* (12), 1243-8.

(10) Shirmanova, M. V.; Gorbachev, D. A.; Sarkisyan, K. S.; Parnes, A. P.; Gavrina, A. I.; Polozova, A. V.; Kovaleva, T. F.; Snopova, L. B.; Dudenkova, V. V.; Zagaynova, E. V.; Lukyanov, K. A., FUCCI-Red: a single-color cell cycle indicator for fluorescence lifetime imaging. *Cell Mol Life Sci* **2021,** *78* (7), 3467-3476.

(11) Lincoln, R.; Greene, L. E.; Zhang, W.; Louisia, S.; Cosa, G., Mitochondria Alkylation and Cellular Trafficking Mapped with a Lipophilic BODIPY–Acrolein Fluorogenic Probe. *Journal of the American Chemical Society* **2017,** *139* (45), 16273-16281.

(12) Van Kessel, A. T. M.; Karimi, R.; Cosa, G., Live-cell imaging reveals impaired detoxification of lipid-derived electrophiles is a hallmark of ferroptosis. *Chem. Sci.* **2022,** *13* (33), 9727-9738.

(13) Boudreau, C.; Wee, T.-L.; Duh, Y.-R.; Couto, M. P.; Ardakani, K. H.; Brown, C. M., Excitation light dose engineering to reduce photo-bleaching and photo-toxicity. *Scientific reports* **2016,** *6* (1), 30892.

(14) Gustafsson, N.; Culley, S.; Ashdown, G.; Owen, D. M.; Pereira, P. M.; Henriques, R., Fast live-cell conventional fluorophore nanoscopy with ImageJ through super-resolution radial fluctuations. *Nature communications* **2016,** *7* (1), 12471.

(15) Zhao, W.; Zhao, S.; Han, Z.; Ding, X.; Hu, G.; Qu, L.; Huang, Y.; Wang, X.; Mao, H.; Jiu, Y., Enhanced detection of fluorescence fluctuations for high-throughput super-resolution imaging. *Nature Photonics* **2023**, 1-8.

(16) Zhang, Y.; Asghari, P.; Scriven, D. R.; Moore, E. D.; Chou, K. C., Structured illumination microscopy with a phase-modulated spinning disk for optical sectioning. *Optics Letters* **2023,** *48* (15), 3933-3936.

“You can’t resist for very long a truth you discover for yourself”

-Nikolai Chernyshevsky, What Is to Be Done? (1865)

希望本是无所谓有，无所谓无的。这正如地上的路；其实地上本没有路，走的人多了，也便成了路。

“Hope cannot be said to exist, nor can it be said not to exist. It is just like roads across the earth. For actually the earth had no roads to begin with, but when many men pass one way, a road is made.”

-鲁迅《故乡》

- Lu Xun, My Old Home（1921）